Theoretical and experimental contribution to the study of exchange-spring magnets

Renuka Tayade

THESE DE DOCTORAT
DE L'ECOLE NORMALE SUPERIEURE DE CACHAN

Présénte par

Renuka TAYADE

pour obtenir le grade de
DOCTEUR DE L'ECOLE NORMALE SUPERIEURE DE CACHAN

Domain:
Sciences physiques

Sujet de la thèse:

Theoretical and experimental contribution to the study of exchange spring magnets

Thèse présentée et soutenue à Cachan le 2014-07-03 devant le jury composé de :

Lotfi BESSAIS	Professeur des universités, Paris XII	Rapporteur
Mourad CHERIF	Professeur des universités, Paris XIII	Rapporteur
Olivier ISNARD	Professeur des universités, Joseph Fourier	Examinateur
Frèderic MAZALEYRAT	Professeur des universités, L'ENS Cachan	Directeur de Thèse
Martino LOBUE	Chargé de recherche au CNRS	Co-encadrant

SATIE ENS CACHAN, CNRS, UMR 8012.
61, avenue du Prsident Wilson, 94235 CACHAN CEDEX (France)

Table of Contents

Contents **i**

Figures **iii**

Tables **vi**

Symbols **vii**

Acknowledgement **ix**

1 Introduction **4**
1.1 Figures of merit 6
1.1.1 Saturation magnetization 6
1.1.2 Hysteresis 7
1.1.3 Permeability 7
1.1.4 Remanence 7
1.1.5 Coercivity 7
1.1.6 Coercivity mechanisms: Nucleation and Pinning 7
1.1.7 Maximum magnetic energy product 9
1.2 Exchange spring magnet 11
1.2.1 Micromagnetic scale parameters 13
1.2.2 Architecture of exchange spring media 14
1.2.3 Magnetization reversal in ESM 17
1.3 Exchange spring media in magnetic recording 18
1.4 Summary 21
1.5 Plan of Thesis 21

2 Synthesis of Mixture **26**
2.1 Experimental techniques and equipment 27
2.1.1 Sample selection 27
2.1.2 Mechanical milling 27
2.1.3 Ultrasonic mixer 28
2.1.4 X-Ray diffraction 28
2.2 Precursors 28
2.2.1 Structural characterization of precursors 32
2.2.2 Magnetic characterization 33
2.2.3 Conclusion 36
2.3 Mixing 36
2.3.1 Structural characterization of the mixtures 37
2.3.2 Magnetic characterization 42
2.4 Conclusion 43

3 Synthesis of Bulk Magnets **48**

3.1 Spark Plasma Sintering 48
3.2 Mechanically milled bulk samples 49
3.2.1 Structural characterization 50
3.2.2 Magnetic characterization 57
3.3 Partial conclusion 61
3.4 Ultrasonic mixed samples 62
3.4.1 Permalloy 63
3.4.2 Iron 74
3.5 Partial conclusion for ultrasonic mixed samples 76

4 Micromagnetics 82
4.1 Thermodynamic potentials for magnetic systems 83
4.2 Energy contributions 84
4.2.1 Exchange energy 85
4.2.2 Anisotropy energy 86
4.2.3 Magnetostatic energy 88
4.2.4 External field contribution 88
4.3 The free energy 89
4.4 Brown's equation 89
4.5 Landau-Lifshitz equation 90
4.6 Landau Lifshitz Gilbert equation 90
4.6.1 LLG in spherical co-ordinate system 92
4.7 Stoner-Wohlfarth model 92
4.8 Soft and hard material 93

5 Microwave Assisted Magnetization Dynamics 96
5.1 Single phase magnetic system 99
5.1.1 P-modes 102
5.1.2 Phase diagrams for magnetic reversal 105
5.2 Exchange coupled bilayer system 112
5.2.1 Macrospin theory 120
5.2.2 Variation of the microwave field frequency 121
5.3 Summary 124
5.4 Conclusion 124

6 Conclusion and Future Prospects 128
6.1 Conclusion 128
6.2 Future Prospects 130

Appendix A 134

Appendix B 137

Bibliography 144

List of Figures

1.1 Orstead and Ampere 5
1.2 Relative hysteresis for Hard and Soft magnets 6
1.3 Nucleation 8
1.4 Pinning 9
1.5 Second quadrant of hysteresis 9
1.6 Energy Product development 11
1.7 Exchange Spring 12
1.8 Thin film exchange spring 12
1.9 Hard Soft spins 12
1.10 Architecture for Exchange Spring Nanocomposites 15
1.11 Effect of interaction in soft, hard regions 16
1.12 Hystersis in ESM 17
1.13 Recording Trilemma 18
1.14 Microwave field application 19

2.1 Planetary Ball Mill 28
2.2 Ultrasonic mixer 28
2.3 BaM structure 29
2.4 Flowchart of Sol-gel process 30
2.5 Iron-BCC structure 31
2.6 Permalloy-FCC structure 31
2.7 XRD-BAM powder 32
2.8 XRD-Permalloy powder 33
2.9 XRD-Iron nanopowder 33
2.10 Magnetization loop-Commercial ferrite and powder 34
2.11 Magnetization loop-Permalloy 35
2.12 Magnetization loop-Iron 36
2.13 XRD-N2H-25min 37
2.14 XRD-N2H (milling time) 38
2.15 SEM-N2H powder 39
2.16 XRD-N5H-35min 39
2.17 SEM-N5H 40
2.18 XRD-N10H-35min 40
2.19 SEM-N10H 41
2.20 XRD-NXH vs vol.fraction 41
2.21 XRD-N10U 42
2.22 SEM-N10U 42
2.23 Average magnetization of mixture of 50% permalloy and BaM 43

3.1 Current flow through particles during spark plasma sintereing. 49
3.2 SPS-Insideview 49
3.3 SPS condition profile 50
3.4 XRD-N2H800-40min 51

3.5 SEM-N2H800 51
3.6 Density variation for $N2H800$ sample with milling time. 52
3.7 XRD-NXH800 with milling time 52
3.8 Diffraction pattern for $N5H800$. 53
3.9 SEM-N5H800 54
3.10 XRD-N10H800 at different milling time 55
3.11 SEM-N10H800 56
3.12 XRD-NXH800 patterns 57
3.13 Hysteresis loop N2H800 at different milling time 57
3.14 Variation of coercivity for $N2H800$ sample with milling time. 58
3.15 Variation in saturation magnetization and remanence for $N2H800$ series with milling time. 58
3.16 Hysteresis curve with variable milling time for $N5H800$ series as indicated in the label. 59
3.17 Hysteresis curve with variable milling time for $N10H800$ series as indicated in the label. 60
3.18 Comparison of saturation magnetization for mechanical milled alloys 61
3.19 XRD-N2U500 63
3.20 XRD-NXU550 (milling time) 63
3.21 XRD-N5U500 65
3.22 XRD-NXU500 with increasing volume fraction 65
3.23 Hysteresis of NXU550 system 66
3.24 Hysteresis loop for different volume percentage of $Fe_{25}Ni_{75}$ in $NXU500$ series. 67
3.25 Variation of M_s with respect to volume fraction of permalloy in NXU500 68
3.26 Variation of H_c with respect to volume fraction of permalloy in NXU500 68
3.27 Variation of σ_s with respect to volume fraction of permalloy in NXU550 69
3.28 Variation of σ_s with respect to volume fraction of permalloy in NXU550 70
3.29 Variation in hysteresis is shown with temperature for $N10U500$ sample. 71
3.30 Variation of hysteresis with temperature for $N20U500$ sample. 71
3.31 Variation of H_c as a function of temperature with respect to volume fraction of permalloy in NXU500 72
3.32 Hysteresis measurement for $N10U550$ at different temperature. 72
3.33 Hysteresis measurement for $N20U550$ at different temperature. 73
3.34 Variation of H_c with respect to volume fraction of permalloy in NXU550 73
3.35 Hysteresis loop for $N10U$ samples at different sintering temperature. 74
3.36 XRD-FXU550 with increasing volume fraction 75
3.37 Hysteresis for FXU550 75
3.38 Variation of magnetic parameters for $FXU550$ series with respect to the different metallic volume fraction. 76

4.1 Uniaxial anisotropy 87
4.2 Cubic anisotropy 88

5.1 Rotating frame 98
5.2 Representation of the Single phase magnetic system with perpendicular anisotropy. 99
5.3 polar angles 100
5.4 Astroid for **P**-mode 102
5.5 Solution of Hard magnetic phase going towards stability. 104
5.6 Hysteresis of hard phase in absence of in-plane microwave field. 105
5.7 Hysteresis of hard and soft phase in presence of microwave field. 106
5.8 Phase diagram for hard phase at 6GHz. 107
5.9 Hysteresis of hard phase subjected to 10GHz 108

5.10 Phase diagram for hard phase at 10GHz 109
5.11 Thershold field for Hard phase 110
5.12 Forward branch for hard phase at various frequencies 111
5.13 Variation of switching field in hard phase 111
5.14 Average magnetization for bilayer at 10GHz 112
5.15 Basic model for of hard/soft bilayer with perpendicular (z-axis) anisotropy axis. 113
5.16 Average magnetization for bilayer at 6 GHz. 115
5.17 Zero directional field switching 116
5.18 Spatial profile of bilayer at 6 GHz before switching 116
5.19 Difference in applied field for uniform and non-uniform system. 118
5.20 Exchange energy vs magnetization angle. 119
5.21 magnetization in macrospin at 6 GHz 120
5.22 Average magnetization in response to varying magnitude of in-plane microwave field. 122
5.23 Variation of Switching field in bilayer system as a function of frequency. 123
5.24 Comparison between the switching field of bilayer and hard system and its variation with the microwave frequency. 124

6.1 Flow chart of finite difference program 134
6.2 Time discretization and spatial point mesh. 135
6.3 Saddle-node bifurcation 139
6.4 Graphical representation of the super-critical hopf-bifurcation. 139
6.5 Graphical representation of the sub-critical hopf-bifurcation. 140
6.6 Representation of $(h_{az}, h_{a\perp})$ plane. 140

List of Tables

2.1 Comparison of parameters in the various samples of Barium hexaferrite. 34
2.2 Comparison of parameters in the various samples of $Fe_{25}Ni_{75}$. 35
2.3 Naming of the series of the samples 37
2.4 Specific characteristics of precursors. 37
2.5 Variation in volume fraction and crsyatllite size for $N2H$ samples milled for different time. 38

3.1 Naming scheme of the sintered bulk samples. 50
3.2 Microstructure parameter of $N5H800$ series of samples revealed from Rietveld's refinement method 53
3.3 Microstructure parameter of $N10H800$ series of samples revealed from Rietveld's refinement method. 55
3.4 Influence of different percentage of iron-nickel in barium hexaferrite on the magnetic properties in $NXH800 - 45min$ samples. 60
3.5 Naming scheme of the sintered bulk samples using ultrasonic mixing. 62
3.6 Microstructure parameter of $NXU550$ series of samples revealed from Rietveld's refinement method. 64
3.7 Microstructure parameter of $NXU500$ series of samples revealed from Rietveld's refinement method. 66
3.8 Influence of different percentage of iron-nickel in barium hexaferrite on the magnetic properties in $NXU550$ samples. 77
3.9 Influence of different percentage of iron-nickel in barium hexaferrite on the magnetic properties in $NXU500$ samples. 78

5.1 Width of the transition region at different frequencies of the in-plane applied field. 117

List of Symbols

$\mathbf{E}$	Electric Field	5
$\mathbf{B}$	Magnetic field	5
M	Magnetization	6
H	Magnetic field strength	6
M_s	Saturation magnetization	6
μ	Permeability of free space	7
M_r	Remanance	7
H_c	Coercivity	7
H_N	Nucleation Field	8
K	Magnetocrystalline Anisotropy Constant	8
H_P	Pinning or Propagation Field	8
A	Exchange Stiffness constant	9
$(BH)_{max}$	Maximum Energy Product	9
H_d	Demagnetizing Field	9
l_{ex}	Exchange length	14
l_w	Domain wall width	14
J	Exchange Coupling Constant	17
$G_L(\mathbf{M}; \mathbf{H}_a, T)$	Landau Free Energy	22
U	Internal Energy	83
S	Entropy	83
$\mathbf{H}_a$	Applied Magnetic Field	83
dQ	Heat absorbed by the system	83
T	Temperature	83
S	Entropy	83
$E(\mathbf{H}_a, S)$	Enthalpy	83
$F(\mathbf{m}, T)$	Helmholtz Free Energy	83
$\mathbf{H}_{eff}$	Effective Field	90
γ	Gyromagnetic ratio	90
α	Damping Constant	90
N_x, N_y, N_z	Demagnetizing Factors	92

Acknowledgement

Dr. A. Kalam, a great scientist once said,

Man needs his difficulties because they are necessary to enjoy success.

Everyone who has crossed his difficult times realizes this thought. Sometimes it dawns upon you that, when you succeed, it was not only you alone but an ensemble of various things and people that made you overcome all the barriers, travel through bad and good times, and ultimately reach the goal. These incidents leave their mark in your life. And today i am reminded of the words by *J.F.Kennedy*,

We must find time to stop and thank the people who makes a difference in our lives.

I take this platform to thank all those who have touched me, helped, loved, nurtured, influenced, taught and strengthened me, moreover had courage to show me my weaknesses and make sure i work on them. I would like to thank first of all *Prof.S.N.Kane* to encourage me to pursue a research career and honor me with a possibility to work in France. Of course, that couldn't have been possible without *Prof.F. Mazaleyrat*, also my thesis director, who accepted me as his student. My deepest thanks for providing me the support and facilities and opportunities to travel in conferences. I also thank the Director of laboratory **SATIE**, *Pascal Larzabal*, for all the support and facilities. Deepest affection for the whole administrative staff, *Ms.Abriet, Ms.Bacquet and Ms.Gallos* for their support. I also would like to extend my gratitude to the technical staff, and i shall never forget very warm and friendly greetings from *Mr.Bach*, for who i shall remain as "Dora, L'exploratrise".

I also thank *Ecole Doctorale* (EDSP) for their support and efficient but a lot of paperwork that they made me do, it is nevertheless obligatory for all! The years in *SATIE* haven't been a cake walk, and i can not thank enough my supervisor *Dr.M.LoBue* for standing by me. His immense reservoir of patience in handling my bad scientific writing and my silly mistakes with formule and unorganized-ness, surely is commendable, and a large amount of humble apologies and many thanks. Thank you once again for always keeping my spirits up and scolding me whenever needed and for constant encouragement. I also would like to show my gratitude to *Dr.O.Pasko*, fondly known as *Sasha*, for teaching me the experimental techniques and for being a person who has always been ready to help whenever asked for. A big part of my work is all because of him.

Many others helped me in this work as well, and i would like to acknowledge *Dr.O.De La Barrier, Dr.V.Loyau* for their assistance. Thanks to *Dr.Karim Zehani* for being an excellent teacher. I was fortunate enough to work and be in company of some great people, i am indebted to *Prof.C. Serpico*, for his co-operation and sharing his work and teaching me the mathematical treatments. I would also like to thank *Prof.G. Bertotti* for the discussions which really helped my work. During the doctoral studies, i have met a lot of wonderful people, explored different types of food and culture. This fun and friendliness couldn't have been possible if not for such amazing colleagues, *Dr.Slim, Dr.Lilia, Dr.Marwan, Dr.Linh, Kien, Oussama, Muriel, Emna, Hiba, Dhouha, Raouia, Nomane, Yazid, Julien, Pierre* and all the rest of my colleagues.

Special thanks to *Dr.Nidhal (aka water-girl), Baptist (aka Batman), Dr.Benjamin (aka Big-Ben), Adrien (aka Ady), Victor (aka "vicky"), Sylvain and Kevin (aka KK)* for teaching and playing "bellot" with me, acting in the movie, partying and making fun of each other and eating **the**

CROUS food. I loved all these things because of you guys and thank you so much for making such fantastic memories for me. Thanks to *Aiswarya* and *Amal* for the interesting conversations and spicy dinners.

As a typical Bollywood fan, i quote a cliché, "Friendship needs no sorry and no thank you." My friends who i can not belittle by saying thanks, but they need to be mentioned for having been integral part of my life, *Archana, Praveena, Meghna, Vinoth, Srikanth, Avinash, Saravanan* and extremely loved by all, my bro *Mithun*. My two best friends, philosophers and guide, with who i can always be myself, *Sapana and Soumya*. Special credit to you both for bearing with me for years, salute to you for your patience. Love you guys always. Thanks to *Sagar* for memorable family time holidays. *Rohan*, thanks for always being there to give advice about anything on this earth when asked for, despite of being busy always. Finally, i wish i can shower as much love and show as much support and have as much strength as my parents. I might not say it enough but i love you always. Also thanks for being over tensed and dramatic and passing on that trait in me as well :D Acknowledgment wouldn't complete without mentioning my brother, *Gautam*, who should thank me for being his elder supportive sister!!!

I must not forget to thank, the most important *things* that have encouraged me, always been there with me during distressed times and uplifted me - Songs in my playlist!! Thanks to *Raju Hirani and Aamir* for making a truly entertaining "*3 idiots*", a film that not only motivates and teaches but reinvents the notion, *"All izz well"* (worked several times for me). Thanks to *J.K.Rowling* for the magnum opus, *Harry Potter* Series for the inspiration to keep moving and making my difficulties seem lesser. My source of motivation, "The Prodigal Daughter", for which i am highly grateful to *Jeffery Archer*. *R.P.Feynman* has been a reservoir of knowledge and fun and an amazing teacher and i am glad that such people are always alive through books and recorded videos, that keep my interest alive and make Physics a lot of fun. Truly love you Mr.Feynman.

No work today is complete with out the support of technology. I thank *DELL, Microsoft, LaTeX and MATLAB* and the people behind it.

CHAPTER 1
INTRODUCTION

Chapter 1

Introduction

Contents

1.1	Figures of merit	**6**
1.1.1	Saturation magnetization	6
1.1.2	Hysteresis	7
1.1.3	Permeability	7
1.1.4	Remanence	7
1.1.5	Coercivity	7
1.1.6	Coercivity mechanisms: Nucleation and Pinning	7
1.1.7	Maximum magnetic energy product	9
1.2	Exchange spring magnet	**11**
1.2.1	Micromagnetic scale parameters	13
1.2.2	Architecture of exchange spring media	14
1.2.3	Magnetization reversal in ESM	17
1.3	Exchange spring media in magnetic recording	**18**
1.4	Summary	**21**
1.5	Plan of Thesis	**21**

For a long time, till early 19th century, the only magnetism known to the man was that of iron magnets and of "lodestones", natural magnets of iron-rich ore. It was believed that the inside of the Earth was magnetized in the same fashion, and scientists were greatly puzzled when they found that the direction of the compass needle at any place slowly shifted, decade by decade, suggesting a slow variation of the Earth's magnetic field [1].

The question still lingered, how can an iron magnet produce such changes? It was proposed by Edmond Halley (of comet fame) that the Earth contained a number of spherical shells, one inside the other, each magnetized differently, each slowly rotating in relation to the others.

It was Hans Christian Oersted Fig. 1.1, a professor of science at Copenhagen University at that time, who demonstrated an experiment in his home to his friends and students. He planned to demonstrate two experiments, the heating of a wire by an electric current, and also to carry out demonstrations of magnetism, for which he provided a compass needle mounted on a wooden stand. While performing his electric demonstration, Hans Christian Oersted noted to his surprise that every time the electric current was switched on, the compass needle moved. He kept quiet and finished the demonstrations, but in the months that followed, he worked hard trying to make sense out of the new phenomenon. He still could not come to any certain explain. The needle was neither attracted to the wire nor

repelled from it. Instead, it tended to stand at right angles. In the end he published his findings without any explanation.

Figure 1.1: a) Hans Christian Orstead,courtesy:Meyers Lexicon books b) Andre Marie Ampere, courtesy:Smithsonian Libraries.

During the same time, André Marie Ampère in France felt that if a current in a wire exerted a magnetic force on a compass needle, two such wires also should interact magnetically. In a series of ingenious experiments, André Marie Ampère showed that this interaction was simple and fundamental - "The parallel (straight) currents attract, anti-parallel currents repel". The force between two long straight parallel currents was inversely proportional to the distance between them and proportional to the intensity of the current flowing in each. There thus existed two kinds of forces associated with electricity–electric and magnetic.

In 1864, James Clerk Maxwell demonstrated a subtle connection between the two types of force, unexpectedly involving the velocity of light. The equations of Maxwell's relate the electric and magnetic fields,$\mathbf{E}$ and $\mathbf{B}$ at a point in free space to the distributions of electric charge and current densities in surrounding space. From this connection sprang the idea that light was an electric phenomenon, the discovery of radio waves, the theory of relativity and a great deal of present-day physics[2].

However the problem of explaining ferromagnetism in solids remained unresolved for a long time, until 20th century after the development of quantum mechanics. Today's knowledge about magnetism has enriched manifolds since then. Yet the fundamental behavior and the origins of the magnetism still needs to be explored.

With the availability and advancement in techniques and technology, the scientists are continuously trying to study the fundamentals. People are trying to process new and energy efficient materials [3] for improving the efficiency of power consumption, transmission, utilization and in the progressive replacement of oil-based fuels, in transportation by electric motors etc. Magnetic materials, such as advanced hard and soft magnets play significant role in improving technologies such as magnetic refrigerants, magnetic MEMS (microelectromechanical systems), magnetic shape memory alloys etc [4].

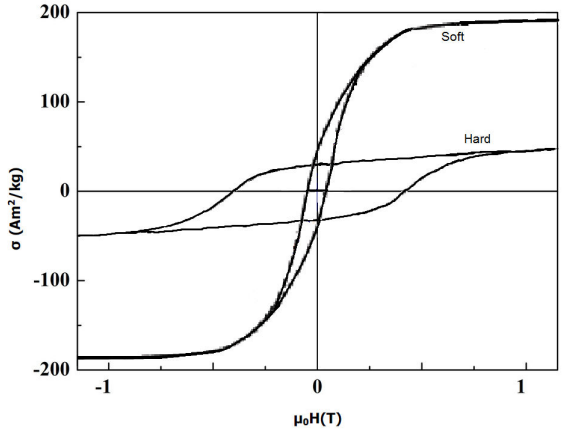

Figure 1.2: Representation of hysteresis loop for hard and soft magnetic materials.

Currently, from the application point of view, the magnetic materials can be divided into two main categories: the magnetically *soft* (easy to magnetize and demagnetize) and the magnetically *hard* (hard to magnetize and demagnetize) as shown in fig. 1.2. The distinguishing characteristic of the first group is high permeability, and it is chiefly this flux-multiplying power of the magnetically soft materials that fits them for their job in machines and devices. Magnetically hard materials, on the other hand, are made into permanent magnets; here a high coercivity is a primary requirement because a permanent magnet, once magnetized, must be able to resist the demagnetizing action of stray fields including its own [5]. For example, the soft materials are, Iron, cobalt, Nickel etc. and the hard magnetic materials are Alnico, Barium Ferrite, Remalloy etc.

The earliest, and for a long time the only, application of the permanent magnet was the compass needle. Today magnetic materials provide high efficiency and reliability and compact, low cost, and low maintenance solutions for renewable energy technologies, including wind turbines, hydroelectric power generators, and wave PowerBuoys etc. Our main focus in this work is to overcome one of the major challenge to improve the characteristics of Permanent magnet. Permanent magnetic materials used in electric machines require a high saturation magnetization as well as high coercivity. Before going any further let us first explore the key characteristics of magnetic materials.

1.1 Figures of merit

In this section, we shall explore the key features used to represent a magnet. Magnetic properties of magnetic materials are characterized by variation of magnetization M with applied field H. The curves between M and H is called *magnetization curve*.

1.1.1 Saturation magnetization

At large enough value of H, the highest possible magnetization achieved by the magnet on after which it is not possible to increase the magnetization no matter how much ever the external magnetic field increases. This constant value of M denoted by M_s is called *Saturation magnetization*. The highest value of saturation in bulk material is $M_s = 1.95 \times 10^6\ Am^{-1}$ ($J_s = 2.45\ T$) by Iron-cobalt alloy with 35% of cobalt[6].

1.1.2 Hysteresis

After the magnetic material achieves saturation, and then a decrease in applied field H to zero does not reduce M to zero. Thus one can say that the magnetization *lags behind* the applied field and this phenomenon is called hysteresis.

1.1.3 Permeability

Permeability is one of the important parameter of a magnetic material which indicates how much magnetic induction B is generated by the material in a given magnetic field strength H [6]. The ratio of B to H is called permeability, denoted by $\mu = B/H$. This term was coined by Oliver Heaviside in 1885. It is measured in N/A^2 in S.I. units. The permeability constant μ_0, also called *permeability of free space*, is the measure of magnetic field generated by a moving electric charge in a vacuum. This constant has a definite value $\mu_0 = 4\pi \times 10^{-7} \approx 1.25 \times 10^{-6}\ mkg/s^2A^2$.

1.1.4 Remanence

When the applied field on a magnetic material is reduced to zero, the magnetization M does not reduce to zero immediately, there is a residual magnetization at $H = 0$. This residual magnetizationos called Remanence,M_r.

1.1.5 Coercivity

Further reduction of the applied field H to negative values, after the magnetization of the material is driven to saturation, at a certain value of $H = H_c$, the magnetization becomes zero. This value of the applied field given by H_c, is known as Coercivity. Thus coercivity measures the resistance of the magnetic material to become demagnetized.

It is an important parameter to distinguish between a hard and a soft magnetic material. More the H_c, the more magnetically hard a magnetic material is. Such materials are used to make permanent magnets.

1.1.6 Coercivity mechanisms: Nucleation and Pinning

There are two basic coercivity mechanisms: Nucleation and Pinning. In order to understand the hysteresis and the magnetization processes of a ferromagnet, it is first necessary to understand the magnetization reversal processes in the system. The magnetization processes are related to the modification, and eventual elimination of the domain structure with increasing applied magnetic field.

Let a ferromagnetic system be first subjected to external magnetic field, which is large enough to saturate the system in the field's direction. The field is then reduced slowly, to avoid dynamic effects. If necessary, the field is decreased to zero, then increased slowly in the opposite direction. During this process, the state of saturation along the original direction of the applied field starts to becomes unstable, and some changes start to take place. The field at which the original saturated state becomes unstable and any sort of a change in the magnetization configuration starts, is called the *nucleation field*. The definition contains history of the applied field.

The saturated state in any system is the state of minimum energy. When the field goes to zero, the saturated state in the opposite direction, is the lower minimum. But it is difficult to reach the lower minimum due to energy barrier. Showing that, other energy

is lower than magnetization state does not prove that the magnetization will chose that state. It must be proven that the lowest energy state is accessible to the system. Since the state is the function of space therefore there are many paths to reach the minima.

The nucleation process, at the start of the reversal process, is studied by linearizing the Brown's equation. Linearization is the an indication of requirement of continuity. Nucleation means that a magnetization state becomes unstable at the nucleation field H_N. In nearly perfect magnets, H_N is a good estimate for the coercivity, $H_c \approx H_N$.

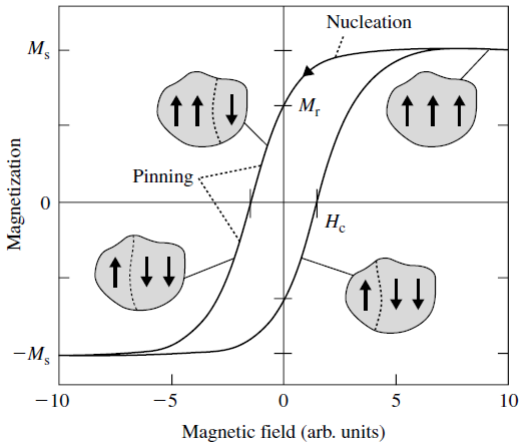

Figure 1.3: Origin of Hystersis:Coercivity mechanism in ferromagnetic particle. Here, the fully magnetized state is unstable (top right)so coercivity is due to domain wall pinning.

The nucleation instability is obtained by eigenmode analysis and the stability is determined by the lowest curvature or eigenvalue. The eigenfunction $\mathbf{m}(\mathbf{r})$ that corresponds to the nucleation field is known as the nucleation mode.

We get and expression of the nucleation field, $H_N = 2K/\mu_0 M_s$. Where K is the anisotropy constant.

If localized nucleation leads to complete magnetization reversal, then the coercivity H_c is equal to the nucleation field H_N. However, this process requires the growth of the reverse domain, and the corresponding domain-wall motion may be hindered by real-structure imperfections [7], [8]. This mechanism is known as *domain-wall pinning*. It is the main source of hysteresis and coercivity in strongly inhomogeneous magnets and yields coercivities $H_c > H_N$. Since the domain wall energy is proportional to the square root of K, domain-wall pinning often occurs in regions where K is small due to chemical disorder (for eg. substituted transition metals and RE magnets). The domain wall is trapped in a region with low domain-wall energy, and the coercivity is given by the pinning or depinning field H_P necessary to push the wall over the pinning-energy barrier.

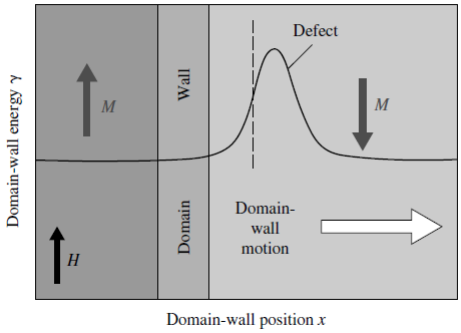

Figure 1.4: Pinning mechanism in the ferromagnetic materials.

A very simple pinning model considers the energy $E(x)$ of a planar domain wall as a function of the wall position x. In practice, $E = 4\sqrt{AK}$, where A is exchange constant, is often determined by the local chemistry, which determines $K(x)$. Fig.1.4 shows an example where the wall energy of the defect is higher than that of the main phase. This regime is known as repulsive pinning and means the penetration of the wall into the defect costs energy. By contrast, attractive pinning amounts to the capturing of a wall in a region of low wall energy. In both regimes, the coercivity is given by analyzing the magnetic energy $E(x)$ as a function of the wall position x.

1.1.7 Maximum magnetic energy product

The maximum energy product $(BH)_{max}$ of a magnetic material is a measurement for the maximum amount of magnetic energy stored in a magnet. It concerns the product, maximally attainable with a magnetic material, made out of flux density B and field strength H. High energy product can be described as the maximum area swept by a rectangle in the second quadrant of a hysteresis loop (B-H curve), as shown in fig.1.5. It is given by $(BH)_{max} = \mu_0 M_r^2/4$. It is simply the measure of the maximum amount of useful work, that a permanent magnet is capable of doing, outside the magnet [9].

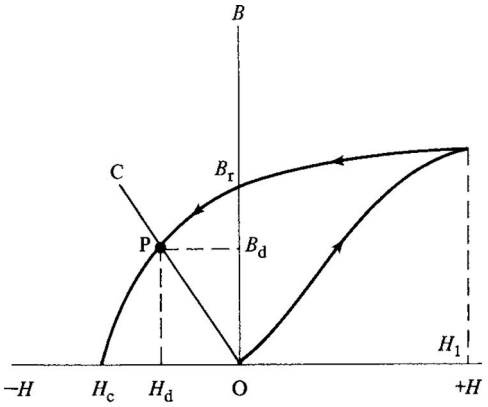

Figure 1.5: Initial magnetization and demagnetization curve of a permanent magnet. Br is the residual induction; point P is the operating point, courtesy: Cullity

We can understand the significance of $(BH)_{max}$ or maximum energy product, by looking at the operation of a magnet. A permanent magnet operates as an "open circuit". The poles create a demagnetizing field H_d which makes induction B lower than the remanence B_r. When the magnet is manufactured it is subjected to a strong magnetic field which makes the induction to follow the path as indicated in fig.1.5. The line OC called the

load line and the operating point P in the second quadrant of the hysteresis loop (also called the demagnetization curve) could possibly be anywhere on this line OC. The best operating point P is chosen in the following way.

According to the Ampere's law,

$$\oint H dl = 0 \tag{1.1}$$

Let H_g be the constant field strength provided by the magnet, B_m is the induction and H_m is the field. Let l_m be the length of the magnet and l_g length of the gap between the poles. Then from (1.1),

$$H_g l_g - H_m l_m = 0 \tag{1.2}$$

The magnetic flux (ϕ) is given as:

$$\phi = B_g A_g = \mu_0 H_g A_g = B_m A_m \tag{1.3}$$

Where, A_g and A_m are the cross section areas of the gap and magnet. Multiplying eq.(1.2) and (1.3) and using the fact that $\mathbf{B}_g = \mu_0 \mathbf{H}_g$,

$$(\mathbf{B}_m \mathbf{H}_m) V_m = \mathbf{B}_g^2 V_g / \mu_0, \tag{1.4}$$

where V_m, V_g represent the volume of the magnet and the airgap, respectively. The flux density in the gap is, therefore maximized when the product $B_m H_m$ is maximum; hence there is the emphasis on energy product as a figure of merit for permanent magnets. For most efficient use of material, the magnet should be so shaped that the load line passes through the point at which BH has its maximum value $(BH)_{max}$ [1].

Although $(BH)_{max}$ is an index of material quality, it is not the only index or even the most suitable one for all applications.

The theoretical maximum product is calculated to be $(BH)_{max} = \mu_0 M_r^2/4$ estimated to be $1 MJm^{-3}$ [10]. The energy product, which is a key figure of merit of permanent magnets, has been enhanced, starting from $\approx 7.96\ KJ/m^3$ for steels discovered during the early part of the century, increasing to $\approx 23.88\ KJ/m^3$ for hexagonal ferrites, and finally peaking at $\approx 445.76\ KJ/m^3$ for neodymium-ironboron magnets during the past ten years. With this, almost 90% of the limit for the energy density, $(BH)_{max}$, (based on the $Nd_2Fe_{14}B$ phase) can be achieved in commercially produced sintered Nd-Fe-B grades [4].

The historical evolution of energy product, spanning nearly 100 years, for the permanent magnets is shown in fig.1.6. For most of the twentieth century, the strength of magnets jumped up every decade or so, with the introduction of new materials. The improvement has now slowed, but researchers hope to make the next leap soon [11].

In this respect, currently, the most actively pursued approach for improvement in the maximum energy product, is synthesis of nanocomposites. This is carried out with particular emphasis on attempt to have the hard magnetic phase textured, as well as exchange-coupled with a soft magnetic phase, called the *Exchange Spring Magnets* (ESM). The latter phase has an intrinsic upper limit of $\mu_0 M_s = 2.43T$ for an $Fe_{65}Co_{35}$ alloy, where M_s is the saturation magnetization. Recently, there is a much revived interest in various types of high-performance permanent magnets, based on rare-earth (RE) intermetallic compounds.

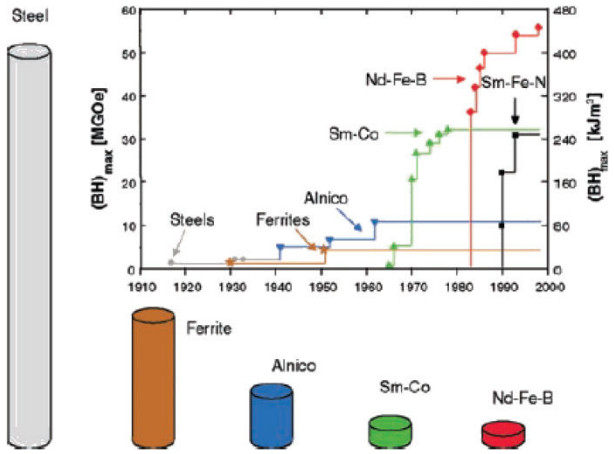

Figure 1.6: Development in the energy density $(BH)_{max}$ at room temperature of hard magnetic materials in the 20th century and presentation of different types of materials with comparable energy density (each magnet is designed so that at a reference point 5 mm from the surface of the pole, a field of 100 mT is produced).

But use of RE elements brings about a corporate competition. Despite their name, the RE elements such as neodymium, aren't truly rare geologically, but they are expensive to mine and process. China, which provides about 95 % of the 96,000 tonnes of RE currently produced worldwide every year, has put increasingly stringent caps on the exports, even as the need for the RE elements is booming. Magnets made with RE are at the heart of modern technology from mobile phones and laptops to high-efficiency washing machines. And many devices that are part of the green economy require substantial amounts of RE elements: an electric car carries a few kilograms of rare-earth elements, and a 3-megawatt wind turbine uses about 1.5 tonnes. Demand leapt from 30,000 tonnes in the 1980s to 120,000 tonnes in 2010, and is predicted to hit 200,000 tonnes by 2015, says Gareth Hatch, founder of the Technology Metals Research consultancy in Carpentersville, Illinois.

The leading idea for how to make next-generation magnets, involves combining nanoparticles of rare-earth magnets with nanoparticles of cheaper magnetic materials creating super-strong end-products with far less of the expensive ingredients. Various nationals are keen to invest in energy-efficient technologies, and scared by a global crunch in the RE market, have started to pay attention to magnetic research [11].

1.2 Exchange spring magnet

The term "Exchange Spring" was first used in 1991 by Kneller and Hawig [12]. Exchange spring magnet (ESM) (although has nothing to do with the actual spring in between!), like composite magnets consisting of a hard magnetic phase and a soft magnetic phase having an inter-phase exchange interaction. A representation of ESM is shown in fig.1.7. The hard and soft phases are combined together to bring about enhancement in the magnetic properties of a magnet. ESM has the higher magnetization from the soft phase and high coercivity from the hard phase, which makes them suitable for the applications of permanent magnets.

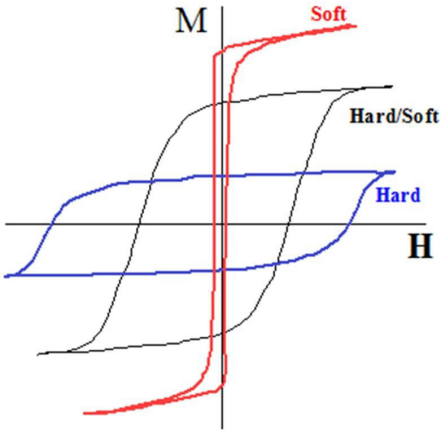

Figure 1.7: Demonstrates the hysteresis of hard and soft phase magnets in blue and red respectively. The resultant hysteresis of the two phases i.e. the Exchange Spring hysteresis loop is shown in black.

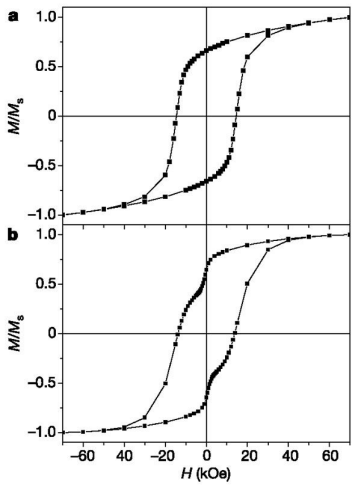

Figure 1.8: Composite of (a)$Fe_3O_4 : FePt$ showing single phase behavior with effective exchange coupling between the two phases and (b)$Fe_3O_4 : Fe_{58}Pt_{42}$, shows two phase hysteresis.[13]

Skomsi and Coey showed that, it is possible to increase the energy product by exploiting the exchange coupling between the hard and soft phases [14]. The additional benefit of having a soft magnetic phase, is reduction of RE materials in magnets [15]. The hard-soft nanocomposites are often obtained in form of thin films, as granular materials or continuous multilayers [16], [17], [18].

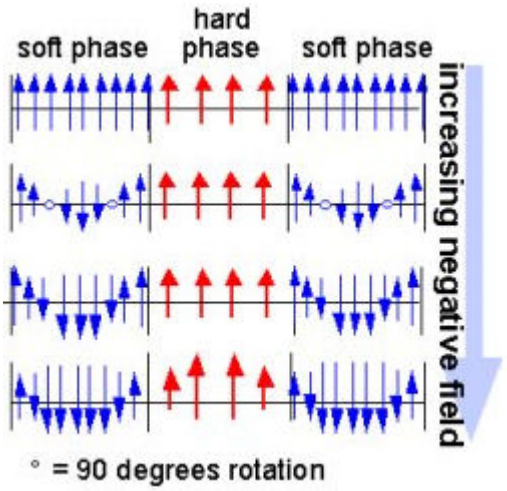

Figure 1.9: Magnetic exchange spring: Hard phase stiffness response of soft high-magnetization phase in magnetic nanocomposite structures, [12]

An important phenomena, that occurs in ESM is that, the soft grains are pinned to the hard-magnet grains at the interfaces by the exchange interaction, while the center of the soft magnet grains can rotate in a reversed magnetic fields, fig.1.9. Such magnets are characterized by enhanced remanent magnetization and reversible demagnetization curves, since the soft grains will rotate back into alignment with the hard grains on removal of applied field.

Although some application of two-phase magnets are based on randomly dispersed nanocomposite geometries, coupled bilayer films provide convenient model systems. Coupled bilayer

films are useful for studying the exchange spring properties because, the relative length scales i.e. thicknesses of the hard- and soft-magnet layers, can be controlled during the deposition process [19]. The heterostructures of hard/soft ferromagnetic layers, such as exchange-coupled bilayers, are widely studied as a model system in order to get a better physical understanding of the exchange-spring magnet.

The bulk processing of exchange spring is essential for practical applications of permanent magnets. Energy product, in case of exchange spring magnets, is the key figure of merit for permanent magnetic application. It is formulated as shown by Skomsi et al. [10] in the following way. The total remanence is given by $M_r = V_h M_h + V_s M_s$, where V_h, V_s are the volume fraction of hard and soft magnetic phase respectively. M_h and M_s are the remanence of hard and soft magnets respectively. Similarly the effective crystalline anisotropy is given as $K_{eff} = V_h K_h + V_s K_s$, with K_h being the anisotropy constant of the hard phase and K_s, of the soft phase. In this case the maximum achievable theoretical coercivity is given by

$$\mu_0 H_c = 2\frac{V_h K_h + V_s K_s}{V_h M_h + V_s M_s} \tag{1.5}$$

The optimal value of the energy product is given by $\mu_0 M_r^2/4$ for $H_c > M_r/2$ and $\mu_0 M_r H_c/2$ for $H_c < M_r/2$. Using eq.(1.5) for $H_c = M_r/2$, under the assumptions that $K_s = 0\ J/m^3$, the $(BH)_{max}$ is given as:

$$(BH)_{max} \approx \frac{\mu_0 M_{s,soft}^2}{4}\left(1 - \frac{\mu_0(M_{s,soft} - M_{s,hard})M_{s,soft}}{2K_h}\right) \tag{1.6}$$

Most of the studies on ESM, have been focused on the investigation of the dependence on thickness and most of them are focused on the properties at high temperatures, where it is technically important. However, it is also interesting to explore the magnetization reversal behavior, since ESM can provide a very unique magnetic environment, and it can be made as a hybrid system [20]. Magnetization reversal process is one of the important concept for assessing the applications of ESM.

Yan et al.[21], [22] have explained magnetization reversal processes of the $Ni_{80}Fe_{20}$ $/Sm_{40}Fe_{60}$ $/Ni_{80}Fe_{20}$ trilayers and $Ni_{80}Fe_{20}$ $/Sm_{40}Fe_{60}$ bilayers by a theory using a simple model, where the controlling parameter is the thickness of the soft and hard layers. In the paper by Guo et al. [23], [24], they claimed that when the anisotropy energy of the soft layer is not small, it also plays an important role in the determination of the switching field. Zambano et al. [25] explored diverse material systems such as $CoPt/Fe_xCo_{1-x}$ $(0 < x < 1)$, $CoPt/Ni$, $CoPt/Fe$, and Sm_2Co_7 $/(Fe, Co, or Ni)$. They investigated the effect of the thickness and the composition of the soft layer with a fixed hard layer and concluded that the anisotropy energy of the hard layer, and the saturation magnetization of the soft layer, are the main factors that determine the nucleation field and coupling length.

1.2.1 Micromagnetic scale parameters

In micromagnetic, which is discussed in chapter 4, we define the energy of the system (magnetic material). This energy is a contribution of several energy terms, anisotropy energy, exchange energy etc. During the definitions, we find that there are characteristics constants of the magnetic system which which when put together, they make important length parameters.

The exchange stiffness constant A, with the dimension of (J/m^3), the uniaxial anisotropy constant K (J/m) and magnetostatic self energy $\mu_0 M_s^2$, gives us two fundamental constant of the dimension of length.

$$l_{ex} = \sqrt{\frac{2A}{\mu_0 M_s^2}} \tag{1.7}$$

l_{ex} is called the exchange length, is of prime importance as it governs the width of the transition between magnetic domains [26].
For a hard magnetic material, having strong crystalline anisotropy, the domain wall is of Bloch type, named after physicist Felix Bloch. A *Bloch wall* is a narrow transition region between magnetic domains, over which the magnetization changes its value in one domain to that in the next. Bloch walls appears when the size of the particle is larger than the domain wall width. The shape of Bloch wall is result of the competition between the anisotropy energy and exchange energy.

$$l_w = \sqrt{\frac{A}{K}} \tag{1.8}$$

Eq.(1.8) determines the width of the domain wall differentiating magnetic domains with different magnetization. Domain wall formation is energetically favorable but it costs domain-wall energy. The wall energy in a spherical two domain particle of radius R, is given by $4\sqrt{AK}\pi R^2$ and the gain in the magnetostatic energy is half the single domain energy i.e. given by $\mu_0 M_s^2 V/12$ [27]. Domain formation in spheres is favorable for particles whose radius exceeds a critical single domain radius, R_{sd}

$$R_{sd} \approx \frac{36\sqrt{AK}}{\mu_0 M_s^2} \tag{1.9}$$

This value varies between a few nm in soft magnets and about 1 μm in very hard magnets. When the radius of the soft magnetic particle is smaller than the l_w, then the wall covers the whole particle.

1.2.2 Architecture of exchange spring media

The challenge in producing high performance ESM, is the difficulty to control the spacing of the particles and the coupling between them. The synthesis requires careful creation of both hard and soft materials on nanomertric scale (< 10 nm), and control over the separation between hard and soft particle [28]. This separation between the particles should be smaller than the Bloch wall length, which is the distance over which the alignment of moments can flip. [US 2013/0257572 A1].

In order to achieve a better properties of the exchange spring media, it is very important to understand the different possible architecture from the hard and soft magnetic phase. There are many types of magnets, two phase nanostructures, having a variety of application in the field of permanent magnets, sensors, spin electronics, and, more recently, magnetic recording. The nanostructures occur in many variations and geometries, including but not limited to multilayers and granural composites. Here we focus on hard-soft two phase nanostructures, characterized by a local anisotropy K in combination with a common easy axis $(\mathbf{e}_z)$.

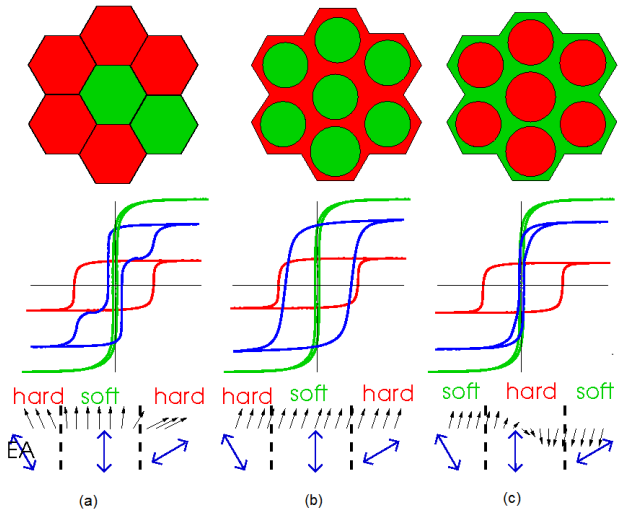

Figure 1.10: Schematic for exchange spring hard-soft nano-structures and its corresponding magnetic behavior. Figure (a) Layered structure, (b)Soft inclusion in Hard matrix and (c) Hard inclusion in soft matrix.

An important thing to note is that the particle size play an important role in deciding the properties of a magnetic material. The addition of the soft phase must be realized carefully, because coercivities $H_c < M_s/2$ are harmful to the energy product. The total magnetization is equal to the volume average of the magnetizations of the two phases, but this is not necessarily true for other quantities, such as the exchange stiffness and the coercivity [27].

For the system with large particles, the magnetostatic energy overcompensates the increase in exchange energy. Big particles are more likely to contain imperfections harmful to coercivity, so coercivity tends to decrease with increasing particle radii $R >> l_{ex}$, R being the radius of the particle. Very small particles have a low coercivity due to superparamagnetic excitations.

Among the possible structures, we currently focus on three main architectures as shown in fig.1.10. In the figure, (a) represents the architecture of a layered structure, (b) represents Ceramic-matrix composite or soft inclusion in hard system and (c) represents the Metal-matrix composite or hard inclusion in soft system.

1. Layered structure:
   In layered structure, the soft phase and the hard phase is exchange coupled only at the interface. The coercivity, predicted from the micromagnetic energy equations, varies as $1/L^2$ as a function of the soft layer thickness L. For large values of L, the soft phase switches easily and this coercivity reduces. This initiates the magnetization reversal of magnet and gives rise to unfavorable "wasp-like" hysteresis-loop shape. The corresponding switching of the soft regions is also known as exchange-spring magnetism [12].

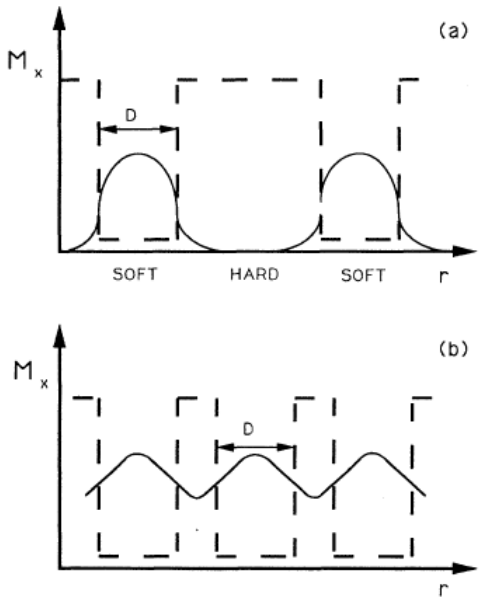

Figure 1.11: Diagram showing the effect of interaction between different soft regions. (a)Large distance between the soft inclusions leads to exponential decrease in the magnetization in hard region. (b)Smaller distance between the soft inclusion leads to reduction in coercivity. [10]

2. Soft inclusion in Hard:
   In the case of single grain structure, we assume an ideal soft inclusion (diameter D and anisotropy of soft phase $K_s = 0$) in hard matrix. The magnetization of both the phases is initially assumed to be aligned. On application of external field the state of the magnetization of the soft inclusion changes but come to a step below $D \approx l_{w-h}$, where l_{w-h} is the domain wall width of the hard phase. For example, for a system $Sm_2Fe_{17}N_3$ with inclusion of diameter $D \approx 3\ nm$ will have coercivity equal to anisotropy field of matrix ($\approx 20\ T$). For $D = 7\ nm$, the coercivity remains as high as $7\ T$. With larger inclusions, the coercivity falls of as $1/D^2$ [10]. In order to obtain higher remanence, a large number of inclusions per unit volume is needed.

   If the space between the neighboring regions gets too small, the soft region interacts and the coercivity gets destroyed as described in fig.1.11. When the distance between the soft inclusion is small, the magnetization mode tunnel through the hard region. The exchange interaction reduces the coercivity if the width of the hard phase is less than l_w.

   The challenge from the point of view of synthesis or realization of these magnets is to have smaller size of the soft regions in order to avoid nucleation at smaller field.

3. Hard inclusion in Soft:
   From the random anisotropy model, which assumes an assembly of randomly oriented and ferromagnetically coupled grains, one can determine the mean asniotropy of the system with a volume V. The volume is assumed to be equal to cube of exchange length $l_{ex} = (A/ < K >)^{1/2}$ [29]. The mean anisotropy for $D << l_{ex}$ is given as:

$$< K >= K_1^4 \cdot D^6/A^3 \tag{1.10}$$

   If the grain size exceeds exchange length, magnetocrystalline anisotropy is deter-

mined by the full magneto-crystalline anisotropy K_1. The coercivity is maximum when $D \approx l_{ex}$. If the grain exceeds domain wall width, $l_w = \pi l_{ex}$, the coercivity decreases proportional to $1/D$, which is case here.

1.2.3 Magnetization reversal in ESM

Chakka et al. [30], published their study about the effect of coupling strength of ESM on magnetic properties. They studied magnetization reversal in a ferromagnetically coupled hard-soft bilayer. With the main focus on the coupling constant J, it is shown that there are 2 distinct type of magnetization reversal mechanisms: Type I and Type II.

Let the magnetization, M, anisotropy constant, K and the thickness of the hard and soft layer t; are denoted with the subscript s, h for soft and hard phases. The energy of the soft phase is given by E_s, and E_h is the energy of the hard phase and $E_{exchange}$ is the coupling energy between them. There are three main barriers controlling the magnetization reversal: E_{B-s}, the energy barrier that needs to overcome for reversal of M_s, E_{B-h}, the energy barrier that needs to overcome for reversal of M_h after the reversal of M_s, and E_{B-sh}, the energy barrier that needs to overcome for reversal of both M_s and M_h.

Type I reversal: When applied field H increases, the energy of the system increases. At the coercivity of the soft phase, E_{B-s} vanishes and M_s reverses. With further increase of H, at the coercivity of hard phase, E_{B-h} vanishes and M_h reversal occurs. This is a two step reversal process, and the hysteresis shows a kink, fig.1.12. It means that the soft phase magnetization is not tightly coupled to hard phase. Therefore M_s and M_h reverse in two steps. When J is increased to a critical value $J_c(I)$, both the energy barriers E_{B-s} and E_{B-h} vanish simultaneously at a particular reverse field $H_c(I)$. At this field simultaneous reversal of both the phases occur in one step, and the hysteresis does not show a kink.

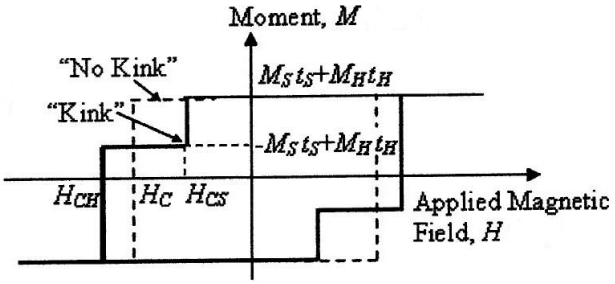

Figure 1.12: Schematic of hystersis loop for a ferromagnetic exchange coupled bilayer, with and without kink. No kind condition is obtained by increasing the coupling strength J.

Type II reversal: When H is increased in reverse direction, depending on the parameters, M, K and t and J; the energy barrier E_{B-sh} can vanish before E_{B-s}. In this case, both the phases can reverse in one step process. The coupling is denoted by $J_c(II)$, and corresponding applied field $H_c(II)$.

The expression for the critical coupling constant is derived analytically in [30]. Type II reversal is the typical kind of reversal seen in ESM.

1.3 Exchange spring media in magnetic recording

Exchange spring magnets plays a significant role in contribution to the energy applications of magnets. Being a prospective candidate for enhancing the energy product, ESM has applications in the domain of magnetic recording and storage technologies (Magnetic Random Access Memories(MRAMS)). ESM also offers a solution for the overcome the "recording trilemma", a major challenges that is faced today in the recording technology.

Garcia-sanchez et al. explains, by micromagentic modelling, that ESM is the most probable way to reduce the switching field in the magnetic memories. ESM could not only make it easier to write the data on the storage devices but also maintain the thermal stability [31].

Magnetic recording technology

Magnetic recording is very important application in field of nanotechnology. The challenges in the magnetic recording technologies viz. the signal-to-noise ratio (SNR), thermal stability and the write-abilty are being referred to as "Recording Trilemma" fig. 1.13 [32].

The demand for smaller (in physical dimensions) storage devices with higher storage capacity grows day by day. Due to increase in the density and reduction in grain size, thermal stability of the device becomes very important. The bits are made smaller and the media is made thinner. In order to increase the performance of the media. it is necessary to increase the grain density, this can be explained in terms of signal to noise ratio (SNR). The SNR can be related to the number of grains N in a bit, of the media by the equation SNR$= 10log(N)$ [33]. More the number of grains, higher is the SNR and the output is more reliable. But if one wants to decrease the bit size and keep high number of grains, the solution is to reduce the grain size, i.e. reduction in the volume V of the grain size. However this leads to difficulty in thermal stability and write-ability.

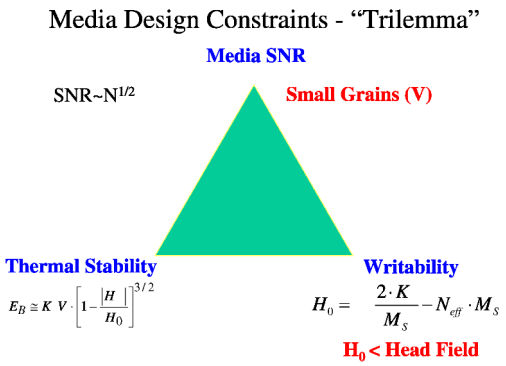

Figure 1.13: Demonstrates the 3 prominent challenges in recording technology interconnected to one another.

Information in the grains is stored by switching the state of magnetization. The two magnetic states are separated by an energy barrier and the reduction of grain size reduces the energy barrier KV, between the two states [34]. K is the magnetocrystalline anisotropy constant. The head field in the storage/ recording device provides the necessary energy to overcome the barrier for magnetization reversal. If the energy barrier is comparable to the thermal energy, magnetization becomes unstable and magnetic fluctuations occurs and this is called superparamagnetic effect. The energy barrier, given by

$$E_v = \frac{KV}{K_B T} = KV\left(1 - \frac{H}{H_0}\right)^{3/2} \tag{1.11}$$

where H is the external magnetic field which assists the magnetization reversal and H_0 is the switching field. Therefore, in order to increase the energy barrier without compromising the grain volume V, the system should have higher anisotropy. Increase in the anisotorpy leads to difficulty in writing the data since the writing field available in the recording devices is limited. The write field should be higher than the switching field whose maximum limit is given by coercivty H_0,

$$H_0 = \frac{2K}{\mu_0 M_s} - N_{eff} \cdot M_s \tag{1.12}$$

For writing the data, the head field should be higher than the coercivity of the grains given by eq.(1.12). The maximum head field that can be achieved is reported to be $2.4T$ [35]. To overcome this challenges, new materials and methods are proposed for magnetic recording media:
(i) Hear/thermally assisted magnetic recording (HAMR) [36], [37],
(ii) patterned media,
(iii) tilted media,
(iv) microwave assisted magnetic recording technology (MAMR)[38].

In the current work we focus on the MAMR solutions applied to the Exchange Spring systems.

Microwave assisted magnetic recording

To overcome the "recording trimlemma", we focus on the method of microwave assisted switching. In microwave assisted switching technique, the media/system is subjected to an externally applied additional microwave magnetic field. The microwave field exerts an additional torque on the magnetization of the grains, together with the head field.

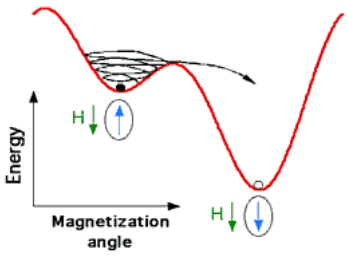

Figure 1.14: Potential energy of the magnetic nanoparticle versus magnetization angle. The potential energy has two wells corresponding to two stable orientation of the magnetization. For small applied fields, one of the two wells is metastable. An additional applied microwave field induces oscillations of the magnetization in the energy wells. When the microwave frequency matches the precession frequency of the magnetization, energy can be pumped into the system. This can lead to magnetization reversal from the metastable to the stable state when the precessional damping is not too high.

The initial state of the magnetization is in metastable minimum. On application of the microwave magnetic field, the grain starts spinning. The applied microwave field frequency matches the frequency of precession, the magnetization spirals up to the saddle point and reverses i.e. switches its state as shown in fig.1.14. Thus we can achieve the recording on

the disk media. This idea was proposed and experimented by Thirion et al. for a single nano particle [39].

In the magnetic recording techniques it is found that the perpendicular recording media provides additional advantage over longitudinal recording media[35].
Advantage of perpendicular media
The history of perpendicular recording started many decades ago, almost simultaneously with longitudinal recording. Many attempts have been made to develop a perpendicular recording system; however the industry was successful introducing new generations of longitudinal components, achieving high areal density [40]. The development of high density systems required complicated optimization of recording heads and media, consuming efforts of large groups of scientists and engineers. The few parts, which were produced never demonstrated any advantages over longitudinal recording components. The research in perpendicular recording was left to several university group and was not considered to be worth much of attention.

The situation around 2000, when it became clear that the potential of longitudinal media was about to be exhausted due to the superparamagnetic limit.

The longitudinal medium grains are oriented in the plane of the magnetic thin film and their diameter determines the recording layer thickness and the grain volume. However, the perpendicular magnetic medium grains are grown in a vertical direction. Therefore, they may have small in-plane diameter D and large volume, forming cylinder-like columns. The ratio of the in-plane diameter D to the grain height t can be about 5:1, supposedly resulting in low media noise and high thermal stability. This simple argument immediately results in an optimistic prediction approximately 5x density grain perpendicular recording medium over longitudinal. So main advantages of perpendicular over longitudinal is:

- High thermal stability- can be achieved by small in-plane grain diameter with cylindrical grain structure [41].
- The vertical pole head in a recording media with a soft underlayer can generate can generate twice the field of longitudinal recording head. This allows writing higher coercivity medium, further decreasing grain size and maintaining media thermal stability.
- The read back signal amplitude from perpendicular medium with soft underlayer is larger compared with equivalent longitudinal medium improving signal-to-noise ratio.
- Perpendicular media grains are strongly oriented. This results in smaller medium noise and a sharper recorded transition. The high orientation of the perpendicular medium also improves the side-track writing and edge noise.
- The demagnetization field in the perpendicular medium is smaller at the transition region. This allows writing narrower magnetic transitions and improves thermal stability of high density data (this is opp. To longitudinal medium). Also, the nonlinear transition shifts in the perpendicular medium are less critical, compared with longitudinal recording.
- The track edges in perpendicular medium are less noisy and better defined due to the vertical pole head configuration. Sharp track edges allow higher track density and a smaller bit aspect ratio.

1.4 Summary

In chapter 1, a general introduction about the history of magnetism is presented. A brief explanation of ESM is given in which we discussed the important characteristics used to describe ESM and its figure of merits such as *Energy Product*. We presented the literature review about the experimental work for the synthesis of ESM. The main challenge in the synthesis of ESM, is also discussed in details. The difficulty in controlling the size of the soft and hard phase inclusions in the matrix is one of the challenges in the architecture of the ESM. We discuss three important architectures, (i) Layered structure (ii) Soft phase inclusion in hard matrix and (iii) Hard phase inclusion in soft matrix. Their corresponding magnetization behavior is also discussed and we find that the most suitable architecture from the permanent magnet application point of view is the *soft phase inclusion in hard matrix*. This architecture is suitable for ESM because one can achieve highest energy product of the resultant magnet, and the magnetization behavior remains hard magnetic as the coercivity is not destroyed when the size of the soft inclusions is greater than domain wall width of hard phase. We also concluded that in order to obtain higher remanence, the density of soft inclusion should be large.

Application of ESM in magnetic recording technology is studied next and we discussed the problem of *recording trilemma*. The incongruity between the decreasing size of the recording material and thermal stability and the writability of the media was discussed in details. We focus on one of the solutions offered for this problem which is *microwave assisted magnetic recording* (MAMR), as one of our area of interest which we studied in details in the theoretical work of this research.

This chapter hence gives the basic introduction about why we are interested in the synthesis of ESM and its major challenges and what experimental work has been done in this respect. On the other hand, we also form the basis as to why are we interested in studying the MAMR which is done in the theoretical part of the work by studying the dynamics of magnetization of the system.

1.5 Plan of Thesis

Chapter 2 and 3, we discuss the experimental part of the work. In chapter 2, we discuss the synthesis of precursors, i.e. hard magnetic material and soft magnetic materials. The advantages and choice for the particular system of Hexaferrite and Permalloy and nano Iron is presented. We also explained the process of mixing of the hard and soft phases. The mixing of the 2 precursors is carried out using mechanical milling and ultrasonic mixing. We compare them on the basis of their structural characterization as a function of (i) mixing method, (ii)volume fraction of the phases.

Chapter 3 describes the next process in the formation of nanocomposite, i.e. sintering and compaction. First we discussed, the systems of mechanically milled mixtures, by studying their structural and magnetic properties. Similar discussions are carried out for the different systems of composites obtained by ultrasonic mixing. We compare the bulk magnets obtained form mechanical milling and ultrasonic mixing. We also study the magnetic properties of permalloy system as a function of the measuring temperature.

In the theoretical part, we stared with modeling the bilayer nanocomposite system using micromagnetics. In Chapter 4, we briefly introduce the fundamentals of micromagnetics. A general history about the origins of micromagnetics is given and the evolution of

the work from energy minimization to study the magnetization dynamics to the current state is discussed. A general concept of thermodynamics potential for magnetic body is presented and the important concept of Landau free energy $G_L(\mathbf{M}; \mathbf{H}_a, T)$ is introduced. Further we look into each energy contributing term, *Exchange energy*, *Anisotropy energy*, *Magnetostatic energy* and *Zeeman energy terms*. Equilibrium condition of the system is discussed using the Brown's equation and we arrive at two significant equations forming a significant advancement in the micromagnetics.

In chapter 5, we studied results of the numerical modeling. From the application point of view, a solution to the "recording trilemma", MAMR is also studied in chapter 5. The fundamental nature of magnetization dynamics was studied through magnetization reversal techniques. We discussed the numerical results obtained by solving the LLG equation. The LLG equation was solved by a new Fortran code using *finite difference technique*. This code was first tested on the systems with uniform magnetization for which the analytical solution had been worked out by Bertotti et al. By comparing the results of the analytical and the numerical solutions, we tested the code and the numerical solutions were found to be in agreement with the analytical solutions. By studying the dynamics in the uniform case we introduced the concept of stable rotating mode solution called the periodic mode solutions or the *P-mode* and the Quasi-periodic solution or the *Q-modes*.

We further framed a model for bilayer exchange coupled system similar to the one proposed by Asti et al. (which is the basis of out study) and we introduced the non-uniformity in the system due to the geometrical structure. We studied these system under an additional in-plane circularly polarized field. We showed that under the condition we used, LLG equation became highly non-linear and very complex in nature. The analytical solution have not been found until now. But we solved the LLG equation numerically using the code and studied the result for the a perfectly coupled hard and soft magnetic material.

CHAPTER 2
SYNTHESIS OF MIXTURE

Chapter 2

Synthesis of Mixture

Contents

2.1	Experimental techniques and equipment	**27**
2.1.1	Sample selection	27
2.1.2	Mechanical milling	27
2.1.3	Ultrasonic mixer	28
2.1.4	X-Ray diffraction	28
2.2	Precursors	**28**
2.2.1	Structural characterization of precursors	32
2.2.2	Magnetic characterization	33
2.2.3	Conclusion	36
2.3	Mixing	**36**
2.3.1	Structural characterization of the mixtures	37
2.3.2	Magnetic characterization	42
2.4	Conclusion	**43**

This chapter discusses the first step of synthesis process of permanent magnets of composite materials, i.e proper mixing of the precursors. Composite material consisting of two suitably dispersed ferromagnetic and mutually exchange-coupled phases, one of which is a high anisotropy magnetic phase in order to provide a high coercive field, while the other is a soft magnetic phase just providing a high saturation M_s, and should envelop the hard phase regions in order to prevent their corrosion. A general theoretical treatment of such systems shows that one may expect apart from a high energy product $(BH)_{max}$, two uniquely characteristic features, a reversible demagnetization curve (exchange-spring) and, in certain cases, an unusually high isotropic remanence ratio B_r/M_s [12].

There are many types of magnetic two phase nanostructures, with a variety of applications in permanent magnetism, soft magnetism, sensors, spin electronics, and, more recently, magnetic recording. They occur in many variations and geometries, including but not limited to multilayers and granural composites. Here we focus on hard-soft two phase nanostructures, characterized by a local anisotropy in combination with a common easy axis.

The impact of microstructure on the magnetic properties of nanocrystalline materials is reported by Herzer [42], [29]. Theoretically the critical dimensions of the phases for composite permanent magnets are estimated and discussed using corresponding models of microstructures. On that basis, the typical magnetic properties of such composites

are derived by kneller and Hawig, [12]. Fig.1.10 shows schematic realization of hard-soft nanostructures.
In this synthesis, the hard magnetic phase used is *Barium hexaferrite* ($BaFe_{12}O_{19}$) and for the soft magnetic phase, iron and some metallic alloys of iron, namely iron-nickel, iron-cobalt are used.

2.1 Experimental techniques and equipment

2.1.1 Sample selection

All the precursors involved are weighted carefully and mixed by volume in order to make the necessary composite.

For the hard magnetic phase, Barium hexaferrite ($BaFe_{12}O_{19}$) is used. It constitutes major fraction of world tonnage of permanent magnets. They are used where "Energy per unit weight and "cost are important considerations. Hexagonal ferrites have high uniaxial anisotropy, $K = 3 \times 10^5\ J/m^3$, easy axis along hexagonal c axis. Since the saturation is small, the anisotropy is sufficient to overcome the magnetostatic energy and give perpendicular magnetization in either flat hexagonal plateletes that can be grown from solution or in (0001) textured thin films. They have:

- Smooth surface
- Nonmetallic electrical properties
- Superior corrosion resistance
- High volume density of magnetic materials achievable in thin films (advantage for high-density recording)

The metallic alloy that we chose for the synthesis of composite : Fe as it has higher magnetization and the permalloy, $Fe_{25}Ni_{75}$, is found to be chemically more resistant to oxido-reduction reaction therefore more possibility of forming composites with better magnetic properties [43].
$Fe_{50}Co_{50}$ is particular interesting because of its magnetic properties. It has high curie temperature, a very high saturation magnetization, high permeability [44],[45].

2.1.2 Mechanical milling

The comminution of the samples is performed by high-energy impacts from grinding balls and friction between balls and the grinding bowl wall. The main aim of milling is to reduction of the particle size, mixing or amalgamation of the powders.

All mixing is performed on FRITSCH Planetary micro mill PULVERISETTE 7 classic line, at $400rmps$. Powder to balls ratio is always kept constant and is $10:1$ and few drops of ethanol are used to aid the milling process. Milling time is the variable parameter.

Figure 2.1: Planetary ball mill used to mix the precursors.

2.1.3 Ultrasonic mixer

For mixing, Sonoplus ultrasonic mixer is used. The powders were taken in a beaker with ethanol. The power of the mixer is always kept between $55\% - 58\%$ (max. power 200 W)and mixing time is kept constant for 10 minutes.

Figure 2.2: Ultrasonic mixer courtesy: Bandelin electronics.

2.1.4 X-Ray diffraction

X-ray diffractograms have been obtained using PAN-alytical X'Pert Pro equiped with linear detector. It used cobalt $k\alpha$ radiation $(1.76)\mathring{A}$.

2.2 Precursors

Hard magnetic phase

Ba (M-type) hexaferrite (BaM) has magnetoplumbite structure and a stoichiometry of $BaFe_{12}O_{19}$ [46]. The magnetoplumbite structure has 32 atoms per formula unit and 64

atoms in a single unit cell, fig.2.3. BaM is a ferrimagnetic material. A ferrimagnetic material is one which in general is composed of two sublattices **A** and B separated by oxygens. In a ferrimagnet, the magnetic moment of lattices A and **B** are not equal but are anti parallel to each other, therefore resulting in a net magnetic moment.

One property of BaM compound that is of particular value in microwave device design is the strong uniaxial anisotropy field with the magnetic easy direction being along the c-axis ($H_A \sim 17,000Oe \sim 1.7T$) [47]. The high magnetic anisotropy field can be adjusted by using an appropriate substitute for the Fe ion, which allows for the tuning of resonance frequencies from 1-100 GHz [48]. This degree of freedom makes BaM a choice material for many monolithic microwave integrated circuit (MMIC) applications. BaM media also provides mass producible perpendicular media, high recording density and also have good oxidation resistance [49].

The structure consists of seven ferric ions distributed onto five inequivalent interstitial sites (one trigonal bipyramidal, two octahedral and two tetrahedral). The magnetism arises from the super-exchange interaction between ferric cations mediated by the oxygen anion. This is a negative exchange interaction (i.e., antiferromagnetism), with an amplitude from each Fe-O-Fe pairing dependent on the angle made between the ferric cations and oxygen (i.e., a larger exchange occurs with larger angles). The saturation magnetization is reported to be $317.7kA/m \sim 0.4T$ with a Curie temperature of $450°C$. This compound is stable in air. Magnetic moment is $20\mu_B$ [50]. It's melting point is $1300°C$, and has specific gravity (the ratio of the density of a substance to the density of a reference substance)of 5300 kg/m^3 at $20°C$.

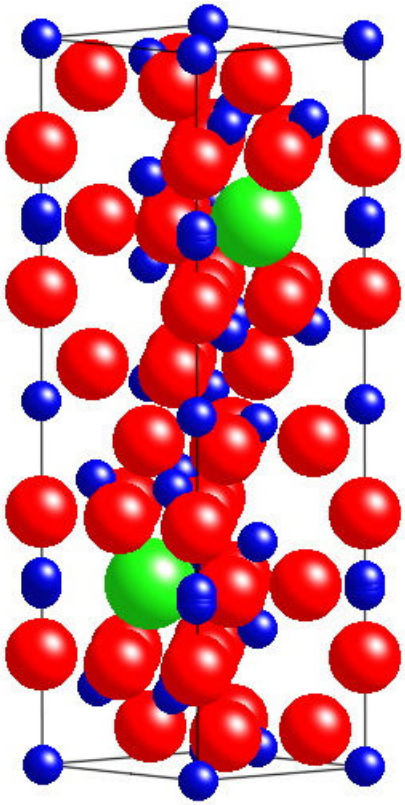

Figure 2.3: Shows magnetoplumbite structure ($BaFe_{12}O_{19}$), Fe-Blue, Ba- Green, O-Red, courtesy:CrystalMaker Software Ltd.

The symmetry is $P63/mmc$; the unit cell whose dimensions are $a = 0.5893\ nm$ and $c = 2.3194\ nm$, contains two formula units. The structure is built up of ten close-packed (both cubic and hexagonal) layers of barium and oxygen atoms. The sequence of the layering in the c axial direction is $BAB'ABCAC'AC$. The primed letters denote layers consisting of one barium to three oxygen atoms. The details of the structure can be found in [51].

BaM bulk compacts are produced by sol-gel method as described in reference [52] and [53]. Barium hydroxide, iron nitrate and citric acid are used as precursors. All materials are taken in required quantities. Iron nitrate is dissolved in deionized water and iron-hydroxide precipitate is formed using ammonia solution.

$$Fe(NO_3)_3 + 3NH_4OH \longrightarrow Fe(OH)_3 + 3NH_4NO_3 \tag{2.1}$$

In fact the NH_4 group make the compound neutral. The precipitate is filtered and washed with water. Citric acid is added in appropriate quantity and the solution in water is continuously stirred at $60°C$. Barium hydroxide is added and the solution is stirred to let the water evaporate at $80°C$. The residue obtained is the gel which is then dried at $150°C$ for 2 hours for removal of organic matter and further calcinated at $900°C$. The obtained brown powder is the M-ferrite. Temperature dependent properties are reported by Shirk et al [54].

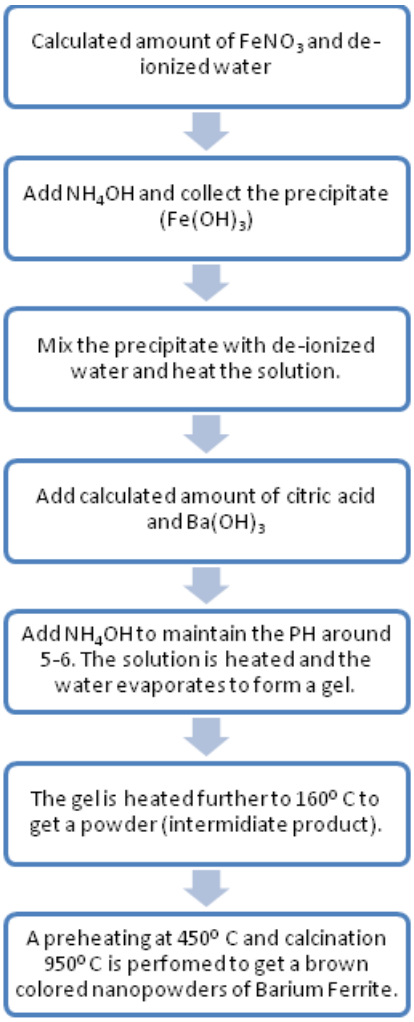

Figure 2.4: Flow-chart representation of the sol-gel process for Barium hexa-Ferrite.

Soft magnetic phase

The 3 metallic alloys used for the synthesis of the composite are discussed in details here.

1. *Iron*

By far, iron constitutes one of the major elements in the earth's crust. Iron has BCC crystal structure, fig.2.5. The nanopowder of iron was used here for the synthesis of the bulk composite. Some physical and magnetic properties of iron at room temperature [55]:

- density:7870 kg/m^3.
- curie temperature:$T_c = 770°C$
- saturation magnetization $M_s = 1.72\ A/m$ $(= 2.16\ T)$.

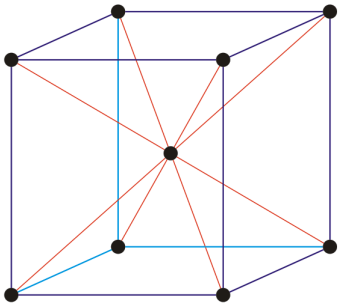

Figure 2.5: Fe has body centred cubic lattice structure, Fe atoms at the corners and in the center(in Blue)

2. *Iron-Nickel*

Use of iron-nickel alloy is know since very long time. Permalloy (with composition of 20% Iron and 80% Nickel) was first invented by physicist Gustav Elmen at Bell Telephone Laboratories. Addition of nickel to iron increases the strength and corrosion resistance of the metallic phase. It has a face-centered (FCC) structure. In this case we use a particular composition of iron-nickel, $Fe_{25}Ni_{75}$ for which the lattice parameter a, calculated from the x-ray diffraction is 0.288 nm with density of 8550 kg/m^3 at room temperature. [56].

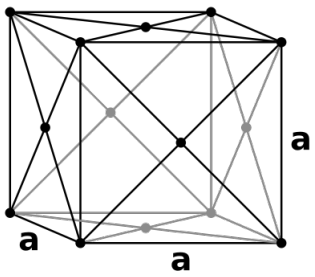

Figure 2.6: FCC structure as of FeNi.

Nano-powder for the composition $Fe_{25}Ni_{75}$ were prepared by cryogenic melting medium,details of which can be found in [57]. This technique uses a phenomenon of torque between the

evaporation of metal at high temperatures and rapid condensation by passing through a cryogenic liquid [58].

2.2.1 Structural characterization of precursors

The structural analysis of the precursors i.e. Barium hexaferrite and the soft magnetic materials, $Fe_{25}Ni_{75}$, Fe is discussed here.

XRD Analysis

Barium hexaferrite diffarction pattern is characterized by its two main peaks at $2\theta \sim 38°, 40°$. The patterns are indicative of the crystalline nature of the samples. The XRD pattern of the commercial ferrite is shown in black in fig.2.7. From the analysis we determined that the crystallite size is $176.2nm$ and cell parameters are : $a = 0.589\ nm$ and $c = 2.323\ nm$.

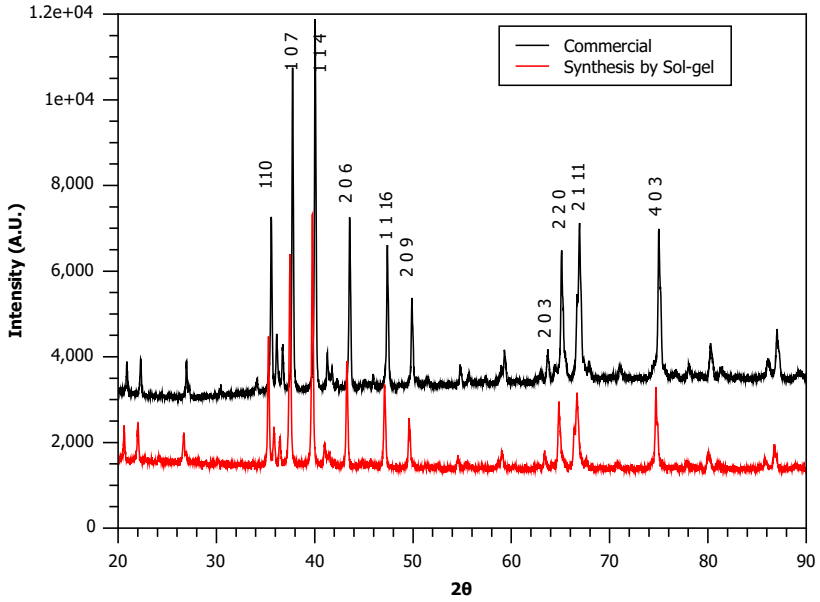

Figure 2.7: X-Ray diffraction pattern for *BaM powder* form synthesized by sol-gel (in red) and for *commercial ferrite* (in black).

The barium hexaferrite nano powder prepared by sol-gel method shown in red in fig.2.7 are also analyzed. The peaks are slightly broader than the peaks obtained from the commercial ferrite. This is because of the reduction in the crystallite size in the powder prepared by sol-gel, which is determined to be $143.7nm$. The lattice parameters are found to be $a = 0.589\ nm$ and $c = 2.322\ nm$ and space group $P63/mmc$. The sol-gel prepared powders have the same lattice parameters as commercial ferrite and the crystallite size is smaller, which is very desirable in the synthesis of nanocomposites.

The diffractogram for $Fe_{25}Ni_{75}$ is shown in fig.2.8. The crystallite diameter is calculated to be 30 nm with the lattice parameter $a = 0.3546\ nm$. The lattice structure is FCC. There is a formation of oxide layer around the nanopowder [59].

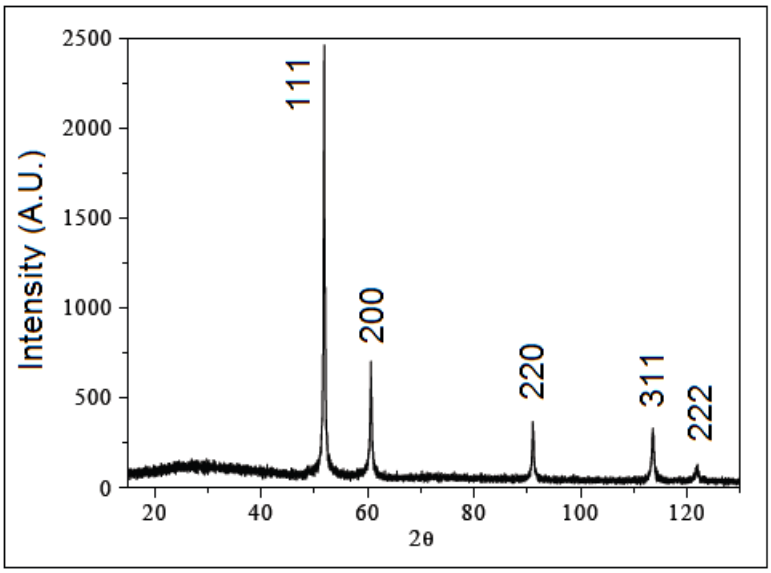

Figure 2.8: Diffraction pattern for the nanopowder of $Fe_{25}Ni_{75}$.

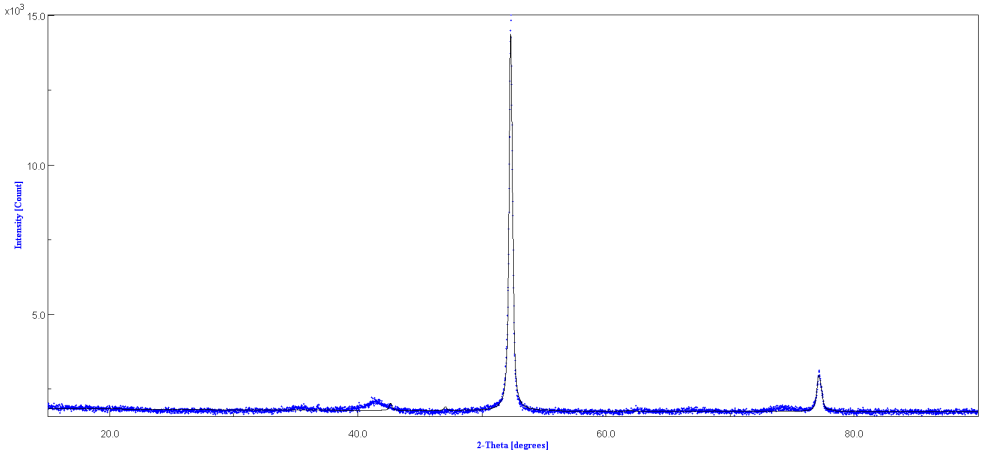

Figure 2.9: X-Ray diffraction for *Iron nano powder*.

Fe nanopowder's diffraction pattern is shown in fig.2.9. Crystalline size from the analysis is calculated to be $65.7nm$ with the cell parameter $a = 0.286\ nm$. A presence of another phase maghemite (Fe_2O_3) is also observed which occupies 16% of the total volume with the lattice parameters $a = 0.84\ nm$ and $c = 0.82\ nm$.

2.2.2 Magnetic characterization

A solid sample of commercial barium hexaferrite is characterized in the laboratory using VSM system. The characteristics of the commercial ferrite are compared with the laboratory prepared barium hexaferrite (BaM) samples, fig.2.10. The bulk ferrite from the nanopowder is prepared using spark plasma sintering method, under the pressure of $50MPa$ in Ar atmosphere in graphite die. The sintering is done for 10 min at a constant temperature of $800°C$ with a heating rate and cooling rate of $160°C/min$. The sintered

BaM is obtained in a compact form of the dimension of 8 $mm \times 1\ mm$.

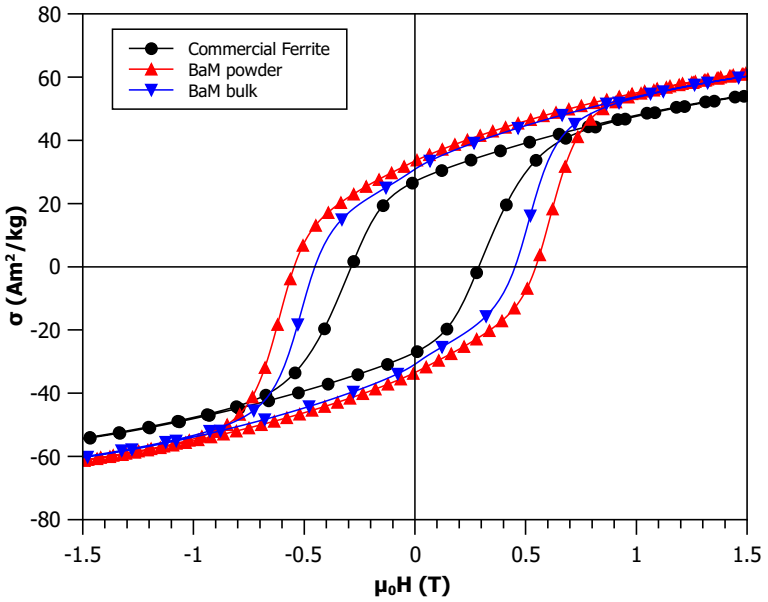

Figure 2.10: Comparison between the hysteresis loop for commercial ferrite (in black), laboratory prepared *BaM powder* and *bulk sample* sintered at 800° C (in red and blue respectively).

Comparison of coercivity, saturation magnetization and remanence of the Barium hexaferrite powder, sintered and commercial is presented in table.2.1 respectively.

Name	Sintering Temperature ($°C$)	$\mu_0 H_c\ (T)$	$\sigma_s\ (Am^2/kg)$	$\sigma_r\ (Am^2/kg)$
powder	-	0.546	64.138	33.460
SPS550	550	0.517	58.429	34.438
SPS800	800	0.452	61.726	30.840
commercial	> 1000	0.2879	56.30	27.04

Table 2.1: Comparison of parameters in the various samples of Barium hexaferrite.

It is observed from the figure and the table that the nanopowder prepared by the sol-gel method have better characteristics than the commercial ferrite. We also find that the coercivity reduces with the increase in the sintering temperature. The remanance also reduces for the bulk samples. The magnetic saturation is slightly reduced after sintering, the hexa ferrite powder have highest saturation magnetization which is equal to 64.14 Am^2/kg. The table also shows the parameters for the ferrite sintered at $550°C$ which we will be using later in the synthesis. Here we just show that when sintered at lower temperature the bulk ferrite shows improved coercivity than the one sintered at $800°C$.

One of the prime soft magnetic phase we used is $Fe_{25}Ni_{75}$, which has the following hysteresis loop, fig.2.11. We observe that the curve is very well saturated and the measured magnetic parameters are, saturation magnetization $\sigma_s = 95.193\ Am^2/kg$, coercivity $\mu_0 H_c = 0.0346\ T$ and the retentivity $\sigma_r = 22.757\ Am^2/kg$. Similar properties are found in literature for ultrafine particles of Fe-Ni alloys [60].

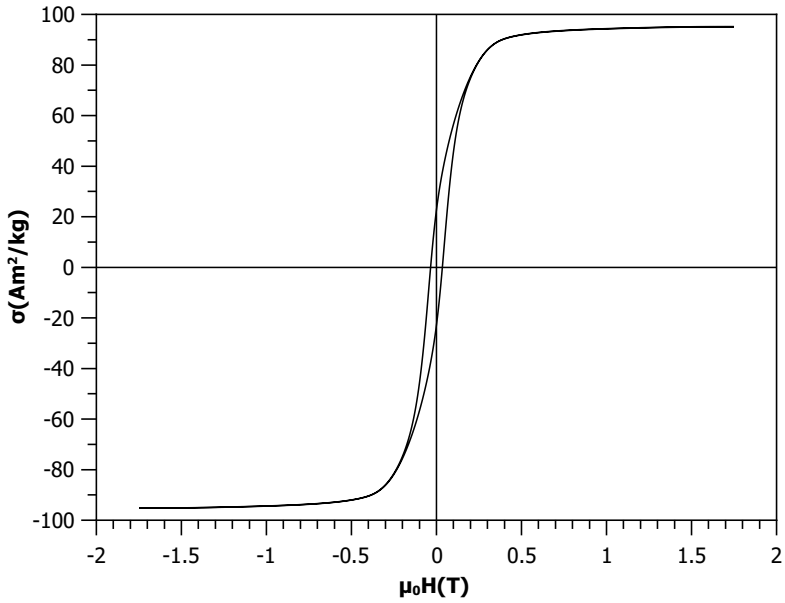

Figure 2.11: Hysteresis loop for the nanopowder of $Fe_{25}Ni_{75}$.

The permalloy powder were sintered at $500°C$ and $550°C$ and the magnetic properties are reported in the table.2.2.

Name	Sintering Temperature ($°C$)	$\mu_0 H_c$ (T)	σ_s (Am^2/kg)
powder	-	0.0346	95.193
SPS550	550	0.01	90.582
SPS500	500	0.01	84.352

Table 2.2: Comparison of parameters in the various samples of $Fe_{25}Ni_{75}$.

The hysteresis for nano powder of iron is shown in fig. 2.12. The loop is soft magnetic and as can be seen the iron nanopwder has high saturation magnetization of $170 Am^2/kg$ which is very close to the value found in literature [61].

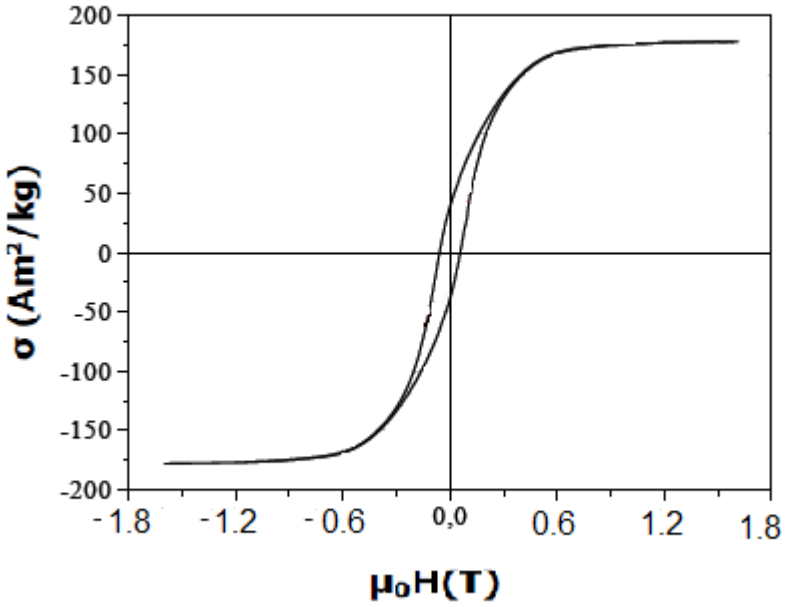

Figure 2.12: The magnetic hysteresis loop for Fe at room temperature.

2.2.3 Conclusion

We presented the properties of the precursor phases used in the synthesis of the mixtures, i.e. barium hexaferrite, permalloy and iron. The following properties are experimentally observed.

- Hard magnetic phase, barium ferrite powder was synthesized by sol-gel method. The as prepared powder have an advantage of crystallite size 146 nm smaller than the commercial ferrite. Also saturation magnetization of the prepared powders, M_s is found to be 64 Am^2/kg with a coercivity of $H_c = 0.54\ T$ higher than the commercial ferrite.
- Soft magnetic phase, iron nanopowder was found to have no significant presence of impurity upon structural characterization. The crystallite size was calculated to be $64nm$ and saturation magnetization 170 Am^2/kg.
- Iron-Nickel alloy composition used as precursor is $Fe_{25}Ni_{75}$ which has $M_s = 95$ Am^2/kg and $H_c = 0.035\ T$.

2.3 Mixing

The very first step for synthesis of exchange spring is mixing of the precursors. This section details the method of mixing and characterization of the mixed samples. Table.2.3 show the naming scheme used to indicate the prepared mixtures. Since in all the mixtures we always use the same magnetic hard phase of barium hexaferrite, it is not mentioned in the naming scheme. The first letter of the sample name indicates soft magnetic phase used. The second is a number, indicating the volume percent content of the soft phase mixed in the other phase. The third letter is an indication of the method of mixing, H stands for Hard milling and U for ultrasonic mixing (the two methods used for mixing). The remaining prefixes will be added according to the variation in the parameters of milling

time and others, which will be indicated as and when they appear in the following sections and chapters.

Metal-Name	prefix	Mixing method	variation parameter
Fe	F	H	Milling time
$Fe_{25}Ni_{75}$	N	H and U	Milling time

Table 2.3: Naming of the series of the samples

The nano powder of Barium hexaferrite and various metals (soft magnetic phase), are mixed together according to the volume fraction. The physical characteristics of these phases that are relevant here are given in table.2.4.

Name	$Mass(g/mol)$	$Density(kg/m^3)$	$Volume(10^{-6}m^3)$
$BaFe_{12}O_{19}$	1111.46	5290	210.1
$Fe_{25}Ni_{75}$	57.839	8480	6.8
Fe	55.84	7870	7.09

Table 2.4: Specific characteristics of precursors.

2.3.1 Structural characterization of the mixtures

Mechanical milled samples

First the mixture of barium hexaferrite and $Fe_{25}Ni_{75}$ are studied. The mixture is prepared by milling the two powders with the soft magnetic phase mixed in $2, 5$ and 10 percent by volume. The milled powders were analyzed by X-ray diffraction. Diffractogram for sample $N2H$ is given in fig.2.13. The 2 major peaks of BaM are very prominent in the diffraction pattern and hence confirm its existence. The volume of each phase in the mixed powder is determined from the analysis, 96.7% for BaM and 3.3% for iron-nickel alloy.

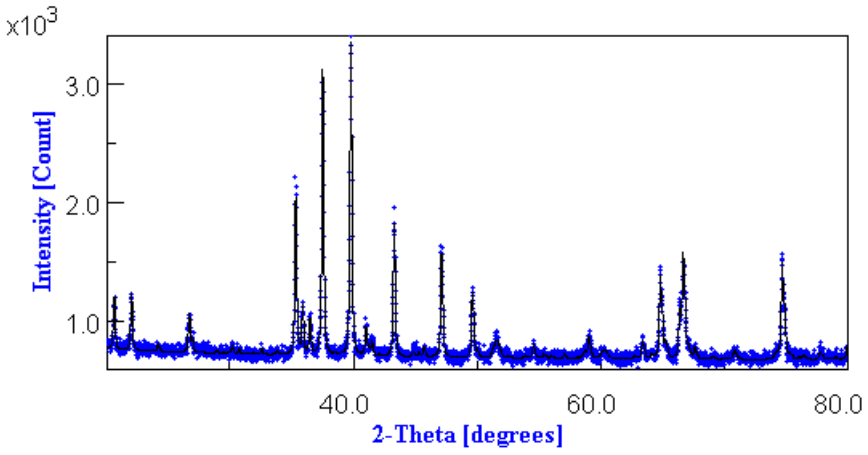

Figure 2.13: XRD pattern of $N2H - 25$ minutes, the mixed precursors milled for 25 minutes.

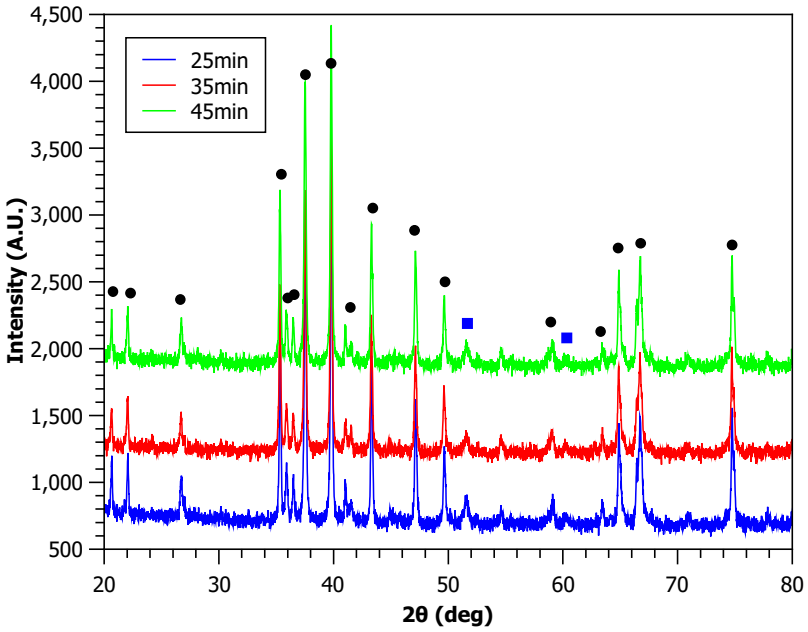

Figure 2.14: Diffraction pattern for $N2H-$ samples milled for 25, 35 and 45 minutes. Blue squares in the figure indicates the $Fe_{25}Ni_{75}$ phase.

For sample $N2H$ milled for 35 and 40 minutes, the diffraction pattern is compared in fig.2.14. The blue squares indicate the peaks for permalloy. The BaM phase and permalloy phase both are conserved during the mixing process. The intensity of the peaks increases with the milling time but the width almost remains constant.

The details of variation of the structural parameters obtained from the analysis are given in the table 2.5. From the table, it is found that the crystallite size does not vary much. The volume of each phase is conserved. Microscopic image of the surface is obtained form scanning electron microscopy. Mix of large and small grains (in grey) can be seen in the image, these are BaM grains and the ones in white are the grains of permalloy $Fe_{25}Ni_{75}$.

Sample Name	Phase	Volume content(%)	crystallite size (nm)
N2H-25min	BaM	96.7	141.8
	$Fe_{25}Ni_{75}$	3.2	99.9
N2H-35min	BaM	97.6	130.6
	$Fe_{25}Ni_{75}$	2.4	98.5
N2H-45min	BaM	97.7	139.4
	$Fe_{25}Ni_{75}$	2.2	98.9

Table 2.5: Variation in volume fraction and crsyatllite size for $N2H$ samples milled for different time.

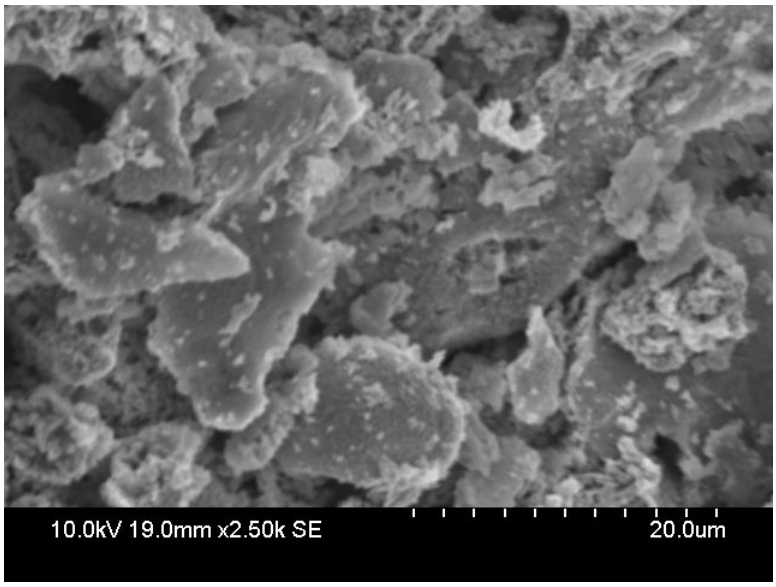

Figure 2.15: $N2H$ morphological view of the mixed powders.

For 5% volume fraction of $Fe_{25}Ni_{75}$ 5% in the mixture, diffraction pattern is shown in fig.2.16. Volume percent of hard and soft phases is 94.8 and 5.2 respectively. Crystallite size for hard phase is found to be $139.8nm$ and that of permalloy particles is $75.05nm$. The morphological image is shown in fig.2.17. One can see the mixture of big and small grains. The shape of the grains is not homogeneous.

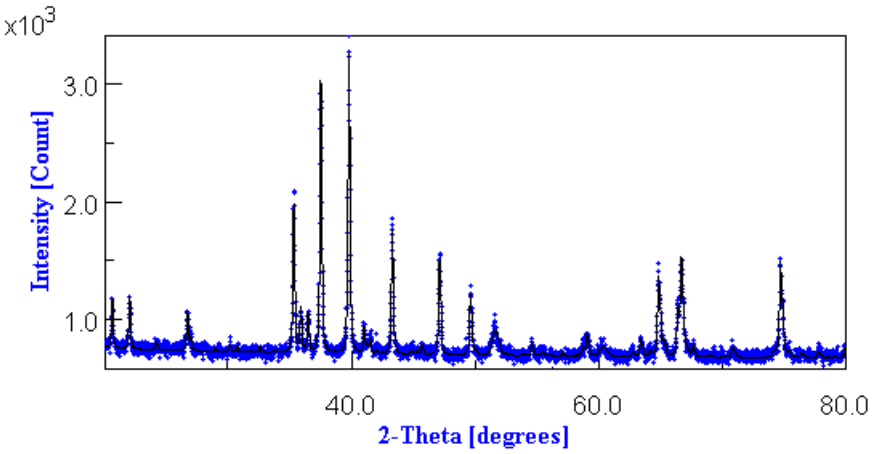

Figure 2.16: Diffraction pattern for $N5H - 35min$ powders; after milling for 35 mintues.

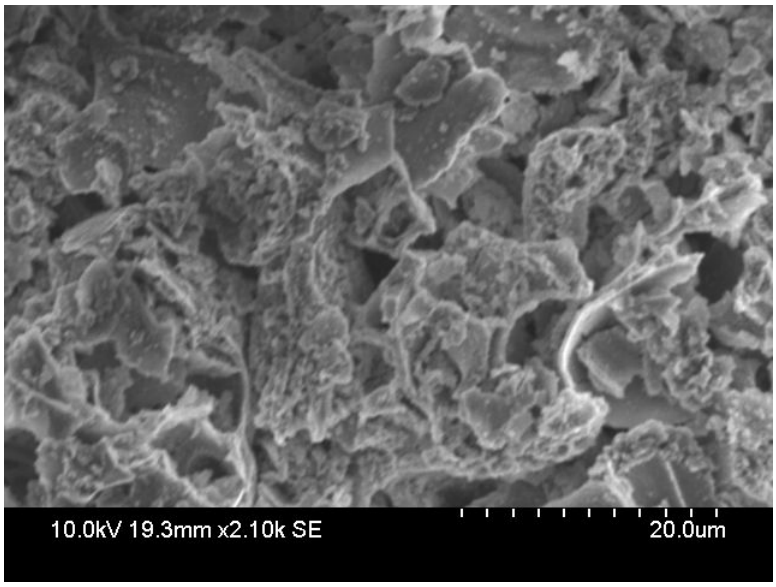

Figure 2.17: $N5H$ morphological view of the mixed powders.

Similarly the diffraction pattern for 10% volume fraction of permalloy has been analyzed, fig.2.18. BaM phase and permalloy phase is preserved during the mix and the volume of the phases found to be same as before milling. The SEM image is shown in fig.2.19. We can observe some pores have formed in the mixture and the overall size grains seems to be smaller.

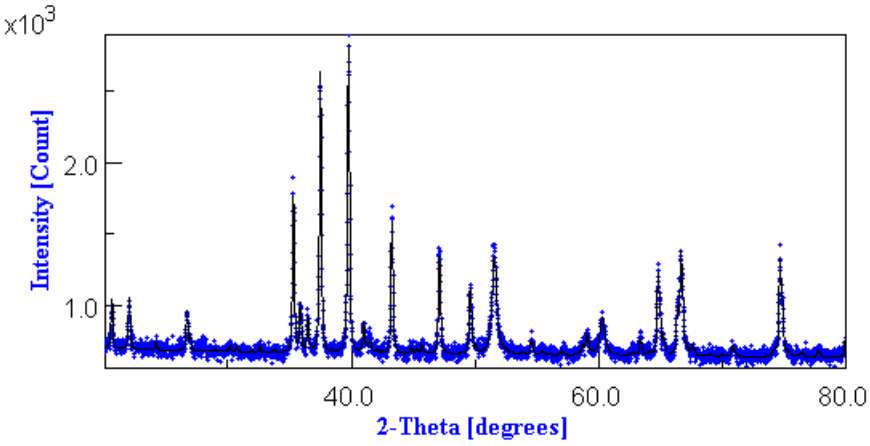

Figure 2.18: $N10H - 35min$ diffraction pattern, for milling time of 35 minutes.

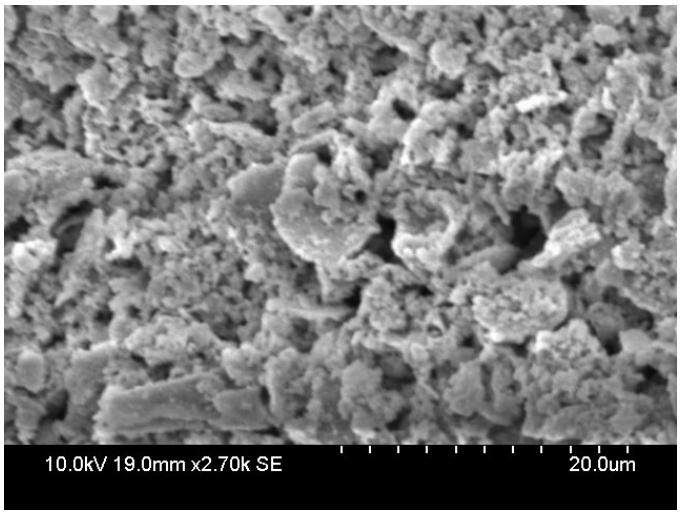

Figure 2.19: $N10H$ morphological view of the mixed powders.

The diffraction patterns are compared for variation in volume fractions in fig.2.20. It is observed that with the increase of soft metallic case the diffraction pattern differs only in intensity of $Fe_{25}Ni_{75}$, which is found to increase with volume fraction of the permalloy.

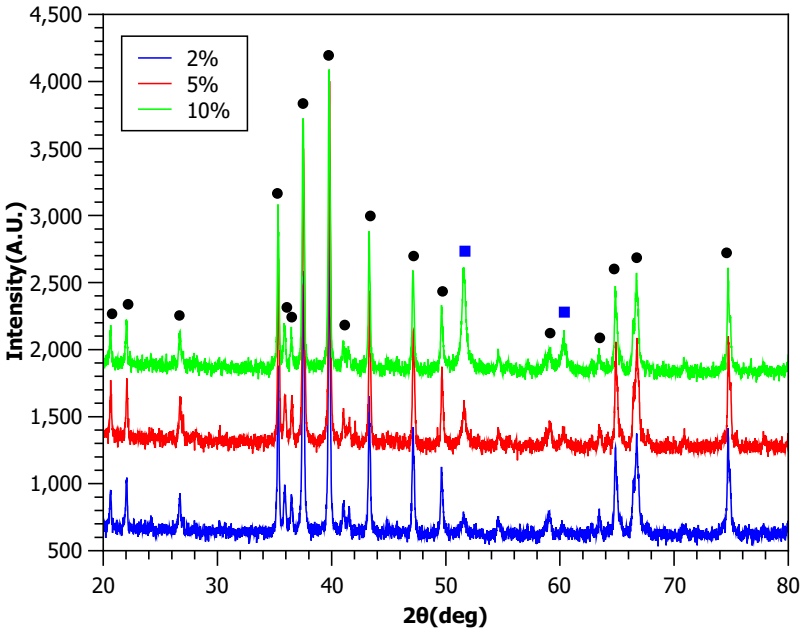

Figure 2.20: Variation in diffractogram for NXH series of samples, with the increase of soft metallic content in BaM. The blue squares indicates the rise in the peak height of $Fe_{25}Ni_{75}$ phase.

Ultrasonic mixed samples

The powders are mixed by ultrasonic mixing under ethanol for 10 minutes and later were heated to $60°C$ to evaporate ethanol. Diffraction pattern for 10% $Fe_{25}Ni_{75}$ mixed in BaM is shown in fig.2.21. From the analysis, the volume content of BaM is 90% and that of soft phase is 10%. No other phase is observed. And the crystalline size is slightly reduced and is determined to be $105nm$ and $68nm$ of hard and soft phases respectively. The SEM image can be seen in fig.2.22.

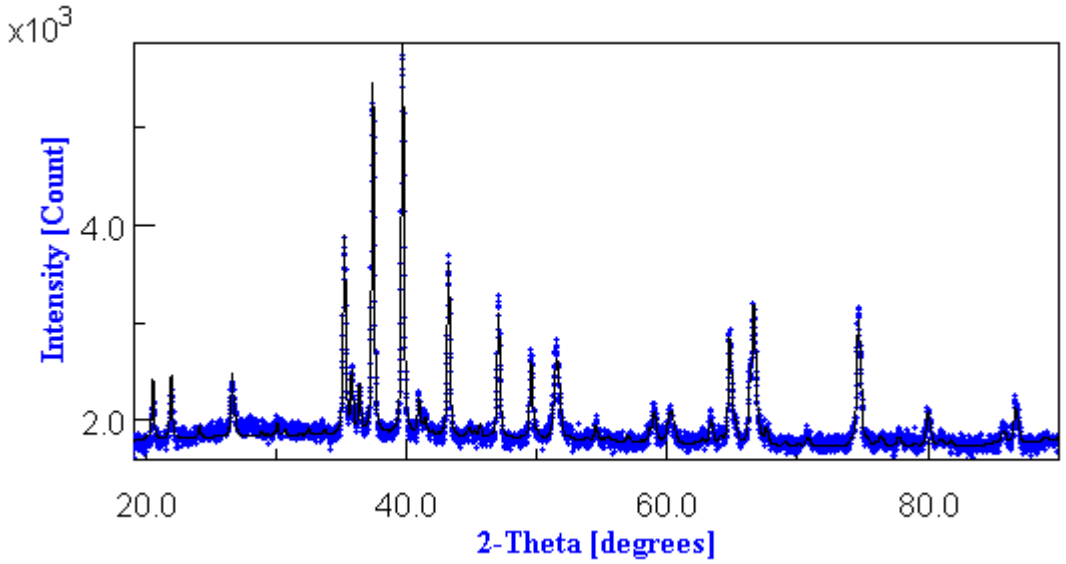

Figure 2.21: Ferrite and Feni powders ($N10U$) mixed by ultrasonic mixing.

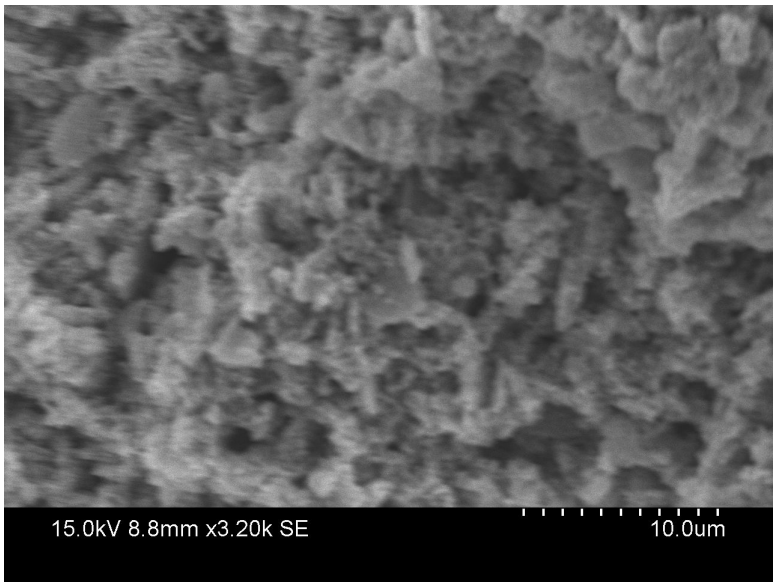

Figure 2.22: $N10U$ morphological view of the mixed powders, zoom view.

2.3.2 Magnetic characterization

The magnetic characterization of the samples is discussed in this section. First the samples mixed by milling are studies.

Here we present, $BaFe_{12}O_{19}$ nanopowder mixed without any milling with $Fe_{25}Ni_{75}$ nanopowder in 50% by volume, the resultant magnetization curve is shown in fig.2.23. The curve in blue is experimentally measured hysteresis for the mix of the precursors by VSM. The curve in red represents the average of the magnetization of the two precursors. We calculated the average using the eq.(2.2),

$$\sigma average = \sigma_{Ferrite} x + \sigma_{permalloy}(1 - x) \tag{2.2}$$

where, $\sigma_{Ferrite}$ represent the magnetization values measured experimentally for ferrite and $\sigma_{permalloy}$ is measures for the permalloy nanopowders alone. x is the corresponding mass fractions of ferrite used in the mixture. The red curve shows that the actual mix of the powder exhibit the magnetic behavior same as average of the two hysteresis of precursors.

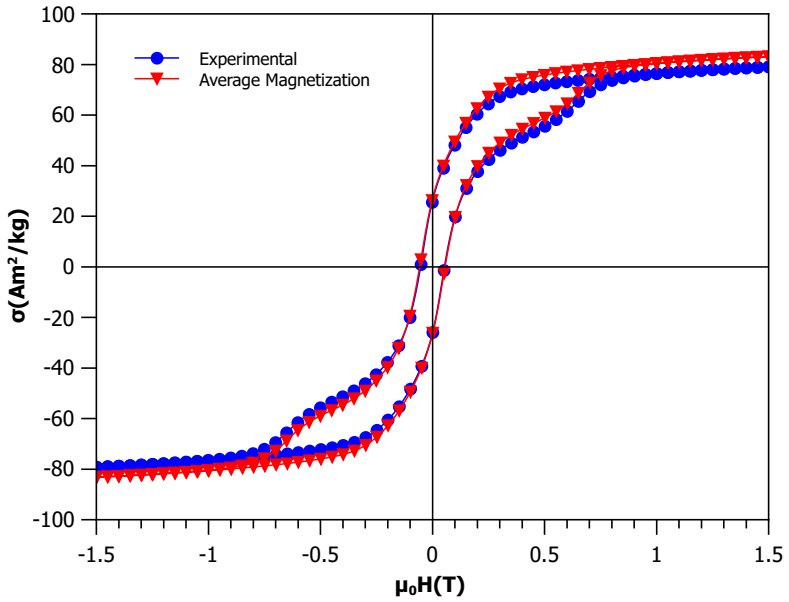

Figure 2.23: Magnetic properties of the mix of the nanopowder of *Barium ferrite* and *Iron-Nickel*. In blue, the experimentally measured curve and in red, the calculated magnetization.

2.4 Conclusion

1. Mechanical milled samples

   - Mixtures of Barium hexaferrite are mixed with different proportions of permalloy (2%, 5% and 10% by volume) by mechanical milling.
   - The mixed powders were milled for 20, 30 and 40 minutes at constant frequency of 400 *rpm*. The milling was carried out in ethanol medium with ball to powder ratio of 10 : 1.
   - The structural characterization was performed using X-ray diffraction. From the XRD analysis, all the mixtures were found to have presence of precursor phases and no other impurity phase was found. The crystallite size of the precursors remains the same.
   - The particle size of ferrites has remained same after the milling. Before milling the average size was 143 *nm* and after milling it was found to be 140 *nm*.

2. Ultrasonic mixed samples

   - The hard and soft magnetic phases were mixed using ultrasonic mixing for 10 minutes at 58% of the maximum power (i.e. 200 *watts*) with ethanol medium.
   - We analyzed the mixtures of permalloy mixed with barium ferrite. It was found that both the precursor phases were present in the sample in the same fractions as mixed.

3. We plot the magnetization curve for the experimentally measured mixture of 50% of permalloy mixture and the average theoretically calculated magnetization curve. Both the hystersis curve are found to be equivalent to each other.

CHAPTER 3
SYNTHESIS OF BULK MAGNETS

Chapter 3

Synthesis of Bulk Magnets

Contents

3.1	Spark Plasma Sintering	**48**
3.2	Mechanically milled bulk samples	**49**
3.2.1	Structural characterization	50
3.2.2	Magnetic characterization	57
3.3	Partial conclusion	**61**
3.4	Ultrasonic mixed samples	**62**
3.4.1	Permalloy	63
3.4.2	Iron	74
3.5	Partial conclusion for ultrasonic mixed samples	**76**

In this chapter, we discuss the synthesis of the bulk magnets from the mixtures obtained by hard milling and ultrasonic mixing as seen in section 2.3. In a typical synthesis process the next step after preparation of mixtures is pressing the powders to form the compact product followed by sintering. Instead of the conventional sintering process, we use Spark Plasma Sintering (SPS). A brief introduction to SPS process is given in section section 3.1 followed by structural and magnetic characterization of the bulk samples obtained by mechanical milling in the section section 3.2 and ultrasonic mixing in section section 3.4.

3.1 Spark Plasma Sintering

Spark plasma sintering (SPS) is a sintering technique utilizing uniaxial force and a pulsed (on-off) direct electrical current (DC) under low atmospheric pressure to perform high speed consolidation of the powder. This direct way of heating allows the application of high heating and cooling rates, enhancing densification over grain growth promoting short range diffusion mechanisms, and eventually maintaining the intrinsic properties of nanopowders in their fully dense products [62].

SPS is regarded as a rapid sintering method in which the heating power is dissipated exactly at the locations in the microscopic scale, where energy is required for the sintering process, namely at the contact points of the powder particles fig.3.1. This fact results in a favorable sintering behavior with less grain growth and suppressed powder decomposition.

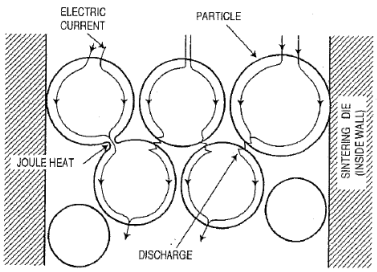

Figure 3.1: Current flow through particles during spark plasma sintereing.

SPS systems offer many advantages over conventional sintering methods (such as using hot press (HP) sintering, hot isostatic pressing (HIP) or atmospheric furnaces), including ease of operation and accurate control of sintering energy as well as high sintering speed, high reproducibility, safety and reliability. While similar in some aspects to HP, the SPS process is characterized by the application of the electric current through a power supply, leading to very rapid and efficient heating fig.3.2. The heating rate during the SPS process depends on the geometry of the container/sample ensemble, its thermal and electrical properties, and on the electric power supplier. Heating rates as high as $1000°C/min$ can be achieved. As a consequence, the processing time typically takes some minutes depending on the material, dimensions of the piece, configuration, and equipment capacity.

For the mixtures of barium hexaferrite and metallic alloys, sintering is done by using Sumitomo Dr.Sinter Spark Plasma Sintering machine. Sintering profile, parameters and conditions are mentioned with the samples in each section.

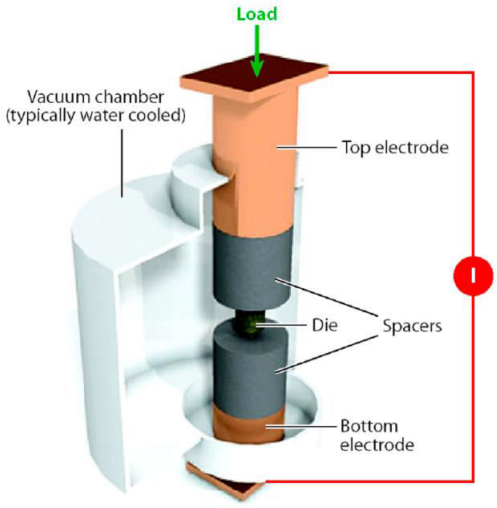

Figure 3.2: Inside view of SPS courtesy:J.E. Garay, Annu. Rev. Mater. Res. (2010)

3.2 Mechanically milled bulk samples

In this section structural and magnetic characterization of bulk samples obtained by spark plasma sintering of mechanically milled mixtures of barium hexaferrite and soft metallic phase $Fe_{25}Ni_{75}$ is discussed. The naming scheme of the samples is given in the table3.1. All the prepared samples consists of the same hard magnetic phase of barium hexaferrite, hence we did not mention it in the naming scheme. The first letter of the sample name indicates soft magnetic phase. The second, a number, indicating the volume fraction of the

soft phase mixed in the bulk. The third letter indicates the method of mixing, H stands for Hard milling followed by the temperature of sintering in degree centigrade. Further suffixes are added according the different conditions of mixing for eg. milling time etc.

Sample Name	Metal Prefix	Volume content X	Mixing method Y	sintering temperature T
NXYT	$Fe_{25}Ni_{75}$	2,5,10	H	800

Table 3.1: Naming scheme of the sintered bulk samples.

3.2.1 Structural characterization

Permalloy

We use the sol-gel prepared barium ferrite and nano-powder of $Fe_{25}Ni_{75}$ prepared by cryogenic melting as our starting materials. As we have seen in section 2.3.1, that the composition after milling were the same as the starting material. After which we perform sintering at 800° C for 10 minutes, as shown in the profile 3.3. Time of sintering is given on x-axis, y-axis on the left and on the right represents temperature and force applied respectively. We apply a maximum force of $2.6kN$ throughout the sintering process, shown in the figure by blue dotted line. The sintering is always performed in Argon atmosphere to avoid any possible reaction between air and the material. The heating and cooling rate is $156°C/min$. The milling time for each sample is indicated after the hyphen in the name, for eg.$N2H800-40min$ is to be read as sample consisting of $Fe_{25}Ni_{75}$, 2% in volume, mixed by *mechanical milling method* for $40min$. Sintering starts at $800°C$ which is maintained for $10min$ during the process.

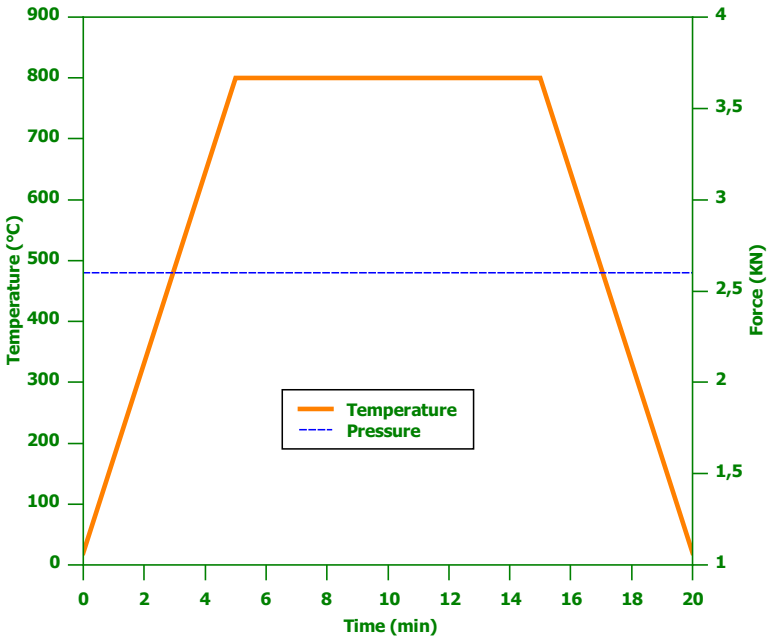

Figure 3.3: Sintering conditions under spark plasma sintering. The time of sintering process is labelled on x-axis. The y-axis on the left shows the temperature and the variation of temperature is shown in orange curve. The y-axis on the right shows the force in kN, represented by blue dotted line.

First we analyze the sample containing 2% of $FeNi$. The analysis of structural characterization of different samples has been carried out by Reitveld's profile fitting method

[63],[64].

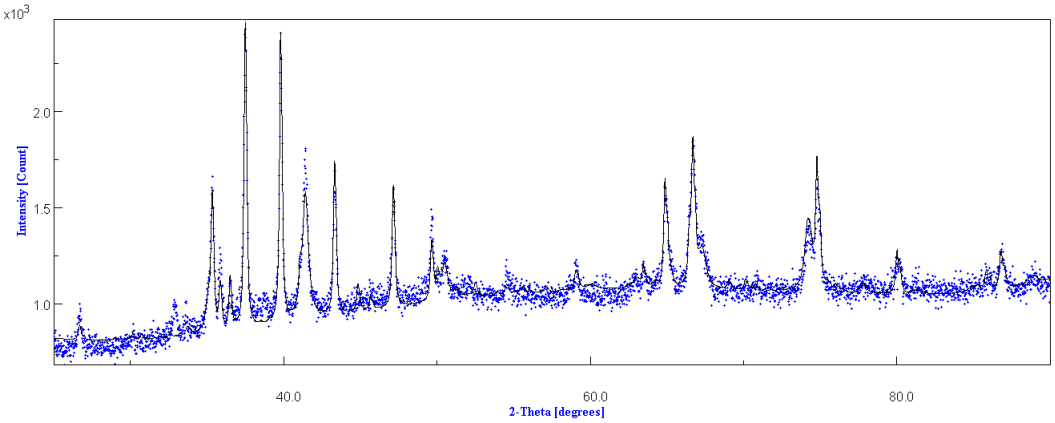

Figure 3.4: Diffarction pattern for $N2H800-40min$ sample from $2\theta = 20°to\ 90°$.

Diffraction pattern for bulk sample $N2H800-40min$ is shown in fig.fig. 3.4. The peaks seen in the diffraction pattern are broad and show that the bulk sample is crystalline in nature. From the analysis, it is found that barium ferrite phase (BaM phase) occupies 63.35% of the total volume, iron-nickel 0.65% and additional phase Fe_3O_4 (ferrous-ferric oxide or magnitite) is formed during sintering, which consists of 35.99% of the total volume. This impurity or the unwanted phase is found to exist only after sintering which could probably have been due to initiation of a reaction between the precursors during milling.

Surface image of the $N2H800-40min$ is taken using scanning electron microscope (SEM), shown in fig.3.5. The dark background represents BaM. On the surface we also find the formation of pores in the sample.

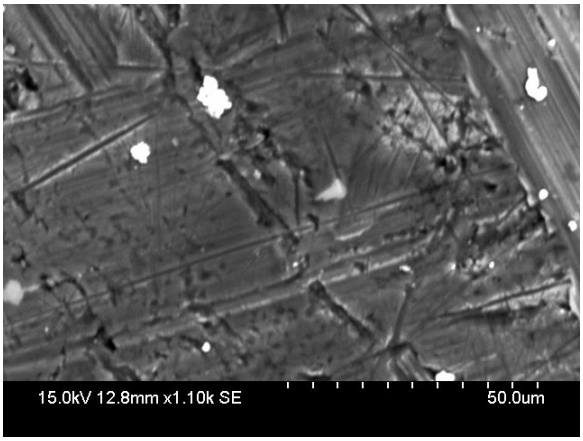

Figure 3.5: Microscope image of $N2H800$, resolved to the scale of 50 micrometer.

The bulk samples of $N2H800$ series, mechanically milled for progressively increasing time intervals of $10, 20, 30, 40, 50$ and 60 minutes, are found to vary in density. We measured the density of the bulk samples using Sartorius balance based on the Archimedes' principle method. The variation of density vs milling time is plotted in fig.3.6. $N2H800-40min$ bulk sample with the milling time of 40 minutes has the highest density as compared to the other samples in the series.

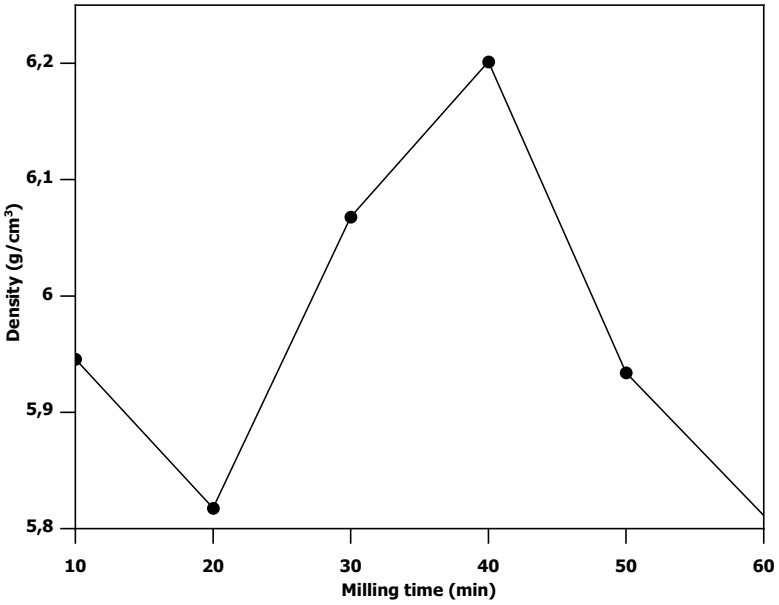

Figure 3.6: Density variation for $N2H800$ sample with milling time.

The series of samples with the composition of 5% $Fe_{25}Ni_{75}$ which have been mechanically milled for 25, 35 and 45 minutes are studied and comparative diffractograms are shown in fig.3.8 and fig.fig. 3.8. The X-ray diffraction pattern of the composite is studied after sintering. From the figures, we can observe that the peaks for $N5H800-45min$ are least in intensity and are broader in comparison to the other samples in this series. This indicates reduction in the cyrstalline size. The diffractogram of the samples also reveal presence of Fe_3O_4 (magnetite) and an intermediate phase $BaFe_2O_4$ (barium mono ferrite).

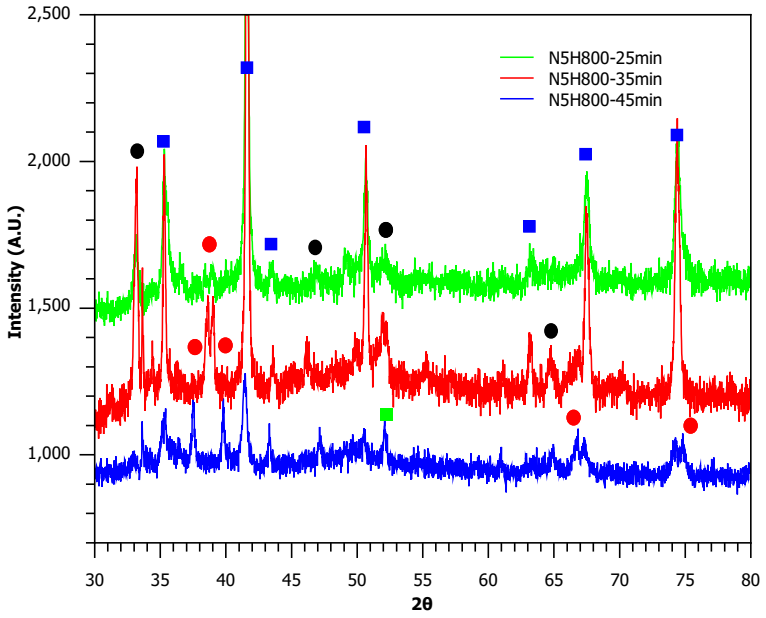

Figure 3.7: Variation in the diffraction pattern for $N5H800$ samples as a function of milling time. Different phases present in the sample are marked, the □ (in blue) represents Fe_3O_4 phase, □ in green-permalloy,○ (in red)-BaM phase and ○ (in black)-$BaFe_2O_4$ phase.

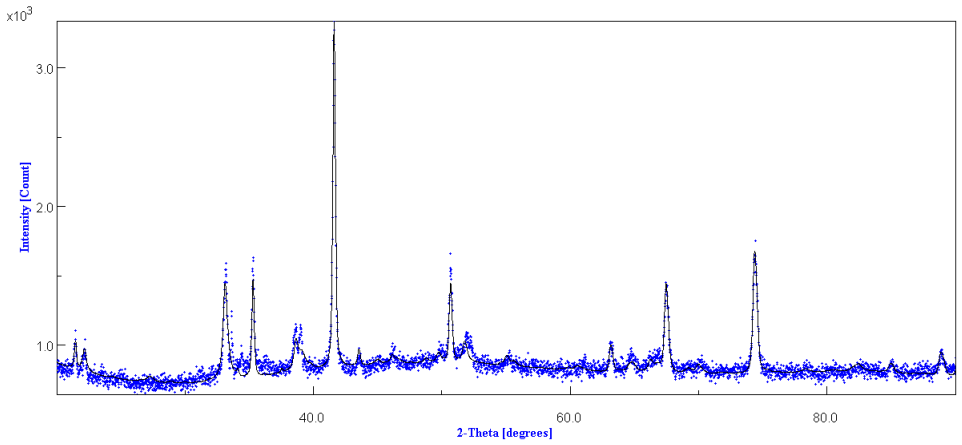

Figure 3.8: Diffraction pattern for $N5H800$.

As we can see in the profile, the indicative peaks of barium hexaferrite have vanished for the samples milled for 25 and 35 minutes. It is evident that the ferrite phase disintegrates and is transformed into intermediate phases. Table 3.2 summarizes the phases which grow in the series with the milling time.

Milling time	BaM		$BaFe_2O_4$		$FeNi$		Fe_3O_4	
(min)	Lattice parameter (nm)	$Vol\%$	Lattice parameter (nm)	$Vol\%$	Lattice parameter (nm)	$Vol\%$	Lattice parameter	$Vol\%$
25	$a = 0.59$ $c = 2.32$	6.5	$a = 1.899$ $b = 0.538$ $c = 0.843$	5.46	$a = 0.354$	1.47	$a = 0.838$	86.56
35	$a = 0.59$ $c = 2.32$	4.9	$a = 1.893$ $b = 0.538$ $c = 0.851$	15.19	$a = 0.354$	1.72	$a = 0.839$	78.14
45	$a = 0.59$ $c = 2.32$	41.6	$a = 1.893$ $b = 0.538$ $c = 0.843$	1.63	$a = 0.354$	2.2	$a = 0.84$	54.48

Table 3.2: Microstructure parameter of $N5H800$ series of samples revealed from Rietveld's refinement method

A possible reaction initiated during the milling and completed during sintering could lead to degradation of the ferrite phase. We propose the reaction given by eq.eq. (3.1), due to excess of Fe in the samples [65]. The source of excess iron possibly could be accounted from the oxidized $FeNi$ nano powder. The presence of carbon in the reaction is due to abundance of carbon during sintering, by use of graphite paper and carbon die for sintering.

$$2BaO \cdot 6(Fe_2O_3) + Fe \rightarrow 2BaFe_2O_4 + 7Fe_3O_4 + O_2 \tag{3.1}$$

The phase relation in ternary system $Ba - Fe - O$ reports three stable phases namely, $Ba_2Fe_2O_5$, $BaFe_2O_4$ and the hexagonal $BaFe_{12}O_{19}$ **??**. It is also reported that $BaFe_2O_4$ coexists with $BaFe_{12}O_{19}$ and Fe_2O_3 phase up to $1000°C$. Gracia et al.[66] reports that iron (III) oxide suffers a reduction to Fe^{2+} ion promoting the emission of molecular oxygen

when fired at high temperatures ($> 700°C$).

From the table3.2, we can also see that the BaM phase is present in relatively higher amount when the milling was performed for 45 minutes. The magnetic properties are affected by formation of the intermediate phases. H_c progressively diminishes as a consequence of the damage produced in the ferrite structure. This behavior is also observed in the works by Bercoff et al. and references therein [67].

The peaks for $N5H800$ series are broader than $N2H800$ diffraction pattern, which indicate the fine nature and small crystallite size of the particles.
The SEM image of the surface of $N5H800 - 35min$ is shown in the fig.3.9 in which the agglomeration of the iron-nickel particles can be seen on the surface of the bulk sample. The dark background represents the BaM matrix and the white represents the permalloy dispersion. In the bulk samples, pores can also be seen which could also be responsible for the shift in the peaks of the diffractogram.

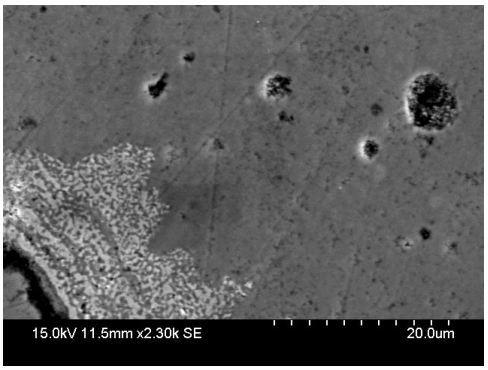

Figure 3.9: Microscope image of $N2H800$, resolved to the scale of 20 micrometer. Agglomeration of FeNi particles can be seen in the image.

For the next series of samples with 10% $FeNi$ mixed with barium hexaferrite, we carried out the X-ray diffraction after the sintering under the similar sintering condition as shown in the profile fig. 3.3.

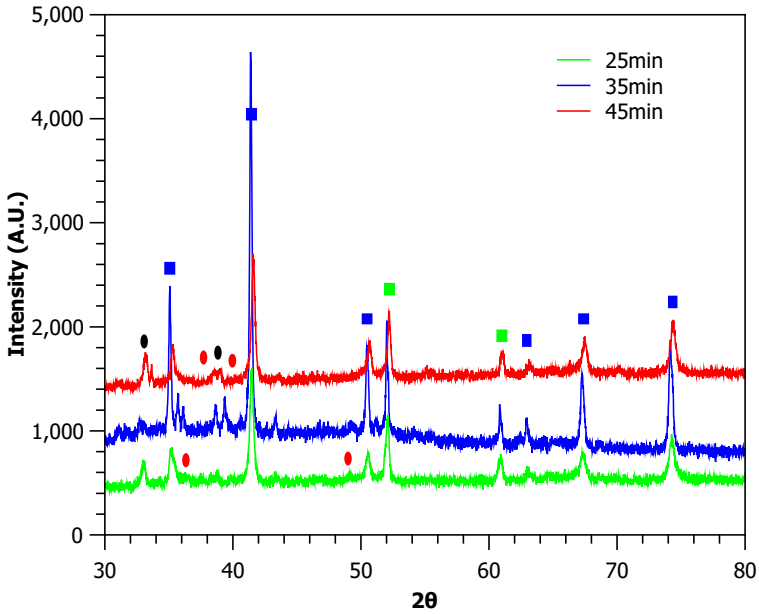

Figure 3.10: Variation in diffraction pattern in $N10H800$ samples depending on the milling time as indicated in the label. Different phases present in the sample are marked, the □ (in blue) represents Fe_3O_4 phase, □ in green-permalloy,○ (in red)-BaM phase and ○ (in black)-$BaFe_2O_4$ phase.

A summary of the micro-structural analysis is given in the table.3.3.

Milling time	BaM		$BaFe_2O_4$		$FeNi$		Fe_3O_4	
(min)	Lattice parameter (nm)	$Vol\%$	Lattice parameter (nm)	$Vol\%$	Lattice parameter (nm)	$Vol\%$	Lattice parameter	$Vol\%$
25	$a = 0.59$ $c = 2.32$	16.15	$a = 1.899$ $b = 0.538$ $c = 0.843$	5.9	$a = 0.353$	9.2	$a = 0.838$	68.7
35	$a = 0.59$ $c = 2.32$	5.9	$a = 1.893$ $b = 0.538$ $c = 0.851$	1.4	$a = 0.353$	10.0	$a = 0.839$	82.56
45	$a = 0.59$ $c = 2.32$	2.58	$a = 1.893$ $b = 0.538$ $c = 0.843$	6.1	$a = 0.354$	8.1	$a = 0.841$	83.27

Table 3.3: Microstructure parameter of $N10H800$ series of samples revealed from Rietveld's refinement method.

As seen from the X-ray diffraction pattern shown in the fig. 3.11 for the samples milled for 25, 35 and 45 minutes. It is observed that with the increasing milling time, the BaM phases diminishes and the volume fraction of the Fe_3O_4 (magnetite) phase increases. The $FeNi$ remains more of less similar to the original volume fraction $\sim 10\%$. A small amount of intermediate phase $BaFe_2O_4$ is also present in all the samples. The lattice parameter, as seen from the table remain the same. Since the metallic content has increased in the samples there is more reduction of the ferrite phase into Fe_3O_4.

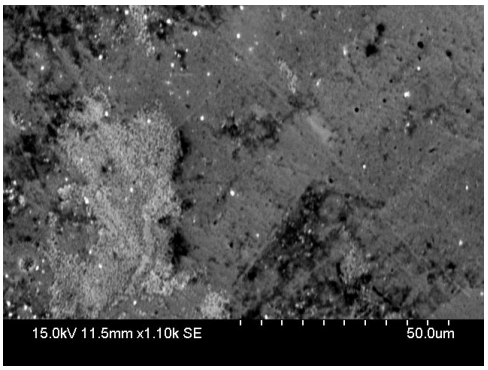

Figure 3.11: Microscope image of $N10H800 - 45min$, resolved to the scale of 50 micrometer. Distribution and agglomeration of permalloy particles can be seen in the image.

From the table.3.3 we can see the percent variation of each phase present in the bulk samples in response to the milling time. We can infer from the table that time of milling of powders has affected the formation of different phases in the bulk samples. The permalloy phase stays close to the its initial volume while mixing. BaM undergoes formation of an intermediate phase. Ones again we can conclude that the increasing milling time leads to reduction of the BaM phase and increases the fraction of magnetite phase in the bulk samples. Surface image of the bulk sample $N10H800 - 45min$ is shown in fig.3.11. The particles appear to be well dispersed. Agglomeration is found on the surface which is not visible in the current image shown. The bulk sample is seen to be more porous in nature than the $N5H800$ bulk sample.
Now we compare the above data based on the volume fraction of permalloy phase in the bulk samples. We take the bulk samples milled for 45 minutes. A comparative diffraction pattern is plotted in fig. 3.12. The curve in blue represents $N2H800-40min$ bulk sample, $N5H800 - 45min$ is indicated in red and $N10H800 - 45min$ is shown in green. Symbols are used to indicate different phases. The black squares indicates BaM phase and blue circles indicate the peaks corresponding to magnetite phase. We can observe that with the increase in the volume fraction of permalloy, the corresponding peaks of BaM phase disappear. For $N10H800$ sample, we can see only small intensity peaks of BaM shifted close to each other, almost superposed with each other. In all the bulk samples the volume of magnetite phase remains more or less constant. We also measured the variation in density and one finds that the samples with higher fractions of permalloy have higher density. The density of $N2H800-40min$ is measured to be 5848.5 kg/m^3 and for $N5H800-45min$ is 6038.8 kg/m^3.

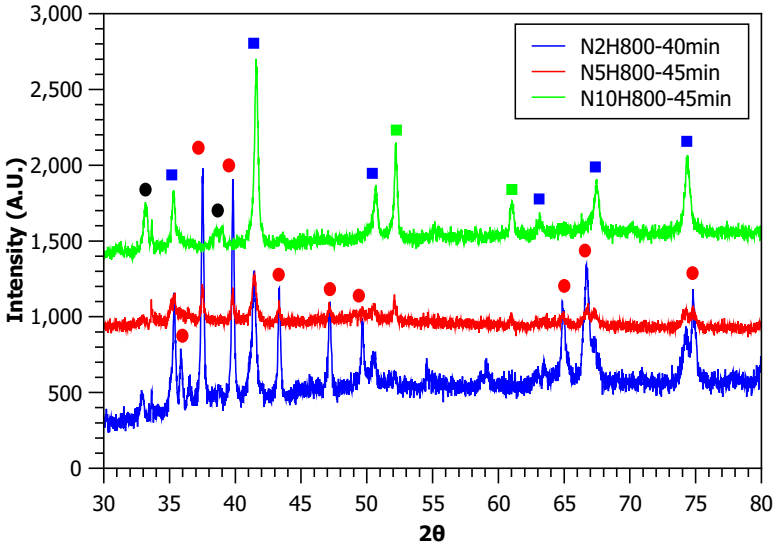

Figure 3.12: Comparative diffraction pattern for Iron nickel samples with different composition, ($NXH800$) series, as shown in the label. Various phases present in the samples are marked, the □ (in blue) represents Fe_3O_4 phase, □ in green-permalloy,○ (in red)-BaM phase and ○ (in black)-$BaFe_2O_4$ phase.

3.2.2 Magnetic characterization

Permalloy

We study the variation of magnetic properties of the bulk samples in response to the milling time for a constant volume fraction of permalloy in the bulk samples. Fig.3.13 plots the hysteresis loops for $N2H800$ bulk samples milled for $20, 30$ and 40 minutes.

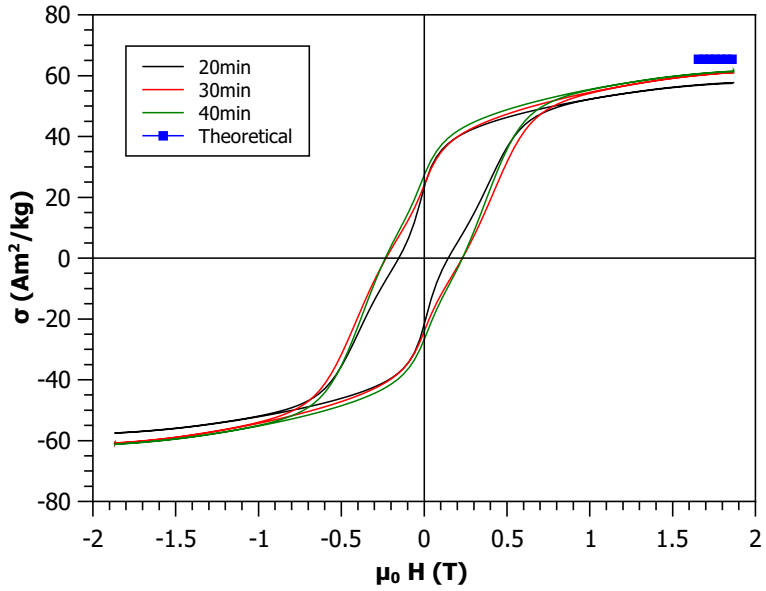

Figure 3.13: Hysteresis curve for $N2H800$ series with variable milling time as indicated in the label.

In the $N2H800$ bulk samples, the hysteresis loop show two phased behavior. We observe a slight variation in the value of coercivity and saturation magnetization. It is seen that the sample milled for 40 minutes has better saturation magnetization and better coercivity in comparison with the others. The small blue squares in the top right corner of the graph represents the theoretical value of saturation magnetization using eq.(**??**). The theoretical value of the coercivity is quite close to the experimental value.

$$\sigma_{average} = \sigma_{hard} * x + \sigma_{soft} * (1 - x) \tag{3.2}$$

where $\sigma_{hard/soft}$ is the specific saturation magnetization of hard and soft phases respectively and x is the mass fraction of the hard phase in the sample.

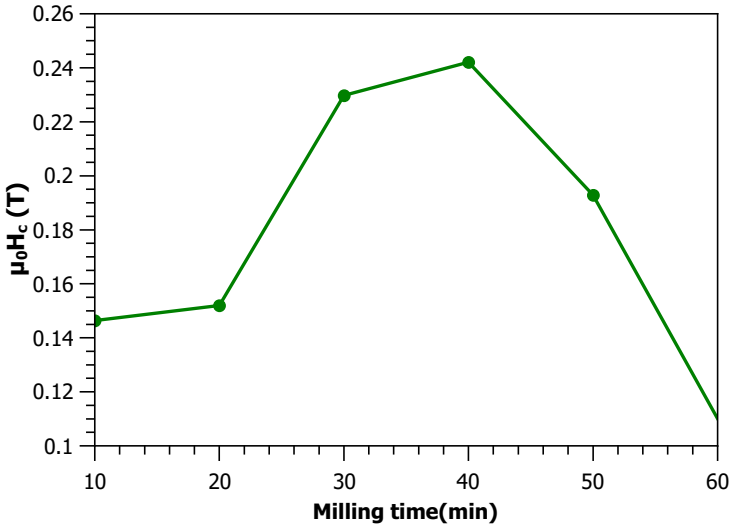

Figure 3.14: Variation of coercivity for $N2H800$ sample with milling time.

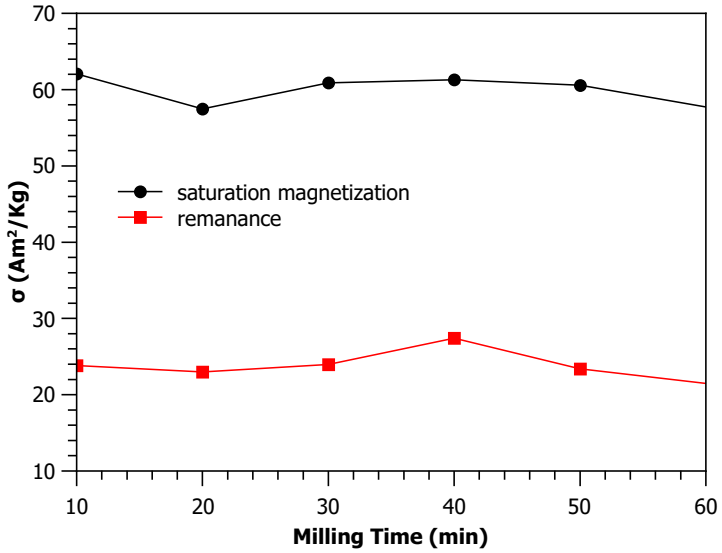

Figure 3.15: Variation in saturation magnetization and remanence for $N2H800$ series with milling time.

Variation in the coercivity for the $N2H800$ series of bulk sample as a function of milling time is plotted in the fig.3.14. The coercivity increases initially with the milling time and then starts to decrease. The bulk sample milled for 40 minutes shows the highest value of coercivity after which a decrease can be seen. Variation in saturation magnetization M_s and remanance M_r is plotted in fig.3.15, the red line indicates the change in remanance and black line represents the variation in M_r. Saturation magnetization and remanence are found to vary in the same pattern as coercivity.

Hysteresis plots for for $N5H800$ bulk samples milled for $25, 35$ and 45 minutes, are shown in the fig.3.16. As we have seen from the analysis of diffraction pattern, these samples contains a very high volume fraction of magnetite phase which being soft magnetic in behavior, is responsible for the reduction of coercivity in $N5H800$ bulk samples. Among the three curves shown in the figure for different milling time, the bulk sample milled for 45 minutes shows better magnetic characteristics compared to the rest.

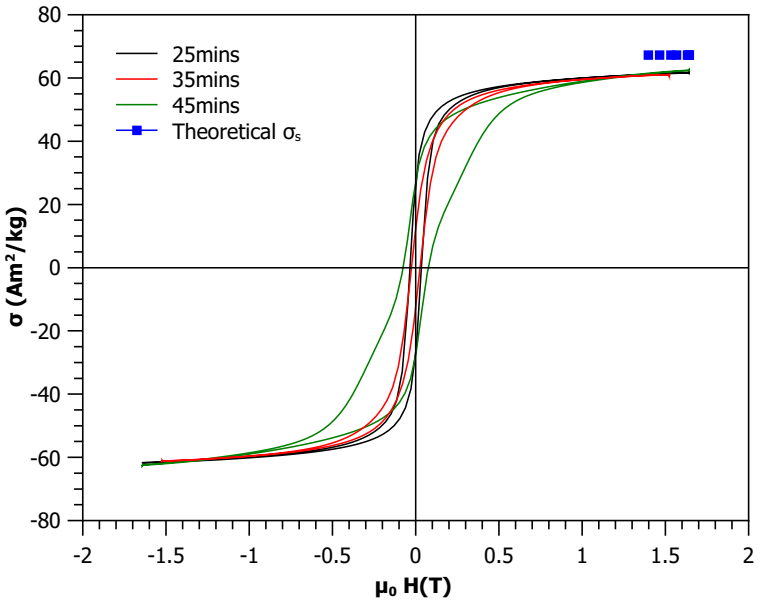

Figure 3.16: Hysteresis curve with variable milling time for $N5H800$ series as indicated in the label.

Hysteresis for 10% volume fraction of permalloy in Barium hexaferrite as shown in fig.3.17. The coercivity does not vary much with the milling time but the magnetization loops differ from one another. Sample with 45 minutes milling shows better magnetic characteristics in comparison to the other samples in the series. Again as seen in the XRD analysis in section 3.2.1, we find BaM disintegrates into intermediate phase and magnetite phase is also formed which leads to the soft magnetic behavior of the whole bulk sample.

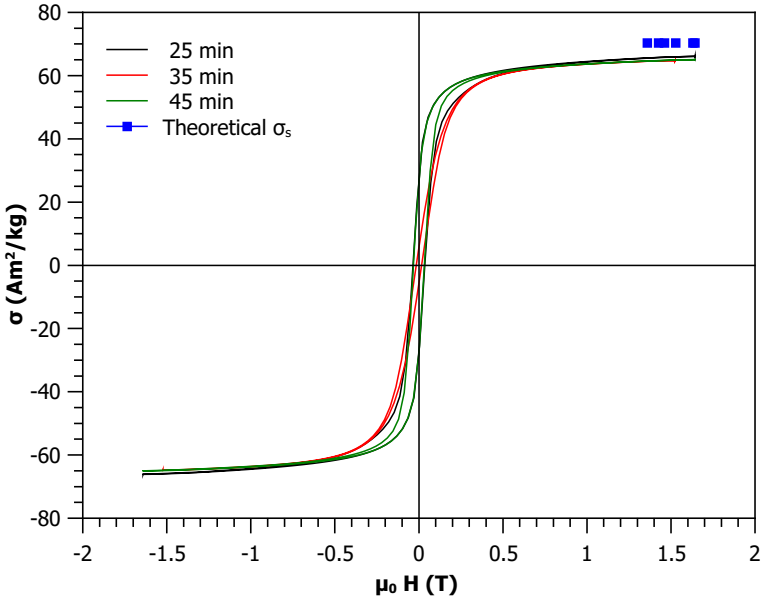

Figure 3.17: Hysteresis curve with variable milling time for $N10H800$ series as indicated in the label.

We draw a comparison among the bulk samples with different volume fraction of permalloy which are mechanically milled under the same conditions. The comparison of magnetic parameters between the samples with the variation in the volume fraction of metallic phase is shown in table.3.4. It can be seen that, with the increase in volume of permalloy in the bulk sample, the value of saturation magnetization increases due to increase in the soft magnetic phase. This also leads to decrease in the value of coercivity. We also find that the remanance of the bulk samples does not vary much.

Name	$\mu_0 H_c$ (T)	σ_s (Am^2/kg)	σ_r (Am^2/kg)	$\sigma_{s-theoretical}$ (Am^2/kg)	$\sigma_{s-th-reaction}$ (Am^2/kg)
N2H800-40m	0.243	27.32	63.449	65.43	64.94
N5H800-45m	0.076	27.175	62.44	67.3	65.08
N10H800-45m	0.031	26.29	65.089	70.32	67.06

Table 3.4: Influence of different percentage of iron-nickel in barium hexaferrite on the magnetic properties in $NXH800 - 45min$ samples.

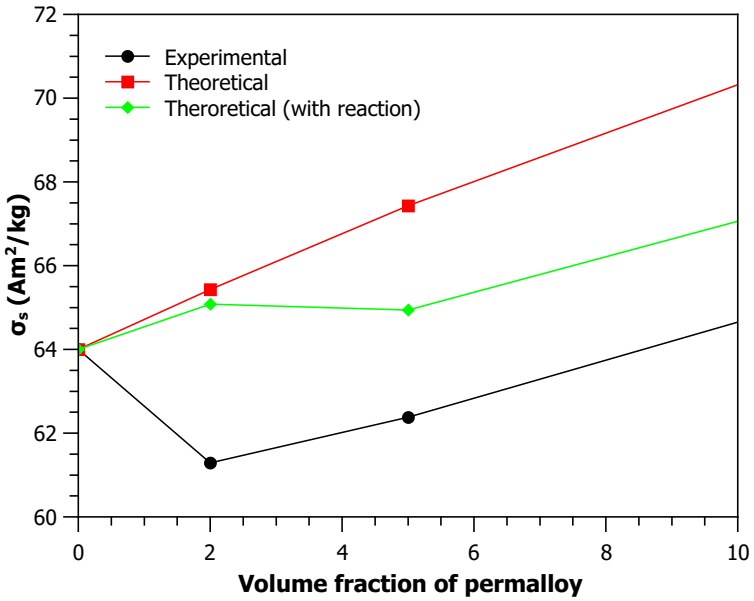

Figure 3.18: Comparison of saturation magnetization with theoretical magnetization with and without reaction between BaM and permalloy.

Fig.3.18 gives us the comparison of the experimental and theoretical saturation magnetization of the mechanically milled magnets as a function of variation in the volume fraction of permalloy. The curve in black (filled circles) is the variation of saturation magnetization measured experimentally. The curve in red(squares) represents the theoretical saturation magnetization which is obtained from the sum of calculated fraction of each phase times the saturation magnetization. This theoretical sum is obtained when we consider that the mixtures of BaM and permalloy do not have reaction between them. From the XRD analysis we find that the sintered samples have had reaction between BaM and permalloy phase. From the analysis of the diffractogram we also find the fraction of various phases formed during the sintering. Using the fraction of each phase present in the samples due to reaction, we calculated the theoretical value of the saturation magnetization as shown in green(diamonds).

From this we observe that the magnetization of the sintered samples is much lower than the theoretical value without the reaction and is a little lower than the theoretical saturation magnetization with reaction. Since we take the saturation magnetization of powder of the powdered form of each phase in the calculation of the theoretical values are a little higher.

3.3 Partial conclusion

- We synthesized the bulk compact composite magnets of barium hexaferrite and permalloy (with 2%, 5% and 10% volume fraction) by spark plasma sintering at $800°C$ for 10 min.
- From the structural analysis, the barium ferrite was found to disintegrate into intermediate phases $BaFe_2O_4$ and Fe_3O_4 with increasing milling time and increasing fraction of permalloy.
- Since the precursor phases were intact after milling and only appear after sintering, we proposed a reaction eq. (3.1), which probably was initiated during milling and completed after sintering.

- Magnetite phase occupies major volume in the bulk samples thereby affecting its magnetic properties. The hysteresis loop of the samples are soft magnetic.
- Amongst all the samples, the samples milled for 40 minutes showed relatively better magnetic properties. The hysteresis loop in all the samples show two phased behavior indicating a weak exchange coupling between hard and soft magnetic phases.
- The variation of coercivity and saturation magnetization is plotted in table 3.4. The magnetization slightly increases with increasing permalloy fraction.
- We also compared the measured saturation magnetization with theoretically calculated saturation magnetization for the precursor phase with out reaction and also by taking into account the phases appear after the reaction. The saturation magnetization calculated theoretically without considering any reaction between the phases is the limit of the saturation magnetization that the sample can achieve which is higher than the experimentally observed value.
- The theoretical saturation magnetization considering the reaction between the phases is found to be closer to the the experimentally observed value.
- All the bulk sample showed formation of pores as observed in the images obtained by SEM.

3.4 Ultrasonic mixed samples

In this section, we discuss the structural and magnetic characterization of the bulk samples mixed using ultrasonic mixer and sintered by SPS method. As seen in the section 3.2, the bulk samples obtained from the hard milling, did not show strong exchange coupling in the samples. Further the XRD analysis indicates possible chemical reaction that might have been initiated during mechanical milling leading to formation of unwanted phases in the bulk samples. Therefore, another method of mixing, *the ultrasonic mixing* is applied to keep the two magnetic phases from becoming chemically active.

In the section 2.3.1, we found from the analysis of the diffraction pattern of the ultrasonic mixed samples, that both the precursor phases are conserved after the mixing. In this section we study the bulk samples obtained form these mixtures after they were passed through the process of compaction and sintering using SPS method. Naming scheme for the samples is as mentioned previously, an overview about the bulk samples for this section is given in the table.3.5. All the bulk samples consists of the same hard magnetic phase i.e. (barium hexaferrite) BaM, hence we did not mention it in the naming scheme. The first letter of the sample name indicates soft magnetic precursor phase. The second, a number, indicates the volume fraction of the soft phase in the bulk. The third letter is represents the method of mixing, which in this case is U, stands for Ultrasonic mixing followed by the temperature of sintering in degree centigrade.

Sample Name	Metal Prefix	Volume content X	Mixing method Y	sintering temperature T
NXYT	$Fe_{25}Ni_{75}$	2,5,10	U	500, 550
FXYT	Fe	2,5,10,15,20	U	550

Table 3.5: Naming scheme of the sintered bulk samples using ultrasonic mixing.

The sintering is performed at $800°C$ for mechanically milled bulk samples has lead to the presence of unwanted phases which deteriorated the magnetic properties of the bulk samples. One of the possible reasons could be the high temperature of sintering, leading to higher diffusion of atoms. Hence a lower temperature is used for sintering. We chose to sinter at $500°C$ and $550°C$ since this temperature was enough to start sintering process.

3.4.1 Permalloy

XRD

Bulk sample $N2U550$, sintered at $550°C$ is structurally characterized using X-ray diffraction. Analyzed diffractogram of $N2H550$ is shown in fig.3.19. From the analysis we find that a large percent of the precursor phases are present in the bulk samples even after sintering. In the $N2U550$ sample, BaM phase occupies 93.97%, $Fe_{25}Ni_{75}$ = 0.8 (originally 2%) and a small additional cubic phase is formed whose stoichiometry is Fe_2O_3 (maghemite) which occupies 5.2% of the total volume. As oppose to the milled samples, here, the reaction leading to transformation of BaM phase into intermediate $BaFe_2O_4$ is not seen.

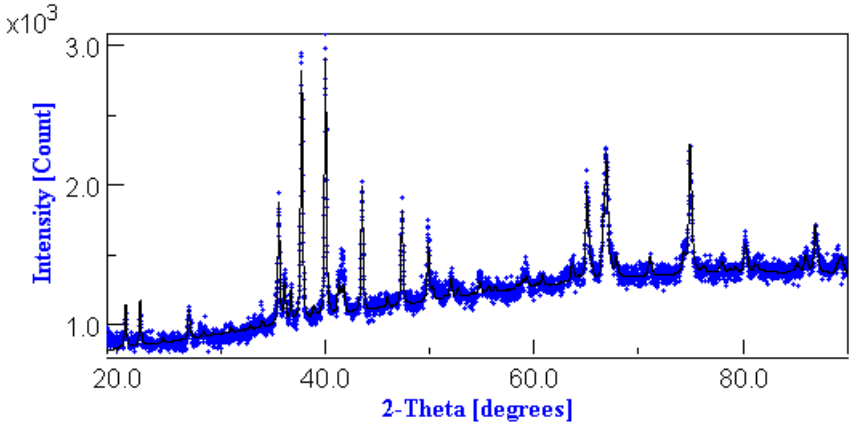

Figure 3.19: Analyzed diffraction pattern of ultrasonic mixed sintered bulk $N2U550$.

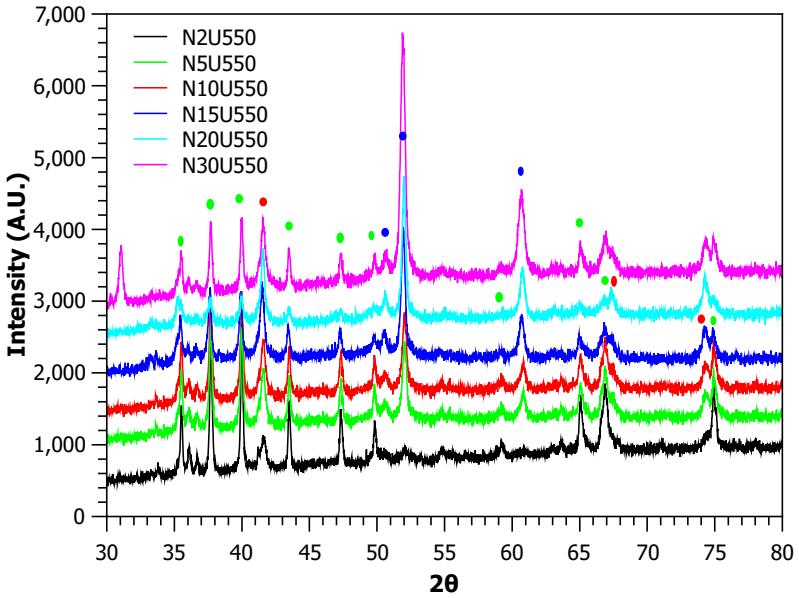

Figure 3.20: Analyzed diffraction pattern of ultrasonic mixed samples, $NXU550$ series, sintered $550°C$. The circles in green represent BaM phase; blue circles indicate peralloy phase and red show maghemite phase.

Fig.3.20 shows a comparative diffractograms for different volume fractions of permalloy

phase. All the samples are sintered at $550°C$ under similar conditions. Different phases are indicated by colored circles in the diffractogram. The red circles represents Fe_2O_3, maghemite phase and blue for permalloy phase. The filled circles in green indicate the presence of BaM phase. We find that BaM phase is present in all the bulk samples with the increasing volume of the metallic phase in contrast with the fact that it was absent or present in very less amount in many bulk samples obtained by hard milling.

Sample	BaM		$BaFe_2O_4$		$FeNi$		Fe_2O_3	
(min)	Lattice parameter (nm)	$Vol\%$	Lattice parameter (nm)	$Vol\%$	Lattice parameter (nm)	$Vol\%$	Lattice parameter	$Vol\%$
N2U550	$a = 0.589$ $c = 2.32$	75.5	-	-	$a = 0.354$	2.9	$a = 0.839$	21.5
N5U550	$a = 0.589$ $c = 2.32$	55.79	-	-	$a = 0.354$	4.23	$a = 0.839$	39.97
N10U550	$a = 0.589$ $c = 2.32$	54.8	-	-	$a = 0.354$	12.0	$a = 0.839$	33.11
N15U550	$a = 0.589$ $c = 2.32$	43.76	$a = 1.899$ $b = 0.538$ $c = 0.843$	1.5	$a = 0.354$	15.46	$a = 0.839$	39.26
N20U550	$a = 0.589$ $c = 2.33$	21.8	$a = 1.893$ $b = 0.538$ $c = 0.843$	1.7	$a = 0.354$	19.76	$a = 0.84$	56.66
N30U550	$a = 0.592$ $c = 2.32$	18.59	-	-	$a = 0.356$	32.8	$a = 0.839$	48.25

Table 3.6: Microstructure parameter of $NXU550$ series of samples revealed from Rietveld's refinement method.

In table.3.6 volume fraction of the different phases present in the bulk samples are deduced from the XRD analysis. The intermediate phase of Barium hexaferrite ($BaFe_2O_4$) is not present in the bulk samples till the volume fraction of permalloy is 10% but for volume fraction greater than this we observe traces of barium mono ferrite phase. Another phase maghemite, (Fe_2O_3) is present in all the samples. The volume of this phase increases with the increase in permalloy fraction in the samples. The BaM phase reduces with the increase in the permalloy volume in the sample. Similar observation have also been made by Ovtar et al. [68] and pal et al. [69]. With increasing fraction of permalloy phase, particularly $N10U550$, $N15U550$ and $N20U550$, the peaks in the diffraction pattern become more intense and broader which indicates reduction in crystallite size. Some peaks corresponding to BaM show splitting, this splitting is actually an overlap of the peaks corresponding to maghemite and BaM phase.

The second series of samples obtained after ultrasonic mixing is sintered at $500°C$. The diffractogram for $N5U500$ is shown in the fig.3.21. From the analysis, it is found that the cubic Fe_2O_3 phase occupies 17.8% of total volume. $Fe_{25}Ni_{75}$ occupies 4.6%, there is a presence of small amount of barium mono ferrite occupying 1.7% of the total volume and the rest of the volume is occupied by BaM phase. A comparative diffraction pattern for $NXU500$ series with different volume fraction of permalloy, $X = 5, 10, 15, 20$ and 30 is shown in fig.3.22.

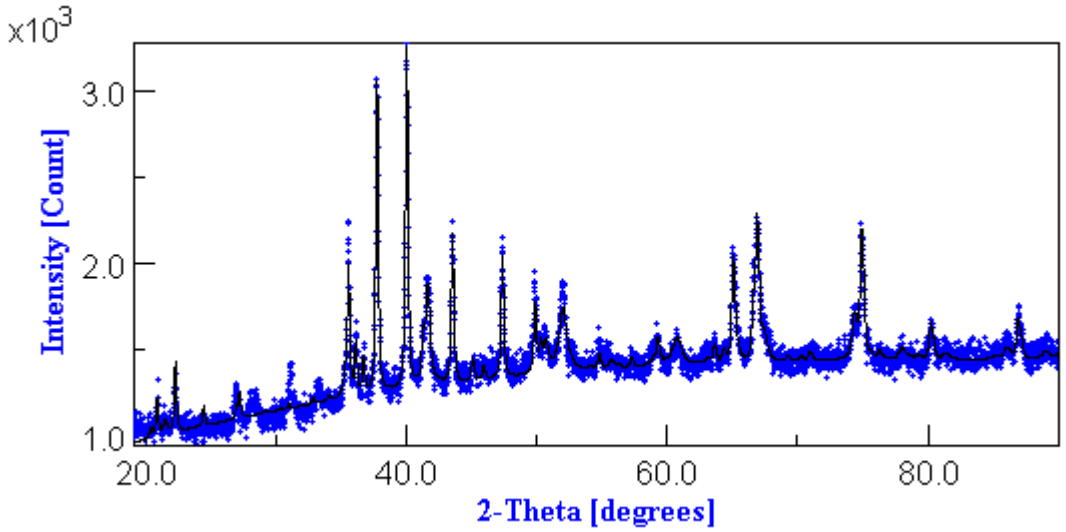

Figure 3.21: Analyzed diffraction pattern of ultrasonic mixed sintered bulk samples, $N5U500$, i.e. with 5% $Fe_{25}Ni_{75}$.

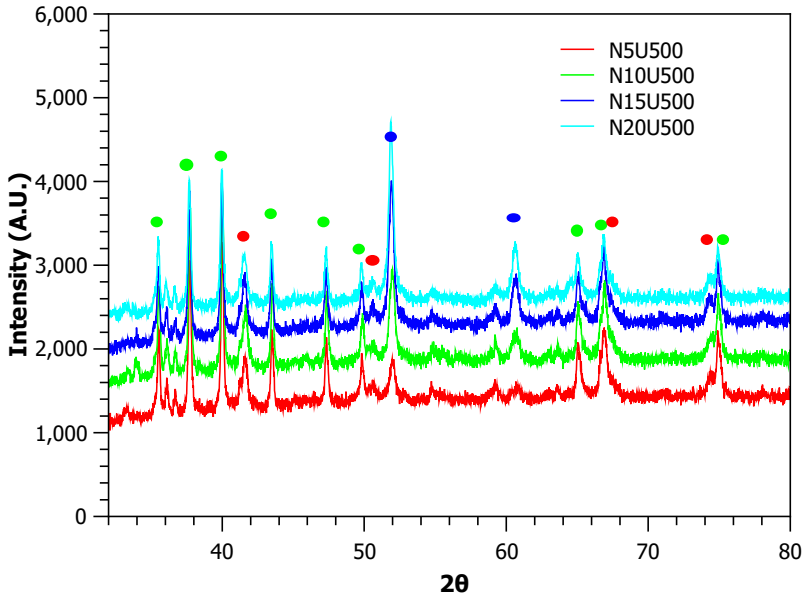

Figure 3.22: Analyzed diffraction pattern of ultrasonic mixed samples, $NXU500$ series, sintered at 500°. The green circles represent BaM phase, Fe_2O_3 is shown in red and $FeNi$ phase is shown in blue circles.

In the fig.3.22, diffraction patterns for the varying volume fraction of the permalloy phase are compared. One can observe the variations in the phase depending on the peak height and width. Different phases are indicated by colored dots. The green dot indicates BaM phase, blue indicates permalloy phase and Fe_2O_3 or maghemite is represented by red dot. Magnetite phase is formed in all the bulk samples but is occupies only about 20 25% of the total volume.

Sample	BaM		$BaFe_2O_4$		$FeNi$		Fe_2O_3	
(min)	Lattice parameter (nm)	$Vol\%$	Lattice parameter (nm)	$Vol\%$	Lattice parameter (nm)	$Vol\%$	Lattice parameter	$Vol\%$
N5U500	$a = 0.589$ $c = 2.32$	75.74	$a = 1.92$ $b = 0.546$ $c = 0.835$	1.7	$a = 0.354$	4.6	$a = 0.839$	17.8
N10U500	$a = 0.589$ $c = 2.32$	62.8	$a = 1.92$ $b = 0.538$ $c = 0.843$	0.83	$a = 0.355$	12.8	$a = 0.839$	23.48
N15U500	$a = 0.589$ $c = 2.32$	58.24	-	-	$a = 0.355$	17.38	$a = 0.839$	24.36
N20U500	$a = 0.589$ $c = 2.32$	52.92	-	-	$a = 0.355$	21.5	$a = 0.84$	25.54

Table 3.7: Microstructure parameter of $NXU500$ series of samples revealed from Rietveld's refinement method.

Table.3.7 gives the volume fraction of different phases present in the bulk samples sintered at $500°C$. We can see that the samples containing 5% and 10% volume fraction of permalloy, have traces of barium mono ferrite present after sintering. This is contrary to the observation for the samples sintered at $500°C$, in which this phase for present for higher volume fraction of permalloy. The fraction of permalloy remains more or less similar to the initial fraction after mixing. Thus we find a small reduction of BaM phase as compared to the samples obtained by mechanical milling.

Magnetic properties

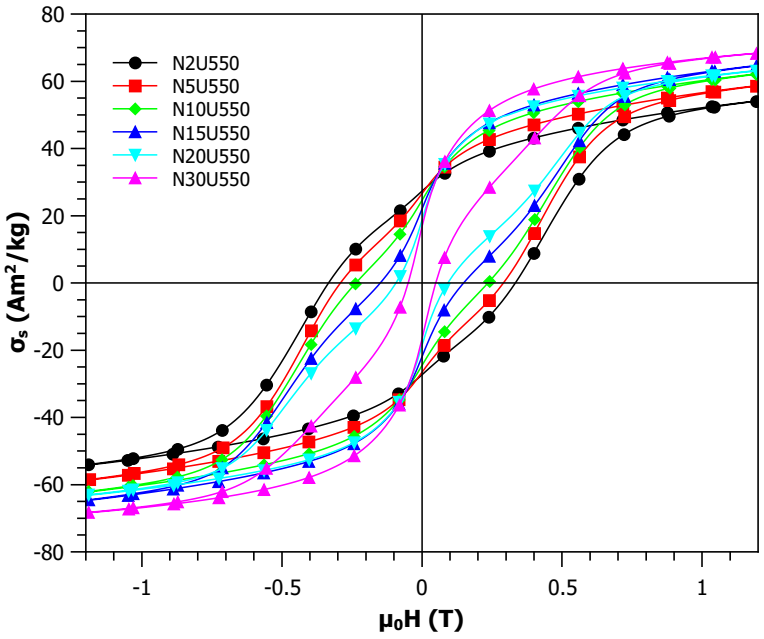

Figure 3.23: Hysteresis loop for different volume fraction X of $Fe_{25}Ni_{75}$ in the $NXU550$ series, where $X = 2, 5, 10, 15, 20$.

We study the magnetic properties of permalloy mixed bulk samples in this section. First we discuss $Fe_{25}Ni_{75}$ bulk samples sintered at $550°C$. The fig.3.23 show a comparative behavior and variation in hysteresis for a different volume fractions of the permalloy phase. Coercivity and saturation magnetization are found vary inversely with each other. The coercivity decreases with the increase in the permalloy fraction. As already seen from the XRD analysis, sec.3.4.1 the magnetite phase occupies between $30 - 40\%$ and is dominant in the bulk samples which is responsible for a dominant soft magnetic behavior in the bulk samples.

We observe from the figure, the loop in black corresponding to $N2U550$ has highest coercivity in comparison to the other bulk samples but has lowest saturation magnetization. With the increasing permalloy content, there is a reduction in coercivity and increase in saturation magnetization. The loops still have 2 phased behavior.

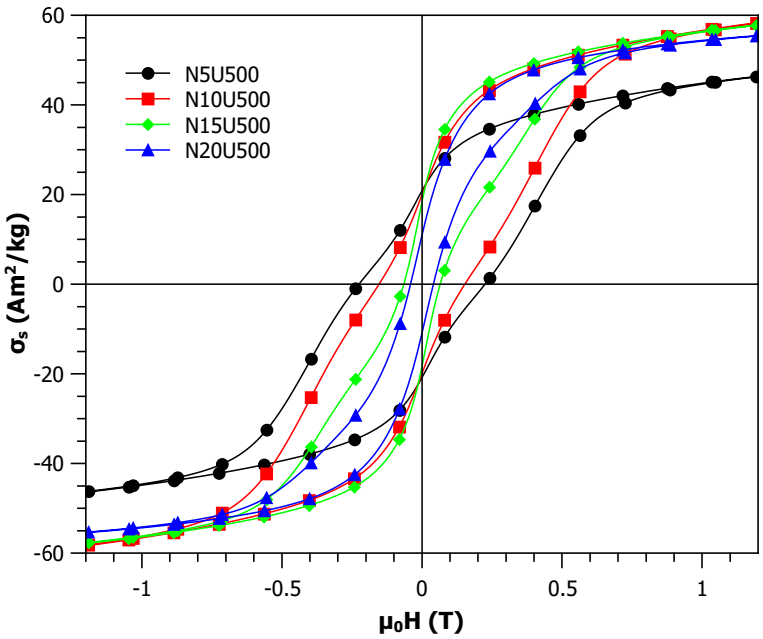

Figure 3.24: Hysteresis loop for different volume percentage of $Fe_{25}Ni_{75}$ in $NXU500$ series.

For the bulk samples sintered at $500°C$, we find a different magnetic behavior. The hysteresis loop are shown in fig.3.24 for different volume fractions $X = 5, 10, 15$ and 20 percent of permalloy respectively. We find again the decrease in coercivity and increase in saturation magnetization with the increase in the permalloy content again. The loops are 2 phased loop and do know show an exchange spring behavior.

We compare the magnetization parameters of the samples sintered at two different temperatures. Fig.3.25 and fig.3.26 show the variation in the coercivity and saturation magnetization respectively. From the figures, we observe that coercivity H_c reduces with the increase in the volume fraction of permalloy. With respect to the sintering temperature, H_c is found to be higher for the samples sintered at $550°C$ than those sintered at $500°C$. The green line shows the theoretically calculated saturation magnetization for each composition to compare with experimentally obtained values.

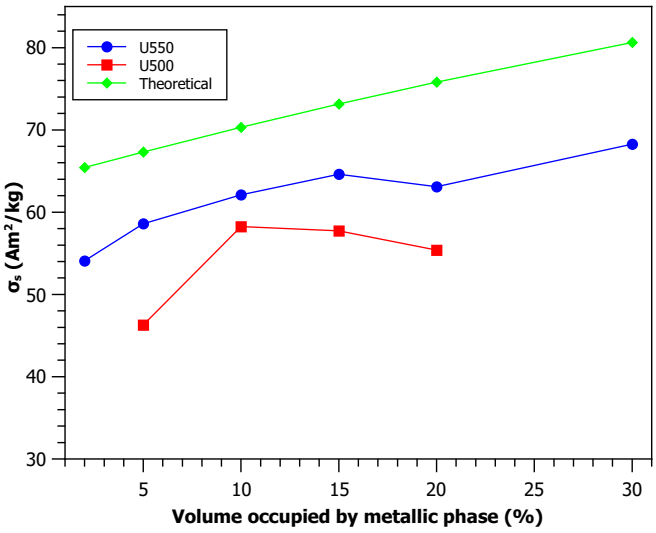

Figure 3.25: Saturation magnetisation variation in $NXU500$ and $NXU550$ sample series, with respect to different volume fractions of permalloy, sintered at $500°C$ (in red) and $550°C$ (in blue). The values are compared with the theoretical saturation magnetization (in green) for each composition.

Similarly the saturation magnetization increase with the increasing volume till the volume of metallic phase is 15%, on further increasing the volume fraction of permalloy M_s also reduces. So overall, the bulk samples sintered at $550°C$ is found to have higher magnetic properties although it is reduced due to soft magnetic characteristics.

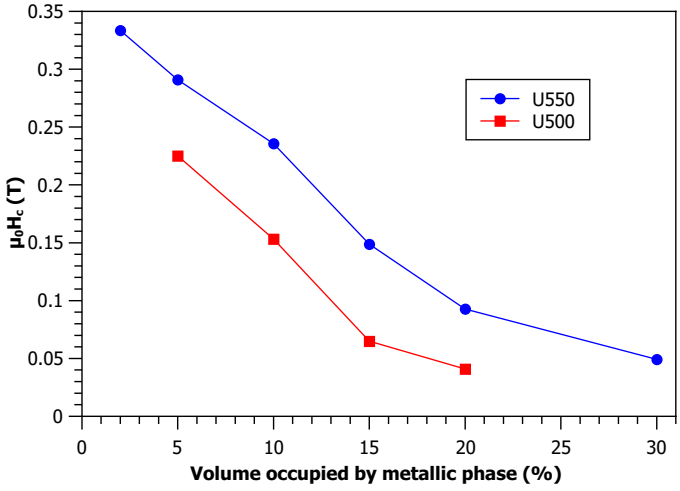

Figure 3.26: Coercivity variation in $NXU500$ and $NXU550$ sample series, with respect to different volume fractions of permalloy, samples sintered at $500°C$ (in red) and $550°C$ (in blue).

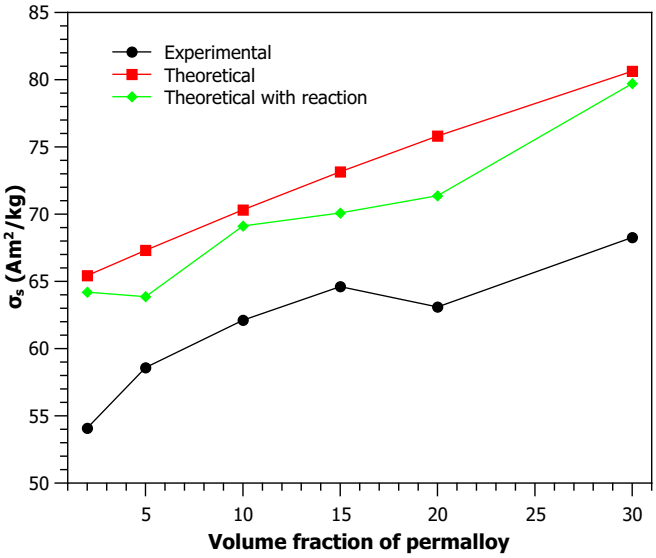

Figure 3.27: Saturation magnetization variation in $NXU550$ sample series, with respect to different volume fractions of permalloy. They are compared with the theoretical values obtained when the phases are mixed with out reaction and the theoretical values including the reaction of the phases present after sintering.

Fig.3.27 shows the comparison of experimentally measured saturation magnetization (black circles) of $NXU550$ series of samples with the theoretical values of saturation magnetization, without reaction between the precursor phases (red squares) and with reaction between the precursor phases (green diamonds). Saturation magnetization as a function of increasing volume fraction permalloy content in the sample. The theoretical curve (in red) shows that the in the case of no reaction between the precursor phases, the saturation magnetization increases linearly with the increasing fraction of permalloy phase. The experimentally measured magnetization is much lower than the theoretical values. However, we also find that the the experimental saturation magnetisation also increases with the increasing permalloy fraction but is lower than theoretical curve. We also plot the theoretical saturation magnetization by considering all the phases present after the sintering due to reaction between the precursors, curve shown by green diamonds. We find that this curve is closer to the theoretical values without the reaction between the phases. This is probably because we use the values of magnetization of powdered form of each phase which is always higher than the magnetization after heating. Also it depends largely on the particle size [70], [71].

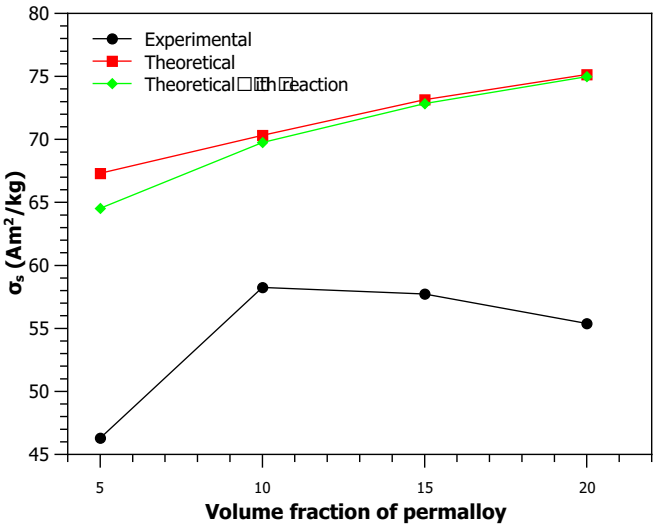

Figure 3.28: Saturation magnetization variation in $NXU500$ sample series, with respect to different volume fractions of permalloy. They are compared with the theoretical values obtained when the phases are mixed with out reaction and the theoretical values including the reaction of the phases present after sintering.

For the samples sintered at $500°C$, the comparison of saturation magnetization with the theoretical values is shown in fig.3.28. We find that the theoretical values with and without reaction are very close to each other and greater than experimentally observed values.

Temperature variation

Here we study the effect of measuring temperature on the magnetic properties of the sample. The bulk samples of $NXU500$ and $NXU550$ are measured at low temperatures at $140K$ and $200K$ using the temperature measurement facility in VSM. Hysteresis loops measured are presented below for 2 compositions to compare the change in the magnetic properties and the shape of hysteresis with respect to temperature.

Fig.3.29 shows the hysteresis loops for $N10H500$ samples measured at different temperatures. From the figure it can be seen that the coercivity does not vary much at the measuring temperatures. Magnetization in the loops is normalized to focus on the change in the shape of the loops. The loops still have the 2 phase behavior but there is slight change in the shape as the temperature is lowered.

Fig.3.30 shows hysteresis loops traced for bulk sample with 20% permalloy fraction in the bulk measured at different temperature. This sample has soft magnetic behavior among all the other bulk samples sintered at $500°C$. We can observe in the figure that there is a very little change in the shape of the hysteresis loop with the temperature but the hysteresis loops still show 2 phased behavior.

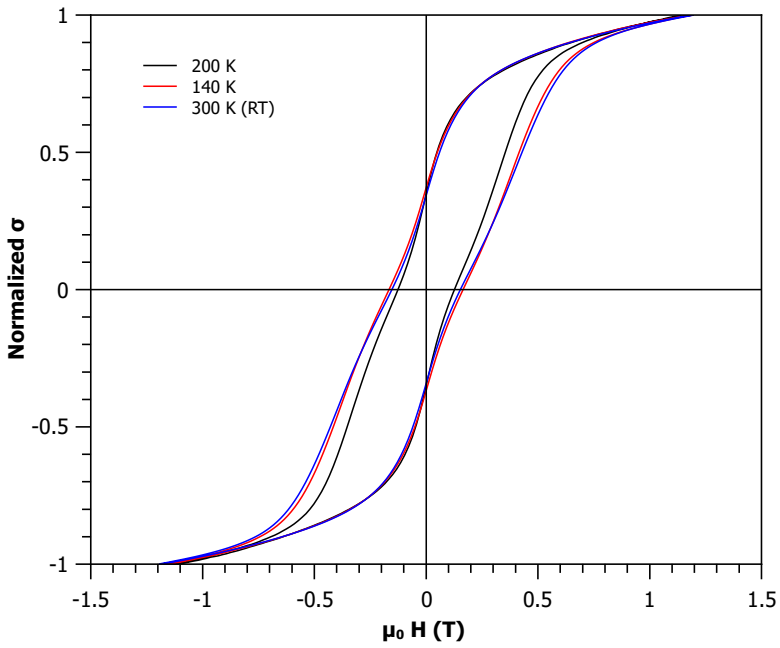

Figure 3.29: Variation in hysteresis is shown with temperature for $N10U500$ sample.

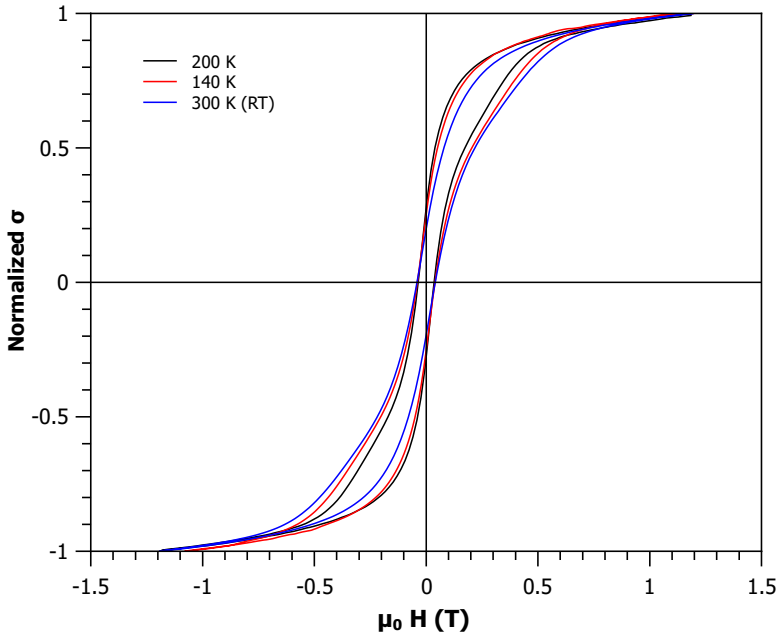

Figure 3.30: Variation of hysteresis with temperature for $N20U500$ sample.

The variation can be more clearly understood by extracting the variation in coercivity from the above loops. Variation of coercivity versus volume fraction of permalloy in the bulk is plotted in the fig.3.31 measured at different temperature. From the figure we find that the coercivity become higher for the same composition with the decrease in temperature.

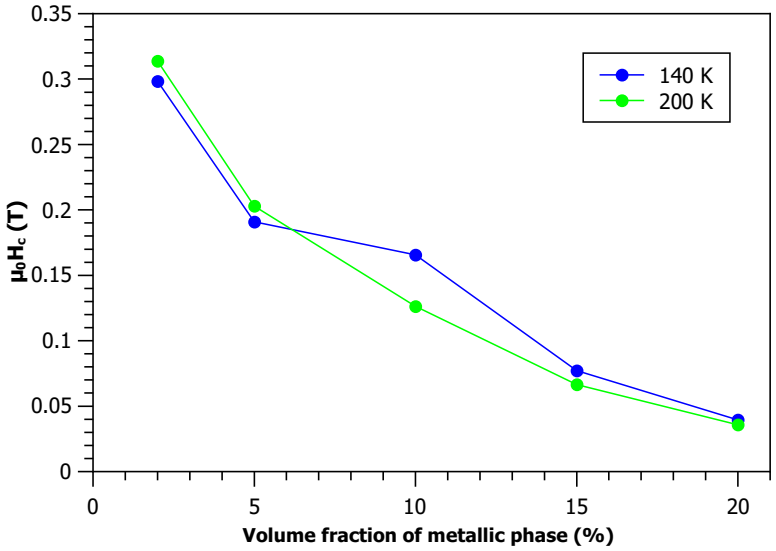

Figure 3.31: Coercivity variation for $NXU500$ series where X is the volume fraction plotted on x-axis, the measuring temperatures are labelled in the figure.

Bulk samples of iron-nickel sintered at $550°C$ are also measured with respect to the variation in temperature. The hysteresis loop is plotted for bulk samples of $N10U550$ and $N20U550$ bulk samples. Fig.3.32, shows the loops for $N10U550$ at temperatures below the room temperature. In the figure, we see change in the shape of hysteresis with decrease in temperature of measurement.

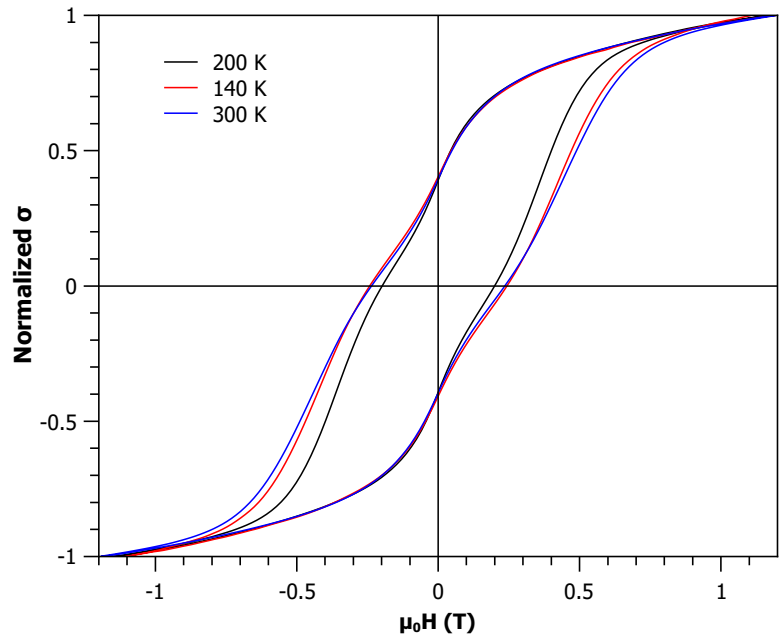

Figure 3.32: Hysteresis measurement for $N10U550$ at different temperature.

Fig.3.33 shows the hysteresis for $N20U550$ bulk sample measured at different temperatures. With higher fraction of permalloy phase, as seen from the XRD analysis, there is an intermediate phase of $BaFe_2O_4$, along with others, present in this bulk sample that occupies more than half of the volume in the bulk. This leads to reduction in the coercivity of the sample. We find from the figure that coercivity does not vary much with

temperature.

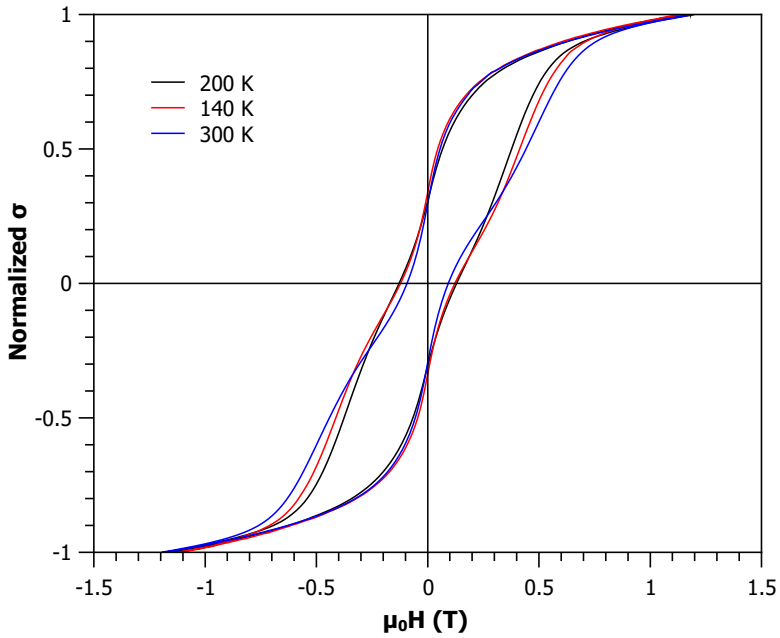

Figure 3.33: Hysteresis measurement for $N20U550$ at different temperature.

We plot the variation in coercivity as a function of the volume fraction of the permalloy in the bulk at different temperature. Fig.3.34 shows the variation in coercivity for $NXU550$ series, X being the volume fraction of the metallic phase, plotted on the x-axis of the figure.

In fig.3.34 we find a steep decrease of coercivity with increasing fraction of permalloy and a slight increase with the decrease in the temperature.

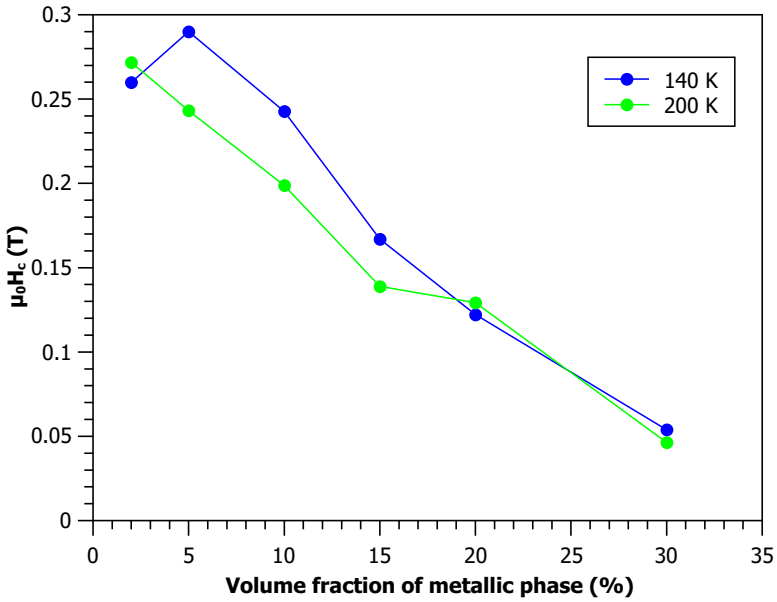

Figure 3.34: Coercivity vs volume fraction of the metallic phase ($Fe_{25}Ni_{75}$), $NXU550$, is plotted in the figure. The values are measured at different temperature indicated in the label. The samples are sintered at $550°C$.

The ultrasonic mixed nanopowders were sintered at various lower temperatures in order to find right temperature of sintering. A reference sample is chosen randomly for comparison, which in this case is $N10U$. It is sintered at various temperatures with a constant pressure at $100MPa$ under Argon atmosphere. The hystersis measurements at room temperature are shown in fig.3.35.

The measured loops show 2 phased behavior. We find a slight change in coercivity and shape of the loop. We chose the sintering temperature according to the good properties needed for a permanent magnet applications i.e. magnets with better coercivity and remanence. From the data we find that the hysteresis for the bulk samples sintered at $500°C$ shows promising single phase behavior. Hence $500°C$ was taken as the lower limit of sintering temperature in the previous measurements.

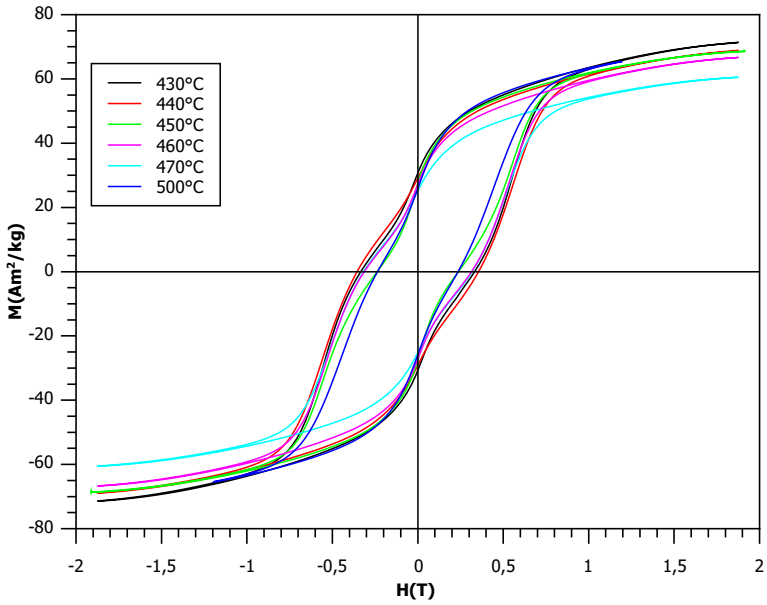

Figure 3.35: Hysteresis loop for $N10U$ samples at different sintering temperature.

3.4.2 Iron

XRD

Bulk samples of nanopowder of (Iron) Fe mixed with BaM are discussed here. The bulk samples are prepared for different volume fraction of Fe in the samples and were sintered at $550°C$. Diffraction patterns for samples containing the volume fraction, X, of Fe ($FXU550$ series, $X = 2, 5, 10, 15$ and 20) are shown in the fig.3.36. From the analysis, it is found that the iron undergoes formation of magnetite, i.e. Fe_3O_4, in this sample it occupies 49.5% of the total volume. BaM phase is also present with 46.19% volume fraction and barium mono ferrite and $BaCO_3$ occupies 2.46% and 1.83% of the volume respectively.

From the figure, we find that the two prominent peaks of BaM disappear in the bulk samples with $X \geq 5$. Orthorhombic $BaFe_2O_4$ phase appears in a small fractions. The green circle represents the BaM phase,circles in blue show magnetite phase and the red circle indicate the barium mono ferrite phase.

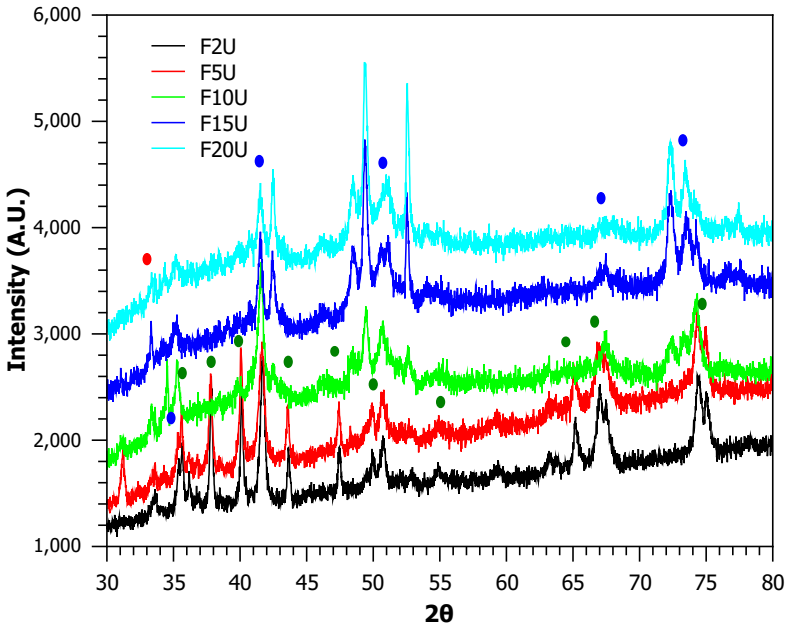

Figure 3.36: Diffraction pattern of ultrasonic mixed $FXU550$ series sintered $550°C$, where X is volume fraction .

Magnetite phase is always present in all the samples. For samples having higher volume fraction of the metallic phase, some peaks broadens but do not change in intensity. Shifting in the position of the peaks is also observed. In samples F15U and F20U only few peaks corresponding to magnetite phase are identified and peaks corresponding to BaM phase are absent.

Magnetic characteristics

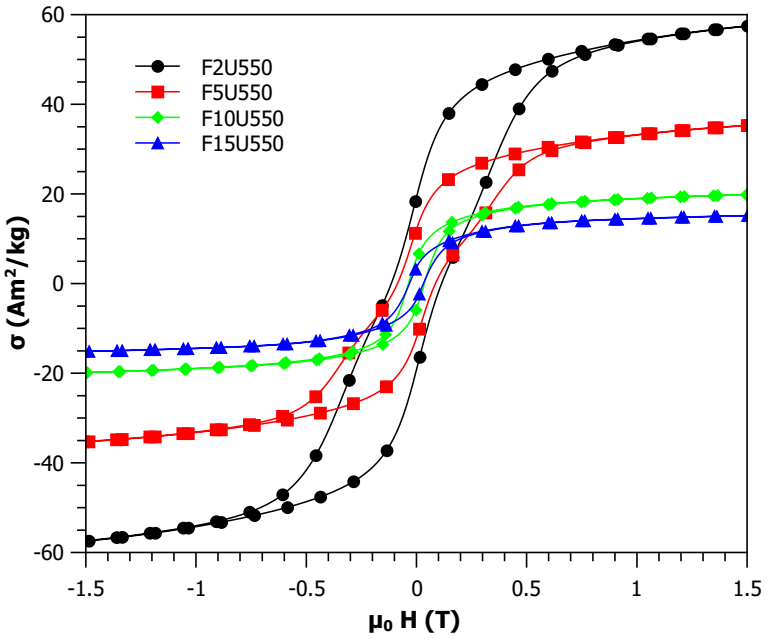

Figure 3.37: Hysteresis loop for $FXU550$ series with different volume fraction of Fe, $X = 2, 5, 10, 15$.

Magnetic characterization of the $BaFe_{12}O_{19}$-$(Fe)_x$, where x is the volume fraction of Fe in the bulk samples is measured by VSM. The measurements are done at room temperature. Fig.3.37 plots the hysteresis loops with respect to the different volume fraction of Fe, all of which are sintered at $550°C$.

We find the hysteresis for 2% fraction of Iron has the highest M_s. As the iron content increases in the bulk the hysteresis loop becomes smaller as compared to the $F2U550$ loop. The magnetic properties deteriorate with the increasing fraction of Iron, owing to the fact that we found the formation of iron oxide with stoichiometry FeO and complete disappearance of BaM phase and also an intermediate phase $BaFeO_2$ in the bulk. Magnetite phase is present in all the samples.

Variation in magnetic parameters is plotted in fig.3.38. Variation in coercivity, given in black, corresponds to the left Y axis. Variation in M_s is given in red squares corresponds to the values on the right y-axis (in red).

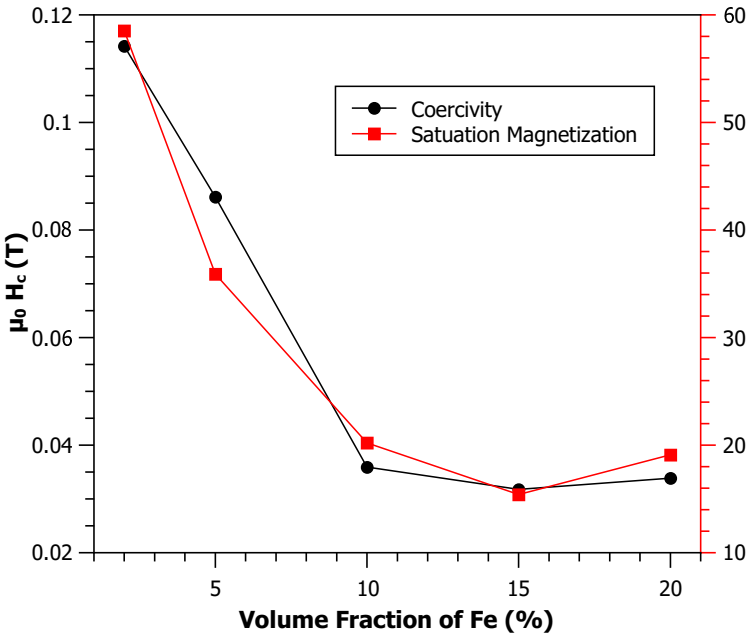

Figure 3.38: Variation of magnetic parameters for $FXU550$ series with respect to the different metallic volume fraction.

From the figure we find that coercivity H_c and saturation magnetization M_s decrease steeply till volume fraction of iron is 10% in the sample after which the parameters do not vary much.

3.5 Partial conclusion for ultrasonic mixed samples

1. Permalloy mixed bulk samples

   - All the bulk samples are prepared by spark plasma sintering of the mixtures obtained after ultrasonic mixing.
   - The samples with different composition (2,5,10,15,20 and 30) %, volume fraction of permalloy were sintered at two sintering temperatures: $500°C$ and $550°C$.
   - The samples were sintered for 10 minutes under argon atmosphere. The bulk samples of 8 mm × 1 mm were prepared.

- The structural characterization was performed using XRD. From the analysis of the diffraction pattern, we found that BaM phase was present in all the bulk samples.
- From the analysis, we find that the as the permalloy phase fraction was increased, the intermediate phase Fe_2O_3, i.e. maghemite fraction also increased.
- Although we found that the $FeNi_3$ fraction remains the same as the initial mixing volume fraction. Thus the only phase that disintegrates is the BaM phase. In the samples sintered at $550^{\circ C}$, $BaFe_2O_4$ phase is only present in sample with 15% and 20% of FeNi, in a small fraction.
- For the series of samples sintered at $500^{\circ C}$, the samples with volume fraction of 5%, 10%, 15% and 20% of FeNi were discussed. In this series of samples, for the samples with lower fraction of permalloy was found to have minor content of barium mono ferrite which disappears after volume fraction $> 10\%$.
- Magnetic properties are studied by VSM. Due to the disintegration of the barium ferrite and formation of maghemite phase, the magnetization in the samples increases but the bulk becomes soft magnetic in nature.
- Similar linear behavior in magnetization and coercivity with increasing volume fraction of bulk samples was found in the samples sintered at $500^{\circ}C$.
- Bulk samples sintered at $550^{\circ}C$ are found to have relatively higher values of coercivity H_C and saturation magnetization σ_s (fig. 3.25) in comparison to the bulk samples sintered at $500^{\circ}C$ (fig. 3.26).
- We also compared the variation of magnetization as a function of permalloy fraction with the theoretical values obtained (i) by considering the magnetization of each phases in their respective fractions and (ii) by considering the content of fraction of different phases analyzed from XRD.
- From comparison we found that the maximum theoretical limit of saturation magnetization was never reached. The theoretical saturation magnetization including the formation of phases (i.e. considering the reaction), we found that, the saturation magnetization reduced with the increasing volume fraction of permalloy.
- The magnetization calculated considering the reaction was found to be closer to the experimental values for the permalloy volume fraction $< 10\%$ for the samples sintered at $550^{\circ}C$. It was found that the experimentally measured samples achieve the magnetization which is 84% of the maximum limit of saturation without any reaction between the precursor phases.

Name	σ_s (Am^2/kg)	$\sigma_{s-theoretical}$ (Am^2/kg)	$\sigma_{s-with-reaction}$ (Am^2/kg)
N2U550	54.89	65.43	64.20
N5U550	58.59	67.3	63.86
N10U550	62.11	70.32	69.13
N15U550	64.61	73.15	70.09
N20U550	64.1	75.81	71.37
N30U550	68.26	80.63	79.71

Table 3.8: Influence of different percentage of iron-nickel in barium hexaferrite on the magnetic properties in $NXU550$ samples.

Name	σ_s (Am^2/kg)	$\sigma_{s-theoretical}$ (Am^2/kg)	$\sigma_{s-th-reaction}$ (Am^2/kg)
N5U550	46.29	67.3	63.86
N10U550	58.25	70.32	69.13
N15U550	57.73	73.15	70.09
N20U550	55.39	75.81	71.37

Table 3.9: Influence of different percentage of iron-nickel in barium hexaferrite on the magnetic properties in $NXU500$ samples.

- Magnetic properties are also studied as a function of the temperature (below room temperature) at 140 K and 200 K. The shape of the hysteresis is found to change to a small extent and the coercivity increases slightly at lower temperatures as shown in fig. 3.31.

2. Iron mixed bulk samples

   - Bulk samples with various volume fractions (2%, 5%, 10%, 15% and 20%) of iron were prepared by SPS at 550°C.
   - The XRD analysis showed that BaM phase disappeared with the increasing volume fraction of iron.
   - Magnetite phase was present in all the bulk samples. Most of iron was oxidized there by introducing the dominance of soft magnetic behavior in the sample. For $F2U550$ sample, barium possibly reacted with the carbon during sintering and formed barium carbonate occupying almost 2% of the total volume.
   - An intermediate phase $BaFe_2O_4$ was formed in the samples with higher volume fraction i.e. 5% and 10% of iron.
   - Magnetic properties deteriorate with increasing fraction of iron due to formation of unwanted oxides in the bulk samples. And the samples $F10U550$ and $F15U550$ show unusually small magnetization.

3. Comparison based on method of mixing

   - Since the samples were sintered at different temperatures we shall not can not exactly compare the two samples.
   - From the characterization techniques we found some peculiar differences in the samples prepared using the two methods. The samples with milling since were sintered at 800°C, the barium ferrite phase of found to disintegrate completely into magnetite phase and relatively small fraction of barium mono ferrite phase.
   - Sample made by ultrasonic mixing and sintered at 500°C and 550°C were found to retain comparatively large fraction BaM phase. BaM phase disintegrates into maghemite phase and very small fraction of mono ferrite phase.
   - Due to large disintegration of BaM in mechanically milled samples, the samples were very soft magnetic in nature more than those obtained using ultrasonic mixing.
   - The coercivities were found to be much larger in the ultrasonic mixed samples but there is no significant increase in saturation magnetization.

CHAPTER 4
MICROMAGNETICS

Chapter 4

Micromagnetics

Contents

4.1	Thermodynamic potentials for magnetic systems	**83**
4.2	Energy contributions	**84**
4.2.1	Exchange energy	85
4.2.2	Anisotropy energy	86
4.2.3	Magnetostatic energy	88
4.2.4	External field contribution	88
4.3	The free energy	**89**
4.4	Brown's equation	**89**
4.5	Landau-Lifshitz equation	**90**
4.6	Landau Lifshitz Gilbert equation	**90**
4.6.1	LLG in spherical co-ordinate system	92
4.7	Stoner-Wohlfarth model	**92**
4.8	Soft and hard material	**93**

In 1935, Landau and Lifshitz wrote a paper on the structure of a wall between two anti parallel domains; this and several papers by Brown around 1940, forms the foundation of *micromagnetics*. Micromagnetics was first demonstrated in details in a book by Brown in 1963 [72]. The theory uses classical physics in a continuous medium. The microscopic details of the atomic structure are ignored and the material is considered from a macroscopic point of view taking it to be continuous [73], [74], [75].

Earlier, micromagnetics was limited to using the energy minimization approach and classical nucleation theory to study the magnetization mechanism in the system. But it was found that this approach was only restricted to work out the domain structures and magnetization reversal and not necessarily determine exactly the state of the system after its reversal. Therefore, a lot of work has been devoted to the development of dynamical approach involving the Landau-Lifshitz (LL) equation of motion. In micromagnetics basically all atomic moments are replaced by a continuous vector $\mathbf{M}(\mathbf{r})$, which is function of the position vector $\mathbf{r}$.

The structure of micromagnetics includes interactions between magnetic moments over short and long-range spatial scale, ranging from few nanometers (nm) to few micrometers (μm). Hence we discuss the short range exchange and anisotropy interactions followed by comparative long range magnetostatic interactions. These interactions are described in terms of free energy of the system.

In this chapter, a general introduction of the thermodynamics potential is given for a magnetic body which explains the concept of free energy. It is followed by a brief explanation of the different contributing energy terms and a total free energy term described for a ferromagnet. We discuss Brown's equation in the next section and Landau Lifshitz (LL) equation is introduced to explain the magnetization dynamics. Model by Stoner Wolfharth is discussed in brief at the end of the section as a special case for uniformly magnetized body. A difference between Hard and Soft magnetic material is explained from theoretical point of view.

4.1 Thermodynamic potentials for magnetic systems

Any thermodynamic description is based on the ability to define the appropriate thermodynamic state function. The state function, or a state variable is a property of the system that depends only on the current state of the system and is independent of the path of the system through which the current state is achieved. A state function describes the equilibrium state of the system and a state quantity can be of energy type (internal energy U, enthalpy, free energies) or of entropy S, that describes the system quantitatively.

We describe the state quantities for a magnetic body. Let us assume a magnetic body of volume V and it consists of number of elementary moments $\mathbf{m}_i$. We consider a small volume dV inside a volume V of a magnetic body. dV is large enough to contain many moments. Let $\mathbf{H}_a$ be the external action on the system. Then according to the first law of thermodynamics,

$$dU = \mu_0 \mathbf{H}_a \cdot d\mathbf{m} + dQ \tag{4.1}$$

where U is the internal energy of the system and dQ is the heat absorbed by the system during the transformation from one state to another. It is known that $dQ = T\ dS$, where temperature T and entropy S are the conjugate variables for the thermal energy. The system is defined by the fixing one of the variables in the conjugate pairs, (S, T) and $(\mathbf{H}_a, \mathbf{m})$. We define the 4 thermodynamic potentials by fixing two variables. The 4 potentials are called as : *internal energy* $U(\mathbf{m}, S)$, *enthalpy* $E(\mathbf{H}_a, S)$, *Helmholtz free energy* $F(\mathbf{m}, T)$ and *Gibbs free energy* $G(\mathbf{H}_a, T)$. The equilibrium is reached when the appropriate potential reaches minimum.

At fixed temperature, T, the relevant potentials are $F = U - TS$ and $G = F - \mu_0 \mathbf{H}_a \cdot \mathbf{m}$. Since, the Gibbs free energy depends on external field and temperature, which are the variables that can be experimentally controlled, hence the two potential F and G are of interest.

The appropriate equilibrium condition for each potential can be determined by the second law of thermodynamics, which states that:

$$dS \geq \frac{dQ}{T} \tag{4.2}$$

If the system is in certain initial state and is then left isolated, it reaches the new equilibrium state and acquires new value of magnetic moment. This new equilibrium state is characterized by entropy S. Then according to the second law given by eq.(4.2), the change in entropy is always positive.

To study the transformation in a system at constant temperature, the variation of *Helmholtz free energy* is given as

$$dF = dU - TdS \tag{4.3}$$

Under constant temperature, we get the relation $dF \leq dU \leq \mu_0 \mathbf{H}_a \cdot \mathbf{m}$. If no work is done on the system then the *Helmholtz free energy* goes to minimum. The *Gibbs free energy* $G(\mathbf{H}_a, T)$, under constant temperature is given as

$$dG = -\mu_0 \mathbf{m} \cdot d\mathbf{H}_a \tag{4.4}$$

The negative sign in eq.(4.4) indicates that the *Gibbs free energy* also decreases towards minimum. The term $-\mu_0 \mathbf{m} \cdot d\mathbf{H}_a$, in fact, represents the potential energy of the body due to the elementary moments at an applied magnetic field H_a. We can see that $G(\mathbf{H}_a, T)$ depends only on $\mathbf{H}_a$ and T, thereby controlling the spontaneous transformation under fixed $\mathbf{H}_a$ and T. Any transformation of this kind can only proceed in the sense of producing a decrease of G. The thermodynamic equilibrium is reached when G attains a global minimum value. But G alone does not define the complete state of the system because in the magnetic system, the moment $\mathbf{m}$ varies during the process of relaxation, and the process leading to a certain value of $\mathbf{m}$ has characteristic relaxation time much shorter than time scale over which $\mathbf{m}$ varies significantly and the system globally approaches equilibrium. This implies that the system passes through a sequence of thermodynamic states, each state characterized by a well-defined value of $\mathbf{m}$. In the magnetic systems, free energy has many local minima corresponding to metastable equilibria.

The generalized energy of such (non-equilibrium) states, for a given $\mathbf{H}_a$ and T, is a function of $\mathbf{m}$, and is defined by a $G_L(\mathbf{m}; \mathbf{H}_a, T)$ called the *Landau free energy.* $\partial G_L / \partial \mathbf{m} = 0$ represents the metastable state of the system.

$$G_L(\mathbf{m}; \mathbf{H}_a, T) = F - \mu_0 \mathbf{H}_a \cdot \mathbf{m} \tag{4.5}$$

Thus whatever be the system, the first step is to write a good potential function and energy terms (i.e. to determine the full set of state variable necessary to define the state of the system). We shall explore the energy terms in the following sections one by one to write the free energy functional for magnetic bodies. From now on, we consider volume $\triangle V$ with uniform magnetization $\mathbf{M}$. We are interested in dependence of free energy on orientation of the magnetization. We assume, at a fixed temperature T, $|\mathbf{M}| = M_s$, where M_s is the saturation magnetization. At the same time, the elementary volume is such that $\triangle V$ is small enough with respect to characteristic length over which the magnetization varies significantly, so we can consider each volume having uniform properties. But also $\triangle V$ is large enough to contain significant number of elementary magnetic moments. So, magnetization $\mathbf{M}(\mathbf{r})$ is $\triangle V$ average.

For the generic elementary volume $\triangle V$ placed around the position $\mathbf{r}$, we indicate the free energy $\triangle G_L(\mathbf{M}(\mathbf{r}; \mathbf{H}_a, T))$. The function $\mathbf{M}$ is dependent on time t,

$$\mathbf{M} = \mathbf{M}(\mathbf{r}, t) \tag{4.6}$$

4.2 Energy contributions

In this section we discuss the contributions to the free energy functional for ferromagnetic bodies.

4.2.1 Exchange energy

The exchange interaction is a quantum mechanical phenomenon. It takes into account the spin-spin interactions on a scale of the order of the atomic distance and tends to order neighbor spins. The asymmetric nature of the electron states does not allow two electron with parallel spins to stay close to each other. The fact that they never get close reduces the average energy associated with their electrostatic interaction. This energy reduction favors the parallel configuration. These problems are described by Heisenberg Hamiltonian given as

$$\mathcal{H} = -2\mathcal{J}\mathbf{S}_i \cdot \mathbf{S}_j \tag{4.7}$$

where $\mathbf{S}_i$ and $\mathbf{S}_j$ are operators described by localized spins. $\mathcal{J}$ is nearest neighbor exchange integral, describing the strength of the exchange coupling between the spins i and j.

The force between the spins are sufficiently strong to keep the neighboring spins parallel. If S_i is not parallel to S_j, the scalar product decreases and the energy increases. We define unit vector $\mathbf{m}$ in direction $-\mathbf{S}_i$ such that $\mathbf{S}_i = -S\mathbf{m}_i$, where S is the spin magnitude. The exchange energy among spins can be written in terms of the angles $\phi_{i,j}$, between spin i and spin j, i.e. between the direction $\mathbf{m}_i$ and $\mathbf{m}_j$, as

$$F_{ex} = JS^2 \sum \phi_{i,j}^2 \tag{4.8}$$

The angles between neighbors are expected to be always small, because the exchange forces are very strong over a short range. Using the continuous variable $\mathbf{m}$ for magnetization, for small we get $|\phi_{i,j}| \approx |\mathbf{m}_i - \mathbf{m}_j|$. This also means that $\mathbf{m}$ is parallel to the local direction of the magnetization vector, $\mathbf{M}$, and $\mathbf{M}$ is continuous variable. Given that $\mathbf{m}$ does not vary from point to point too rapidly, we can extend such a variable by the first order expansion in a Taylor series

$$|\mathbf{m}_i - \mathbf{m}_j| = |(\mathbf{r}_i \cdot \nabla)\mathbf{m}| \tag{4.9}$$

where $\mathbf{r}_i$ is the position vector pointing from point i to j. Hence putting eq.(4.9) in eq.(4.8)

$$F_{ex} = JS^2 \sum \sum [(\mathbf{r}_i \cdot \nabla)\mathbf{m}]^2 \tag{4.10}$$

where the second summation is over the position vectors from lattice point i to all the neighbors. Changing the summation over i to an integral over the ferromagnetic body, and if $\mathbf{m} = m_x\mathbf{e}_x + m_y\mathbf{e}_y + m_z\mathbf{e}_z$, the result is that for cubic crystals and the exchange energy becomes

$$F_{ex} = \int f_{ex} dV, \tag{4.11}$$

$$f_{ex} = A\left[(\nabla m_x)^2 + (\nabla m_y)^2 + (\nabla m_z)^2\right] \tag{4.12}$$

where A is the exchange integral constant which is defines as $A = \dfrac{JS^2}{a}c$, where a is the edge of the unit cell, $c = 1, 2, 4$ for simple cubic, bcc and fcc respectively. For a hexagonal closed-packed crystal, summation over $\mathbf{s}_i$ vectors leads to same result as in eq.(4.12) with $A = \dfrac{4\sqrt{2}JS^2}{a}$, with a is the distance between nearest neighbors. The constant A is then taken as one of the physical parameters of the material, whose value is obtained by fitting the results of the theory to one of the measurement. It can be obtained from the theoretical expressions, whenever the exchange integral J is known. The constant A

takes into account the effect of short range interaction, it gives the idea of relation to the atomic scale parameter from eq.(4.7). This can be interpreted by treating $\mathbf{S}_i$ as classical vector and limiting the sum to nearest neighbor only. The value of $A = 10^{-11}\ J/m$.

4.2.2 Anisotropy energy

In ferromagnetic materials, when there is no external magnetic field, the material tends to magnetize along a certain energy-favored direction, also called *easy direction*. This is due to the structure of lattice and symmetries in the crystals. We can also assume that there is a force which tends to align magnetization along easy directions. In micromagnetics this force gives us phenomenological term in the free energy functional.

Considering again a volume $\triangle V$ with uniform magnetization $\mathbf{M}$, we are interested in the dependence of free energy $F_{AN}(\mathbf{m})$. We assume that $|\mathbf{M}| = M_s$ at a given fixed temperature T. Under these conditions the state of the system is described by magnetization unit vector $\mathbf{m} = \mathbf{M}/M_s$. The magnetization vector is related in the cartesian and spherical coordinates with the relation,

$$\begin{aligned} m_x &= \sin\theta\cos\phi \\ m_y &= \sin\theta\sin\phi \\ m_z &= \cos\theta \end{aligned} \tag{4.13}$$

The free energy density is given as

$$f_{an}(\mathbf{m}) = F_{an}/\triangle V \tag{4.14}$$

We assume that $f_{an}(\mathbf{m})$ is defined for a *constant* which is independent of $\mathbf{m}$. By choosing different values of this *constant* we get the energy surfaces with different quantitative details, but containing the same information on symmetry breaking. The presence of depressions in the energy surfaces shows space directions that are energetically favored. These directions are called *easy magnetization axes*. They represent the direction along which the magnetization tends to align in order to minimize the free energy. It satisfies the equilibrium condition under the constraint $|\mathbf{m}| = 1$.

$$\frac{\partial f_{an}(\mathbf{m})}{\partial \mathbf{m}} = 0 \tag{4.15}$$

The solution of eq.(4.15) represents local minima, saddle points or local maxima of the energy surface. A local minimum identifies an *easy axis*. Depending on the symmetry of the surface one may encounter many situations, where only one easy axis is present or sometimes a complex situation where multiple easy axes can even be present. Most of the fundamental metallic systems are either *uniaxial* or *cubic*.

Uniaxial Anisotropy

In this case only one direction controls the anisotropy energy. Let define this direction to be z-axis. The anisotropy energy $f_{an}(\mathbf{m})$ will be rotationally-symmetric with respect to the easy axis and will depend only on the relative orientation of $\mathbf{m}$ with respect to this axis. Therefore, we can write the expression of $f_{an}(\mathbf{m})$ as an even function of $m_z = \cos\theta$, or equivalently using as independent variable $m_x^2 + m_y^2 = 1 - m_z^2 = \sin^2\theta$. The energy density $f_{an}(\mathbf{m})$ has the following expansion

$$f_{an}(\mathbf{m}) = K_0 + K_1 \sin^2\theta + K_2 \sin^4\theta + ... \tag{4.16}$$

where K_0, K_1,K_2 are the ansiotropy constants with dimension of energy per unit volume J/m^3. The anisotropy axis is the easy axis for $\mathbf{m}$, with no preferential orientation, according to the fact that f_{AN} depends on even powers of m_z. This anisotropy is known as *easy-axis anisotropy.*

When $K_1 < 0$, the energy is at the minimum for $\theta = \pi/2$, the $\mathbf{m}$ points anywhere in $x-y$ plane. This situation is described as *easy-plane anisotropy.*

When $K_1 > 0$ and $\mathbf{m}$ lies along easy axis. For small deviations of magnetization from the equilibrium position, the anisotropy energy density can be approximated to second order in θ,

$$\begin{aligned} f_{an}(\mathbf{m}) &\cong K_1\theta^2 \cong 2K_1 - 2K_1\cos\theta \\ &= 2K_1 - \mu_0 M_s \frac{2K_1}{\mu_0 M_s}\cos\theta = 2K_1 - \mu_0 \mathbf{M}\cdot\mathbf{H}_{AN} \end{aligned} \tag{4.17}$$

The anisotropy energy is given as:

$$F_{an}(\mathbf{m}) = \int_V K_1[1(\mathbf{e}_{an}(\mathbf{r})\cdot\mathbf{m}(\mathbf{r}))^2]dV \tag{4.18}$$

where $\mathbf{e}_{an}$ is an easy axis unit-vector at the location $\mathbf{r}$ and the constant part connected to K_0 has been neglected.

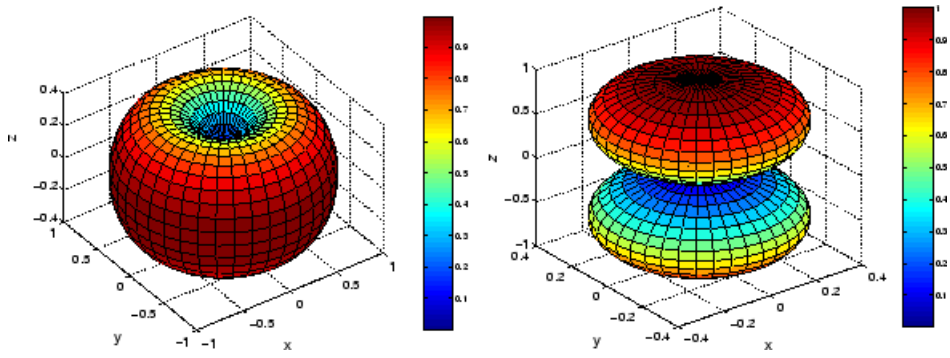

Figure 4.1: Uniaxial anisotropy energy density. On the Left, Easy axis anisotropy ($K_1 > 0$), On the Right, Easy plane anisotropy ($K_1 < 0$).

Cubic Anisotropy

If the anisotropy energy has cubic symmetry, it implies of presence of 3 easy axes, let them be $x-y-z$ axes. This is mostly due to spin-lattice coupling in cubic crystals. The lowest order combination of $\mathbf{m}$ possible gives the following anisotropy energy density,

$$f_{AN}(\mathbf{m}) = K_0 + K_1(m_x^2m_y^2 + m_y^2m_z^2 + m_z^2m_x^2) + K_2m_x^2m_y^2m_z^2 + ... \tag{4.19}$$

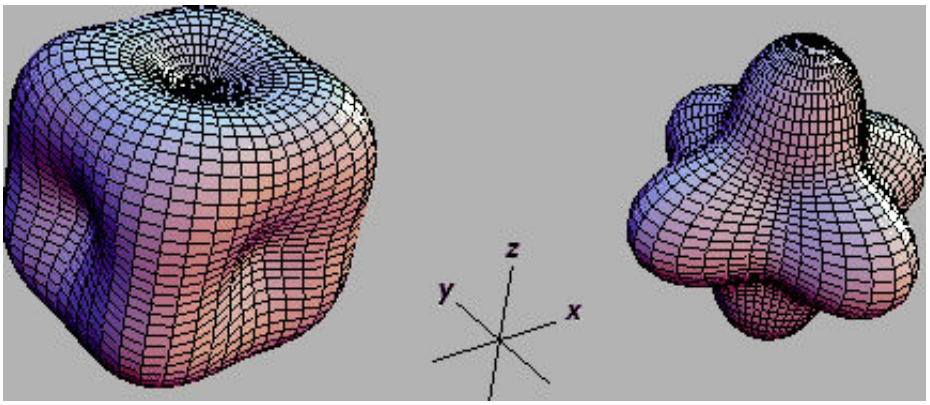

Figure 4.2: Cubic Anisotropy energy density of ($K_1 > 0$) on the left and ($K_1 < 0$) on the right.[Courtsey:Southampton-UK]

Another same analysis results in the anisotropy field $H_{AN} = 4|K_1|/3\mu_0 M_s$.

4.2.3 Magnetostatic energy

Magnetostatic energy is the potential energy of the magnetic moments in the field created by them. Magnetostatic interactions is a long range interaction. Now $\mathbf{M}$ is the magnetization of the body and we consider a magnetostatic field $\mathbf{H}_M$ created by $\mathbf{M}$. Then according to the Maxwell's equations:

$$\nabla \cdot \mathbf{H}_M = -\nabla \cdot \mathbf{M} \tag{4.20}$$

$$\nabla \times \mathbf{H}_M = 0 \tag{4.21}$$

The magnetostatic energy is given by [76]:

$$U_M = -\frac{\mu_0}{2} \int_V \mathbf{H}_M \cdot \mathbf{M} dV \tag{4.22}$$

$$U_M = \frac{\mu_0}{2} \int_V \mathbf{H}_M^2 dV$$

where the integral is calculated over whole space. The factor 1/2 is needed to take into account of the fact that each moment contributes twice to the sum, ones as field source and ones as the test moment. Thus we can express this energy as the integral over the body volume which shows that the contribution associated with each elementary volume is

$$F_m = \int_V \frac{1}{2} \mu_0 \mathbf{M} \cdot \mathbf{H}_m dV \tag{4.23}$$

4.2.4 External field contribution

The potential energy of the magnetic moments in the applied field $\mathbf{H}_a$.

$$F_a = -\mu_0 \mathbf{M} \cdot \mathbf{H}_a dV \tag{4.24}$$

This energy term is referred to as *Zeeman energy*.

4.3 The free energy

Now we are able to write the complete expression for the free energy of the ferromagnetic body. In fact, by collecting eq.(4.12), (4.14), (4.23) and (4.24),we have the expression of the landau free energy. So by summing up all the energy terms over all the elementary volumes and using space integral, where $\mathbf{M} = M_s\mathbf{m}$, we have

$$G_L(\mathbf{M}(\mathbf{r}), \mathbf{H}_a) = F_{ex} + F_{an} + F_m + F_a \quad (4.25)$$
$$= \int_V \left[A\left[(\nabla m_x)^2 + (\nabla m_y)^2 + (\nabla m_z)^2\right] + f_{an} - \frac{1}{2}\mu_0 \mathbf{M}\cdot\mathbf{H}_m - \mu_0 \mathbf{M}\cdot\mathbf{H}_a \right] dV$$

Now $G_L[\mathbf{M}(\mathbf{r})]$ is term representing the fact that the Landau energy is not a function of magnetization value at some point in space but depends on overall functional dependence of $\mathbf{M}$ on $\mathbf{r}$. This expression means that the thermodynamic equilibrium exists in each elementary volume $\triangle V$ even if the system is not globally at equilibrium.

4.4 Brown's equation

The final step in the formulation of classical micromagnetics is to minimize the total energy. We can write the expression for the first-order variation of the free energy function from eq.(4.3),

$$\delta G_L = -\int_V \left[2\nabla\cdot(A\nabla\mathbf{m}) + \frac{\partial f_{an}}{\partial \mathbf{m}} + \mu_0 M_s \mathbf{H}_m + \mu_0 M_s \mathbf{H}_a \right] \cdot \delta\mathbf{m} dV + \int_{dV} \left[2A \frac{\partial \mathbf{m}}{\partial \mathbf{n}} \cdot \delta\mathbf{m} \right] dS = 0 \quad (4.26)$$

where dS is a surface integral. The approach uses standard variational principles but the derivation is somewhat protracted. Essentially, setting the first variation of the total energy to zero leads to two equations. The first is a surface equation,

$$2A\left(\mathbf{m}\times\frac{\partial\mathbf{m}}{\partial n}\right) = 0 \Rightarrow \frac{\partial\mathbf{m}}{\partial n} = 0 \quad (4.27)$$

since $\mathbf{m}\cdot\partial\mathbf{m}/\partial n = 0$ by virtue of $\mathbf{m}\cdot\mathbf{m} = 1$. This implies that the vectors $\mathbf{m}$ and $\partial\mathbf{m}/\partial n$ are always orthogonal, and their vector product can only vanish if $\partial\mathbf{m}/\partial n$ is zero. The volume equation,

$$\delta G_L = -\int_V \mathbf{m}\times\left[2\nabla\cdot(A\nabla\mathbf{m}) + \frac{\partial f_{an}}{\partial\mathbf{m}} + \mu_0 M_s\mathbf{H}_m + \mu_0 M_s\mathbf{H}_a \right]\cdot\delta\mathbf{m}dV = 0 \quad (4.28)$$

$$\mathbf{m}\times\left[2\nabla\cdot(A\nabla\mathbf{m}) - \frac{\partial f_{an}}{\partial\mathbf{m}} + \mu_0 M_s\mathbf{H}_m + \mu_0 M_s\mathbf{H}_a \right] = 0 \quad (4.29)$$

From there we can introduce the effective field, $\mathbf{H}_{eff}$

$$\mathbf{H}_{eff} = \frac{2}{\mu_0 M_s}\nabla\cdot(A\nabla\mathbf{m}) - \frac{1}{\mu_0 M_s}\frac{\partial f_{an}}{\partial\mathbf{m}} + \mathbf{H}_m + \mathbf{H}_a \quad (4.30)$$

Thus we can write eq.(4.27), eq.(4.29) as:

$$\mu_0 M_s\mathbf{m}\times\mathbf{H}_{eff} = 0 \quad (4.31)$$
$$\frac{\partial\mathbf{m}}{\partial\mathbf{n}}|_{dV} = 0$$

Eq.(4.31) are called Brown's equations which allow us to find the equilibrium of the material. The first equation shows that the torque exerted on the magnetization by the effective field is zero at equilibrium.

4.5 Landau-Lifshitz equation

Brown's equation determines all possible magnetization equilibria regardless of their stability. However, according to the thermodynamic principle of free energy minimization, only minima of G will correspond to stable equilibria and, thus, will be in principle physically observable.

Up till now, we haven't spoken about the response of the system to a time-varying applied field. There is a torque N which is exerted by the field acting on the magnetic moment and similar holds for the magnetization vector $\mathbf{m} = \mathbf{M}/M_s$. The relevant field exerting torque on the moments is the field $\mathbf{H}_{eff}$.

Let $\mathbf{M}(\mathbf{r},t)$ be the magnetization vector describing the state of a system. $\mathbf{M}(\mathbf{r},t)$ defines the local magnetization in the system. If $\mathbf{M} \times \mathbf{H}_{eff} \neq 0$, the system is not in equilibrium and thus will evolve in time according to appropriate dynamic equation. This required dynamic equation was proposed by Landau and Liftshiz. It is mostly used for describing the magnetization dynamics. A field $\mathbf{H}_{eff}$ induces precession of local magnetization $\mathbf{M}(\mathbf{r};t)$ in a ferromagnetic body of the form:

$$\frac{\partial \mathbf{M}}{\partial t} = -\gamma \mathbf{M} \times \mathcal{H} \tag{4.32}$$

where $\gamma > 0$ determines the precession rate. In the following, for simplicity we shall identify with the gyromagnetic ratio associated with the electron spin, which yields $\gamma = 2.2 \times 10^5 A^{-1} m s^{-1}$. The magnitude of magnetization $|\mathbf{M}|$ is conserved. Indeed, $M \cdot \partial \mathbf{M}/\partial t = 0$ is an immediate consequence of eq.(4.32). Thus, eq.(4.32) is consistent with the fundamental micromagnetic constraint $|\mathbf{M}(\mathbf{r}, t)| = M_s$.

Energy relaxation mechanisms can be taken into account by introducing an additional phenomenological term chosen through heuristic considerations. In their original paper, Landau and Lifshitz described damping by a term proportional to the component of $\mathbf{H}_{eff}$ that is perpendicular to the magnetization:

$$\frac{\partial \mathbf{M}}{\partial t} = -\gamma_L \mathbf{M} \times \mathbf{H}_{eff} + \alpha \gamma_L M_s \left(\mathbf{H}_{eff} - \mathbf{M} \frac{\mathbf{M} \cdot \mathbf{H}_{eff}}{M_s^2} \right) \tag{4.33}$$

Here, γ_L is a gyromagnetic-type constant which may be different from γ in eq.(4.32) , while α is a damping constant. The rationale behind eq.(4.33) can be explained as follows. The effective field $\mathbf{H}_{eff}$ identifies in $\mathbf{M}$-space the direction of steepest energy decrease, so it would be the natural direction for magnetization relaxation. However, the magnetization magnitude must be preserved as well. This suggests that only the $\mathbf{H}_{eff}$ component perpendicular to $\mathbf{M}$ may contribute to $\partial \mathbf{M}/\partial t$. It is apparent that this component coincides with the vector $-\mathbf{M} \times (\mathbf{M} \times \mathbf{H}_{eff})/M_s^2$. Eq.(4.33) can also be written as:

$$\frac{\partial \mathbf{M}}{\partial t} = -\gamma_L \mathbf{M} \times \mathbf{H}_{eff} - \frac{\alpha \gamma_L}{M_s} \mathbf{M} \times (\mathbf{M} \times \mathbf{H}_{eff}) \tag{4.34}$$

This is the form in which the Landau Lifshitz equation is mostly used in the literature.

4.6 Landau Lifshitz Gilbert equation

Gilbert proposed another equation for the description of magnetization dynamics in ferromagnets.

$$\frac{\partial \mathbf{M}}{\partial t} = -\gamma_G \mathbf{M} \times \mathbf{H}_{eff} + \frac{\alpha}{M_s} \mathbf{M} \times \frac{\partial \mathbf{M}}{\partial t} \tag{4.35}$$

This equation is equivalent to eq.(4.34) by the relation:

$$\frac{\gamma_G}{\gamma_L} = 1 + \alpha^2 \tag{4.36}$$

It is very useful to write the micromagnetic equation in dimensionless units. To normalize the micromagnetic free energy equation, we divide the free energy by $\mu_0 M_s^2 V$. $\mathbf{G}(\mathbf{M}, \mathbf{H})$ is the micromagnetic free energy, the magnetization and fields are measured in the units of M_s, the energies in the units of $\mu_0 M_s^2 V$, where V is the volume of the system,

$$\mathbf{G}_L(\mathbf{M}, \mathbf{H}) = \int \left(A(\nabla \mathbf{M}/M_s)^2 + f_{an} - \frac{\mu_0}{2} \mathbf{M} \cdot H_m - \mu_0 \mathbf{M} \cdot H_a \right) d^3\mathbf{r} \tag{4.37}$$

In the normalized form, $\mathbf{g}_L = \dfrac{\mathbf{G}_L}{\mu_0 M_s^2 V}$, we get,

$$\mathbf{g}_L = \frac{1}{V} \int \left(\frac{A}{\mu_0 M_s^2} (\nabla \mathbf{m})^2 + \frac{1}{\mu_0 M_s^2} f_{an} - \frac{1}{2} \mathbf{h}_m \cdot \mathbf{m} - \mathbf{h}_a \cdot \mathbf{m} \right) dv \tag{4.38}$$

where v is measured in the units of V. The effective field is defined as $\mathbf{h}_{eff} = -\dfrac{d\mathbf{g}_L}{d\mathbf{m}}$

$$\mathbf{H}_{eff} = \mathbf{H}_{ex} + \mathbf{H}_{an} + \mathbf{H}_m + \mathbf{H}_a \tag{4.39}$$

$$\mathbf{h}_{eff} = \frac{\mathbf{H}_{eff}}{M_s} = \frac{2}{\mu_0 M_s^2} \nabla \cdot (A\mathbf{m}) - \frac{1}{\mu_0 M_s^2} \frac{\partial f_{an}}{\mathbf{m}} + \mathbf{h}_m + \mathbf{h}_a \tag{4.40}$$

In the eq.(4.40), we find a constant parameter with the dimension of length, we call this parameter as exchange length.
Exchange length:
The exchange length one of the significant parameter. It controls the width of the transition between magnetic domains [26].

$$l_{ex} = \sqrt{\frac{2A}{\mu_0 M_s^2}} \tag{4.41}$$

Since l_{ex} is very small of the order of few nm and over this length, the exchange interaction is predominant, therefore on this spatial scale, the magnetization is spatially uniform.

Domain wall width:
Another parameter we encounter in the magnetization dynamics description is the domain wall width,l_w, which is the ratio of the exchange and the anisotropy of the system,

$$l_w \sqrt{\frac{A}{K_{mc}}} \tag{4.42}$$

Dividing the eq.(4.35) by γM_s^2, we get,

$$\frac{1}{\gamma M_s^2} \frac{\partial \mathbf{M}}{\partial t} = -\frac{1}{M_s^2} \mathbf{M} \times \mathbf{H}_{eff} + \frac{\alpha}{\gamma M_s^3} \mathbf{M} \times \frac{\partial \mathbf{M}}{\partial t} \tag{4.43}$$

Measuring the time in units of $(\gamma M_s)^{-1}$, $\gamma = 2.2 \times 10^5 Am^{-1}$, and putting $\mathbf{m} = \mathbf{M}/M_s$, the normalized LLG equation is:

$$\frac{\partial \mathbf{m}}{\partial t} - \alpha \mathbf{m} \times \frac{\partial \mathbf{m}}{\partial t} = -\mathbf{m} \times \mathbf{h}_{eff} \tag{4.44}$$

The normalized LL equation is given as,

$$\frac{\partial \mathbf{m}}{\partial t} = -\mathbf{m} \times \mathbf{h}_{eff} - \alpha \mathbf{m} \times (\mathbf{m} \times \mathbf{h}_{eff}) \tag{4.45}$$

4.6.1 LLG in spherical co-ordinate system

The unit vector $\mathbf{m}$ is defined by two spherical angles θ and ϕ as:

$$m_x = sin\theta cos\phi, \;\; m_y = sin\theta sin\phi, \;\; m_z = cos\theta \tag{4.46}$$

The vectors along the directions of θ and ϕ will be denoted as $\mathbf{e}_\theta$ and $\mathbf{e}_\phi$.

Thus the LLG equation projected along θ and ϕ is

$$\frac{d\theta}{dt} + \alpha \frac{d\phi}{dt} = -\frac{1}{sin(\theta)} \frac{\partial g_L}{\partial \phi} \tag{4.47}$$

$$-\alpha \frac{d\theta}{dt} + sin(\theta) \frac{d\phi}{dt} = \frac{\partial g_L}{\partial \theta} \tag{4.48}$$

In the spherical coordinates, the conservation law is given as $\mid \mathbf{m} \mid = 1$. Thus the magnetization dynamics can be assumed to occur on the unit sphere and this makes it easier to study.

4.7 Stoner-Wohlfarth model

Stoner-Wohlfarth(SW) model was proposed in 1948 by Stoner and Wohlfarth. It is the simplest micromagnetic model to study the single domain particle. It assumes spheroidal geometry of the particle and uniaxial anisotropy along the rotational-symmetry axis. The magnetization is uniform within the body hence the exchange energy gives zero contribution to the free energy.

The magnetostatic field gives a simple contribution due to the ellipsoidal geometry.

$$\mathbf{H}_m = -\mathbf{N} \cdot \mathbf{M} \tag{4.49}$$

where N is the demagnetizing factor. We can express N with respect to its principal axes x,y, z, which coincide with the principal axes of the ellipsoid,

$$\begin{pmatrix} H_x \\ H_y \\ H_z \end{pmatrix} = - \begin{bmatrix} N_x & 0 & 0 \\ 0 & N_y & 0 \\ 0 & 0 & N_z \end{bmatrix} \cdot \begin{pmatrix} M_x \\ M_y \\ M_z \end{pmatrix} \tag{4.50}$$

where N_x, N_y, N_z are the demagnetizing factors such that $N_x + N_y + N_z = 1$. Then, the assumption of uniaxial anisotropy implies that the corresponding energy term is quadratic. For instance, if the easy axis is the z-axis, then $\mathbf{e}_{an} = \mathbf{e}_z$ and the anisotropy energy becomes:

$$F_{an}(\mathbf{m}) = K_1(1 - m_z^2)V_0 \tag{4.51}$$

where V_0 is the volume of the spheroidal particle. Finally, the hypothesis of rotational symmetry implies that $N_x = N_y = N_\perp$. Thus the free energy

$$G(\mathbf{m}, \mathbf{H}_a) = K_1(1 - m_z^2)V_0 + \frac{1}{2}\mu_0 M_s^2 \mathbf{m} \cdot N \cdot \mathbf{m} V_0 - \mu_0 M_s \mathbf{m} \cdot \mathbf{H}_a V_0 \tag{4.52}$$

In the dimensionless form, we get,

$$g(\mathbf{m}, \mathbf{h}_a) = \frac{K_1}{\mu_0 M_s^2}(1 - m_z^2) + \frac{1}{2}N_\perp(1 - m_z^2) + \frac{1}{2}N_z m_z^2 - \mathbf{m} \cdot \mathbf{h}_a \tag{4.53}$$

$$k_{eff} = N_\perp + \frac{2K_1}{\mu_0 M_s^2} - N_z \tag{4.54}$$

Eq.(4.53) takes the form

$$g(\mathbf{m}, \mathbf{h}_a) = -\frac{1}{2}k_{eff} m_z^2 - \mathbf{m} \cdot \mathbf{h}_a \tag{4.55}$$

here, k_{eff} takes into account shape and crystalline anisotropy. Introducing the spherical coordinates, let θ be the angle between $\mathbf{m}$ and $\mathbf{e}_z$ and θ_h be the angle between $\mathbf{h}_a$ and $\mathbf{e}_z$. By using this, eq.(4.55) becomes,

$$\begin{aligned} g(\mathbf{m}, \mathbf{h}_a) &= -\frac{1}{2}k_{eff}\cos^2\theta - h_a\cos(\theta_h - \cos\theta) \\ &= -\frac{1}{2}k_{eff}\cos^2\theta - h_{az}\cos\theta - h_{a\perp}\sin\theta \end{aligned} \tag{4.56}$$

where, h_{az} and $h_{a\perp}$ are parallel and perpendicular component of applied field. Eq.(4.7) has a solutions at $\sin\theta = 0$, i.e., $\theta = 0$ or π. In order to find the solutions one needs to minimize the energy [77], i.e. to find

$$\frac{\partial g}{\partial \theta} = 0 \tag{4.57}$$

This gives us a minimum or a maximum energy configuration. The SW model is still extensively used.

4.8 Soft and hard material

We shall first define the terms Soft and Hard magnetic material from the micromagnetic point of view.

In general, we find that most of the magnetic materials have uniaxial or cubic anisotropy. Using the ansiotropy field defined in eq.(4.2.2) , $H_{an} = 2K_1/\mu_0 M_s$ we define a new dimensionless constant k

$$k = \frac{H_{AN}}{M_s} = \frac{2K_1}{\mu_0 M_s^2} \tag{4.58}$$

This ratio defined in eq.(4.58), gives a natural measure of the relative strength of anisotropy versus magnetostatic effects. If the material is *soft*, then the magnetostatic effects will be dominant, hence for such materials, $k << 1$. In the *hard* materials, anisotropy dominates, leading to $k \gtrsim 1$.

CHAPTER 5
MICROWAVE ASSISTED MAGNETIZATION DYNAMICS

Chapter 5

Microwave Assisted Magnetization Dynamics

Contents

5.1	Single phase magnetic system		**99**
	5.1.1	P-modes	102
	5.1.2	Phase diagrams for magnetic reversal	105
5.2	Exchange coupled bilayer system		**112**
	5.2.1	Macrospin theory	120
	5.2.2	Variation of the microwave field frequency	121
5.3	Summary		**124**
5.4	Conclusion		**124**

With the tremendous demand in electronic storage technology new strategies are being continuously tested to overcome the so called "recording trilemma", which is the challenging incongruity between storage density, thermal stability, and easy writing ability, as explained in section 1.3. To understand the phenomena behind these processes, we need to have a grasp of the dynamics of magnetization reversal processes. Among the solutions proposed for the "recoding trilemma", we focus our attention on *microwave assisted switching* in perpendicular magnetic media (section 1.3).

Garcia-sanchez et al. [32] proved using micromagnetic modeling that *exchange spring media* (ESM) with *perpendicular anisotropy* is one of the most reliable ways to reduce the switching field of the memories. ESM also makes it easier to write data on the storage devices while maintaining thermal stability.

The magnetization dynamics described by the Landau Lifshitz (LL) equation and Landau Lifshitz Gilbert (LLG) equation has been introduced in section 4.5. These equations are nonlinear in nature. The spatial distribution of magnetization exhibits very complex features such as nonlinear resonance, quasi periodicity, chaos, turbulence-like dynamics and nonlinear wave propagation [78]. But these equations, under certain conditions on geometrical and physical properties of the system allow exact *spatially uniform solutions*.

In this chapter, we focus on the reversal process in exchange spring systems. Our main aim is to study the bilayer system, i.e two magnetic phases, hard and soft, exchange coupled at the interface. In this regard, we first study the dynamics in a single magnetic phase system subjected to a circularly polarized microwave magnetic field. We assume that the system

has uniaxially perpendicular anisotropy, and we choose the geometry such that the magnetization is spatially uniform (details are given in section 5.1). The dynamical equation for single phase media depends on time through the rotating microwave field, introduced to assist the switching process. To overcome the complex nature of the problem, we exploit the symmetry of the system using a rotating frame. The dynamics of uniform solution in a single phase system subjected to microwave field have been analytically solved by Bertotti et al. [79]. The single phase magnetic media offers certain stable solution, critical or fixed point which in the laboratory frame, rotate uniformly around the symmetry axis. These periodic rotating solutions have been termed as **P-modes**. There are some solutions for which the magnetization is rotating around the symmetry axis, which show limit cycles in the laboratory frame, such quasi periodic solutions are named **Q-modes**.

The study of single phase system gives us the basic understanding for studying the bilayer systems. We study the magnetization dynamics in the bilayer system which is composed of the two magnetic phases, a hard and a soft, details of which are given in section 5.2. The difficulty in studying the bilayer system is that, the magnetization is not only a function of time, but also a function of space (in our particular case, it depends on the spatial component z). The spatial non-uniformity in magnetization is due to the coupling at the interface between the two phases. When the bilayer system is subjected to the circularly polarized microwave field, it becomes very difficult to find the analytical solution of the LLG equation (section 5.2). The problem becomes complex because we do not have uniform solutions. Therefore, we analyze the dynamical process by numerically integrating the LLG equation using finite difference method.

The main result of this numerical approach is to show that, under general conditions, the bilayer system behaves as two distinct **P**-modes naming, the soft layer and the hard layer. This **P**-mode behavior gives us the clue to use the combination of numerical and analytical solution. We studied the magnetization reversal process in the bilayer spring system, where it is known that there are two fields controlling the process of magnetization reversal of spring systems, particularly *nucleation field* and *propagation field*. For magnetic multilayer systems, it has been shown that the leading field in the reversal process is the *nucleation field*, H_N for thin systems and the *propagation field*, H_P for thick systems (i.e. in the limit of infinite thickness of the layers) [80]. In an analytical micromagnetic approach by *Zhao et al.* nucleation and pinning fields have been derived for an exchange-coupled hard/soft/hard magnetic nanosystem. They compared and studied the coercivity mechanisms quantitatively using the analytical formulas with the numerical and experimental coercivity [81].

In this work, we focus on the magnetization reversal in the system with infinite thickness, in which the nucleation takes place since the very beginning of the process in the soft phase whereas the complete reversal (i.e. switching) is associated with the propagation of the reverse domain through the hard layer. The novelty in this work is threefold: we try to understand the non linear dynamics in an exchange spring media, secondly we focus on the microwave assisted reversal in the limit of infinite thickness and thirdly, since there is no analytical solution, we combine the analytical solution of the uniform system and the numerical solutions of the bilayer system to describe the dynamics of the system.

First we begin with writing down the LLG equation,

$$\frac{\partial \mathbf{M}}{\partial t} = -\gamma_G \mathbf{M} \times \mathbf{H}_{eff} + \frac{\alpha}{M_s} \mathbf{M} \times \frac{\partial \mathbf{M}}{\partial t} \tag{5.1}$$

Where $\mathbf{M}(\mathbf{r}, t)$ is the magnetization vector and $|\mathbf{M}(\mathbf{r}, t)| = M_s$ is the saturation magneti-

zation, $\mathbf{r}$ is the position vector and t is the time. The units of measurement are the *S.I.* units. γ_G is the electron gyromagnetic ratio, α is the damping constant and $\mathbf{H}_{eff}$ is the effective field. The effective field can be given as $\mathbf{H}_{eff} = -\partial G_L/(\mu_0 M_s V \ \partial \mathbf{m})$, where V is the volume of the system and G_L is the Landau free energy of the system.

It becomes easy to transform these equations in dimensionless form, as seen in section 4.6. Normalizing the equation allow us to define the quantities in more insightful way. Measuring the magnetization and field in the units of M_s, by describing the magnetization state by a unit vector $\mathbf{m}(\mathbf{r}, t) = \mathbf{M}(\mathbf{r}, t)/M_s$, and $\mathbf{h}_{eff} = \mathbf{H}_{eff}/M_s$ and time is measured in the units of $(\gamma \mu_0 M_s)^{-1}$, we get

$$\frac{\partial \mathbf{m}}{\partial t} - \alpha \mathbf{m} \times \frac{\partial \mathbf{m}}{\partial t} = -\mathbf{m} \times \mathbf{h}_{eff} \tag{5.2}$$

Eq.(5.2) is the dimensionless form of LLG equation. The dimensionless landau energy is given as

$$\mathbf{g}_L(\mathbf{m}, \mathbf{h}_a) = \frac{\mathbf{G}_L(\mathbf{M}, \mathbf{H}_a)}{\mu_0 M_s^2 V} \tag{5.3}$$

$\mathbf{H}_a$ denotes the applied field and $\mathbf{h}_a = \mathbf{H}_a/M_s$. Thus the dimensionless effective field is given as $\mathbf{h}_{eff} = -\partial \mathbf{g}_L/\partial \mathbf{m}$.

The external applied field $\mathbf{h}_a(t)$ is a combination of a DC field $\mathbf{h}_{az}$ directed along the z-axis and an in-plane circularly polarized field of magnitude $h_{a\perp}$ of angular frequency ω, applied in the plane of the system. The total external magnetic field is given by

$$\mathbf{h}_a(t) = h_{a\perp}(\cos \omega t \ \ \mathbf{e}_x + \sin \omega t \ \ \mathbf{e}_y) + h_{az}\mathbf{e}_z \tag{5.4}$$

where $(\mathbf{e}_x, \mathbf{e}_y, \mathbf{e}_z)$ are the unit vectors along x, y and z directions respectively. The magnetization vector follows the constraint $|\mathbf{m}| = 1$ ($|\mathbf{M}| = M_s$).

It can be clearly seen that the dynamics depend explicitly on time through the external field $\mathbf{h}_a(t)$. The complex nature of the problem due to this dependence can be avoided by exploiting the rotational symmetry of the problem. We use the rotating frame of reference which is symmetric about z axis and rotates with angular frequency ω around $\mathbf{e}_z$ axis as shown in fig.5.1.

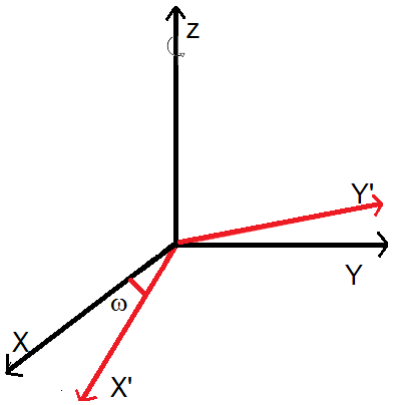

Figure 5.1: Rotating frame (x', y') given in red, is symmetric about z-axis and is rotated by the angle ωt.

In the rotating frame, given by (x', y'), $\mathbf{h}_{eff}$ is time independent. The transformation is given by:

$$\left(\frac{d\mathbf{m}}{dt}\right)_{lab} = \left(\frac{d\mathbf{m}}{dt}\right)_{rotation} - \omega \mathbf{e}_z \times \mathbf{m} \tag{5.5}$$

Using the eq.(5.5), we write the LLG equation in rotating frame. Dropping out the subscript for the frame of reference, the LLG equation in rotating frame becomes:

$$\frac{d\mathbf{m}}{dt} - \alpha \mathbf{m} \times \frac{d\mathbf{m}}{dt} = -\mathbf{m} \times (\mathbf{h}_{eff} - \omega \mathbf{e}_z + \alpha\omega \mathbf{m} \times \mathbf{e}_z) \tag{5.6}$$

The unit vectors in rotating frame are given by $e_{x'}, e_{y'}$ and e_z. For convenience we drop the prime ($\prime$). All the parameters remain the same, however the applied field is given by

$$\mathbf{h}_a = h_{a\perp}\mathbf{e}_x + h_{az}\mathbf{e}_z \tag{5.7}$$

In the following section, we discuss the single phase magnetic systems.

5.1 Single phase magnetic system

Fig.5.2 represents a schematic for a single magnetic phase system. We consider the single phase system having a uniaxial perpendicular anisotropy directed along z-axis. We assume the system to be infinite in plane (i.e. x-y plane) and the thickness of the system is measured along z-axis. This makes the demagnetization factors N_x and N_y equal to zero and since $N_x + N_y + N_z = 1$ implies that $N_z = 1$. We neglect the surface anisotropy effects.

Under these conditions, the magnetization is expected to be uniform in space. It is important to study these spatially uniform solutions because:

- From the practical point of view, the storage devices etc. are designed in the nano scale range. And at such scale, the dominant mode of operation remains spatially uniform in nature.
- Uniform mode theory provides the basis for complex situations.

The magnetization $\mathbf{m}$ in Cartesian coordinates is described by the components m_x, m_y and m_z along the unit vectors $\mathbf{e}_x, \mathbf{e}_y$ and $\mathbf{e}_z$ respectively. K is the anisotropy constant of the system measured in J/m^3 and the normalized magnetocrystalline anisotropy constant is denoted by $k = (2K_1/\mu_0 M_s^2)$. This constant can be included with the shape ansiotropy term, which in this case is $-m_z\mathbf{e}_z$, thus, the total effcetive anisotropy term is given by k_{eff},

$$k_{eff} = (k - 1) \tag{5.8}$$

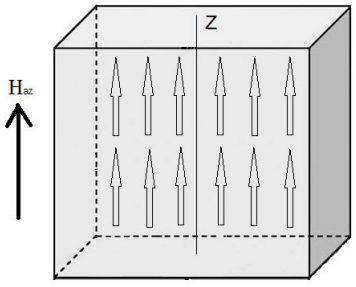

Figure 5.2: Representation of the Single phase magnetic system with perpendicular anisotropy.

Under the above stated conditions, the total effective field acting on the system is given by:

$$\mathbf{h}_{eff} = \mathbf{h}_a + (k_{eff} m_z)\mathbf{e}_z \tag{5.9}$$

In the spherical coordinate system, the magnetization vector is along the unit vectors $(\mathbf{e}_m, \mathbf{e}_\theta, \mathbf{e}_\phi)$ and is given, eq.(5.10).

$$\mathbf{m} = \sin\theta\cos\phi\ \ \mathbf{e}_x + \sin\theta\sin\phi\ \ \mathbf{e}_y + \cos\theta\ \ \mathbf{e}_z \tag{5.10}$$

where, θ is the angle between the z-component of magnetization, m_z and z-axis and ϕ is the angle between the in-plane component of magnetization, $m_\perp = \sqrt{m_x^2 + m_y^2}$ and the perpendicular component of in-plane circularly polarized field is $\mathbf{h}_\perp$ (see fig.5.3).

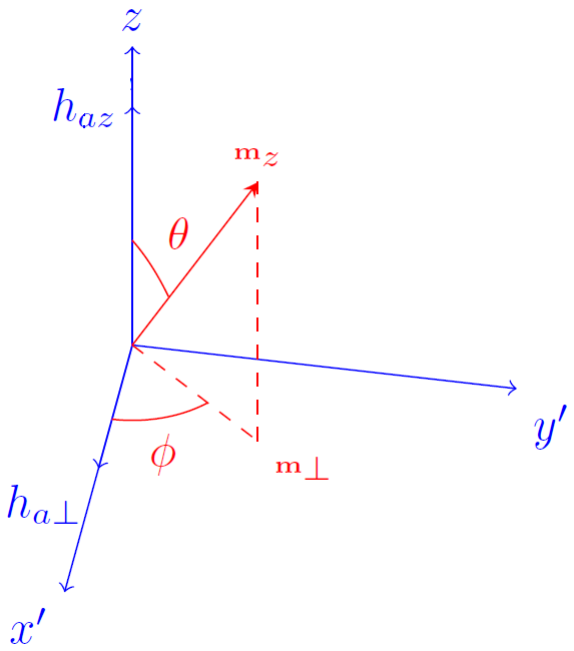

Figure 5.3: Representation of magnetization components m_z,$m_\perp$ in the rotating frame (x', y'). The applied in-plane circularly polarized field $h_{a\perp}$ acts along x' and makes an angle ϕ with $m_\perp$.

Performing time derivative of $\mathbf{m}$ in the spherical coordinates we have,

$$\frac{d\mathbf{m}}{dt} = \frac{d\theta}{dt}\mathbf{e}_\theta + \sin\theta\frac{d\phi}{dt}\mathbf{e}_\phi \tag{5.11}$$

$\mathbf{h}_{eff}$ in the spherical coordinates is given as,

$$\mathbf{h}_{eff} = (k_{eff}\cos\theta + h_{az})(-\sin\theta)\mathbf{e}_\theta + h_{ap}(\cos\theta\cos\phi\ \ \mathbf{e}_\theta - \sin\phi\ \ \mathbf{e}_\phi) \tag{5.12}$$

$$\mathbf{h}_{eff} = h_{eff,\theta}\ \ \mathbf{e}_\theta + h_{eff,\phi}\ \ \mathbf{e}_\phi \tag{5.13}$$

The terms in the LLG equation are given as:

$$\mathbf{m} \times \frac{d\mathbf{m}}{dt} = \begin{vmatrix} \mathbf{e}_m & \mathbf{e}_\theta & \mathbf{e}_\phi \\ 1 & 0 & 0 \\ 0 & \frac{d\theta}{dt} & \sin\theta \frac{d\phi}{dt} \end{vmatrix}$$
$$= -\sin\frac{d\phi}{dt}\mathbf{e}_\theta + \frac{d\theta}{dt}\mathbf{e}_\phi \tag{5.14}$$

$$\mathbf{m} \times \mathbf{h}_{eff} = \begin{vmatrix} \mathbf{e}_m & \mathbf{e}_\theta & \mathbf{e}_\phi \\ 1 & 0 & 0 \\ 0 & h_{eff,\theta} & h_{eff,\phi} \end{vmatrix} \tag{5.15}$$
$$= -h_{eff,\phi}\mathbf{e}_\theta + h_{eff,\theta}\mathbf{e}_\phi$$

$$\mathbf{m} \times \mathbf{e}_z = \begin{vmatrix} \mathbf{e}_m & \mathbf{e}_\theta & \mathbf{e}_\phi \\ 1 & 0 & 0 \\ 0 & -\sin\theta & 0 \end{vmatrix} \tag{5.16}$$
$$= -\sin\theta \quad \mathbf{e}_\phi$$

$$\mathbf{m} \times (\mathbf{m} \times \mathbf{e}_z) = \begin{vmatrix} \mathbf{e}_m & \mathbf{e}_\theta & \mathbf{e}_\phi \\ 1 & 0 & 0 \\ 0 & 0 & -\sin\theta \end{vmatrix}$$
$$= \sin\theta \quad \mathbf{e}_\theta \tag{5.17}$$

Thus, projecting eq.(5.6) along the constant ϕ and constant θ and substituting eq.(5.13) and eq.(5.10), eq.(5.14)-eq.(5.17) in eq.(5.6), we get

$$\frac{d\theta}{dt} + \alpha\sin\theta\frac{d\phi}{dt} = -h_{a\perp}\sin\phi - \alpha\omega\sin\theta \tag{5.18}$$
$$-\alpha\frac{d\theta}{dt} + \sin\theta\frac{d\phi}{dt} = -h_{a\perp}\cos\phi\cos\theta + (h_{az} - \omega + k_{eff}\cos\theta)\sin\theta \tag{5.19}$$

When the system reaches equilibrium, i.e. stationary state, the time derivative is zero. By setting $\frac{d\theta}{dt} = \frac{d\phi}{dt} = 0$, we obtain the equations for the fixed (critical) points of the dynamics in the rotating frame. Thus eq.(5.18) and eq.(5.19) becomes

$$-h_{a\perp}\sin\phi - \alpha(k\cos\theta\sin\theta - h_{a\perp}\cos\theta\cos\phi + h_{az}\sin\theta) = 0 \tag{5.20}$$

$$k\cos\theta\sin\theta - h_{a\perp}\cos\theta\cos\phi + h_{az}\sin\theta - \alpha h_{a\perp}\sin\phi - \omega\sin\theta = 0 \tag{5.21}$$

By introducing a parameter ν_0 and by removing the direct ϕ dependence, we get

$$\nu_0 = \alpha\omega \ \ cot\phi \tag{5.22}$$

$$h_{az} = \omega - (\nu_0 + k_{eff})\cos\theta \tag{5.23}$$

$$h_{a\perp} = \sqrt{(\nu_0^2 + \alpha^2\omega^2)(1 - \cos^2\theta)} \tag{5.24}$$

Eq.(5.23) and eq.(5.24) are the analytical equations that determine the behavior for the uniform single phase. This equations gives the values of applied field needed to obtain a certain stable mode given by a particular set of (θ, ϕ).

5.1.1 P-modes

The fixed points or the stable modes of a system are characterized by a set of (θ, ϕ) given by equations eq.(5.23) and eq.(5.24). These fixed points correspond to a magnetization mode in which the magnetization precesses about the symmetry axis (z-axis) in synchronization with the external field. In other words, these fixed points correspond to *periodic time-harmonic solutions* of the LLG equation. These rotating modes are termed as **P**-modes.

The analytical solution for the **P**-modes in the single phase uniform media can be determined as follows. By removing the dependence on ϕ from eq.(5.23), i.e. by substituting the value of ν_0 in eq.(5.24), we get the following

$$\frac{h_{a\perp}^2}{\sin^2\theta} - \left(\frac{h_{az} - \omega}{\cos\theta} + k_{eff}\right)^2 = \alpha^2\omega^2 \tag{5.25}$$

The eq. (5.25) allow us to plot field conditions, i.e. for given parameters α, ω, k_{eff} and variable $\cos\theta$, we can define one parabolic line in $(h_{az}, h_{a\perp})$ plane. This line identify the field condition that will produce a **P**-mode with desired value of $\cos\theta$. Fig.5.4 represents the field lines for the system of hard magnetic phase with the parameters: $\alpha = 0.1$, $k_{eff} = 0.492$ and the in-plane field frequency of $f = 6\ GHz$.

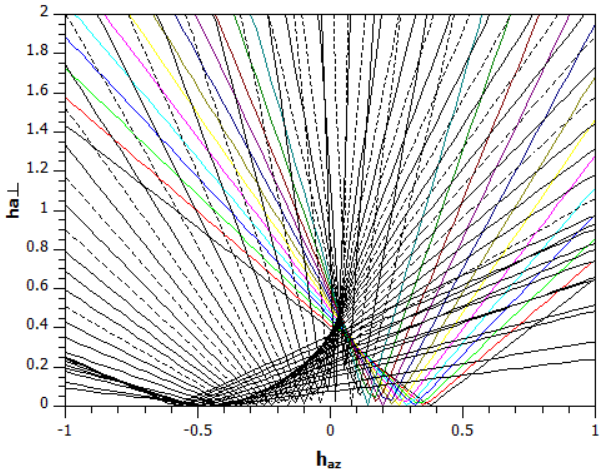

Figure 5.4: Lines for field condition that will produce **P**-mode with desired value of $\cos\theta$. This field lines are calculated for a magnetic system with parameters: $\alpha = 0.1$, $k_{eff} = 0.492$ and the in-plane field frequency of $f = 6\ GHz$. Different colored, broken line represent different values of $\cos\theta$.

We can see that two or four hyperbolic line can pass through a particular point in the figure. It means that there can be two or four **P**-modes associated with a given field condition. Indeed eq. (5.25) can be transformed into a 4th order quartic equation:

$$(1+\Omega^2)m_z^4 - 2b_z m_z^3 + (b_\perp^2 + b_z^2 - (1+\Omega^2))m_z^2 + 2b_z m_z - b_z^2 = 0 \tag{5.26}$$

where,

$$\Omega = \frac{\alpha\omega}{k_{eff}},\ \ b_z = \frac{\omega h_{az}}{k_{eff}},\ \ b_\perp = \frac{h_{a\perp}}{k_{eff}}$$

As can be seen, (5.26) is a fourth-order polynomial equation in m_z, which gives at the most four real roots in the interval $-1 \leq m_z \leq 1$. Therefore, LLG dynamics under rotating field will have at least two stable solutions. Which can be of node-type or focus-type. Therefore, two stable configurations are possible: (i) two nodes or foci; (ii) three nodes or foci plus one saddle [82].
In order to be physically realizable, a **P**-mode must be a stable node of the magnetization dynamics in the rotating frame. When no P-mode is stable, there will exist (at least) one attracting limit cycle of the above dynamics (Poincare Bendixson theorem) [83]. In the rotating frame of reference, a limit cycle represents a periodic magnetization motion along a closed path on the unit sphere. In the laboratory frame, the periodic motion along the limit cycle has to be combined with the rotation of the reference frame and this results in a quasi-periodic magnetization mode or **Q**-mode.

We solve the dynamical equation numerically for single phase magnetic systems. We have developed a code in Fortran based on *finite difference method* to solve the LLG equation (see Appendix). Using this code, we test the stability of the hard phase system and hence test the working of our code. We test the working of the code by comparing the results obtained from the numerical solutions to the results obtained from the analytical time-harmonic solutions [84].

For testing the numerical code, several random initial conditions of magnetization are used. We run the code, for several initial condition and observe that after some period of time, a stable solution is reached. Fig.5.5 shows the numerical solutions for a magnetic system with the following parameters:

- $M_s = 8 \times 10^5\ A/m$,
- $\alpha = 0.01$,
- $H_{az} = 1.1Ms$,
- $H_{a\perp} = 1 \times 10^{-4} Ms$
- $\omega = 0.103\gamma M_s = 1.82 \times 10^{10} Hz$.
- The anisotropy constant, $K = 6 \times 10^5\ Jm^{-3}$.

In the fig.5.5, the figure on the right shows the variation of the in-plane component of magnetization $m_\perp$ versus number of period. The graph plots several initial states of the system at period=0 and as the number of period increases, the system reaches a stable solution. Similar variation is also plotted for m_z. From the numerical solutions we find that the stable solutions are $m_\perp = 0.0686$ and $m_z = 0.9978$. For the single magnetic phase system, the analytical solutions already exists and we plot the analytically calculated P-mode in the same figures. We observe that the numerical solution is in good agreement with the analytical solution.

The dynamical stability of the **P**-mode can be studied analytically by perturbing the **P**-mode solution. We limit the discussion to spatially uniform perturbations. Under this condition, a given **P**-mode will be dynamically stable if the corresponding fixed point of

the magnetization dynamics in rotating frame is stable. **P**-mode stability can be studied by linearizing eq. (5.6) around the **P**-mode solution. Let $\mathbf{m}_0$ be the **P**-mode magnetization and let the perturbed mode be $\mathbf{m}(t) = \mathbf{m}_0 + \delta\mathbf{m}(t)$ ($|\delta\mathbf{m}(t)| \ll 1$). Substituting this in the eq. (5.6) and linearizing it and by computing the trace and the determinant of the resulting stability matrix A_0 [78] given as:

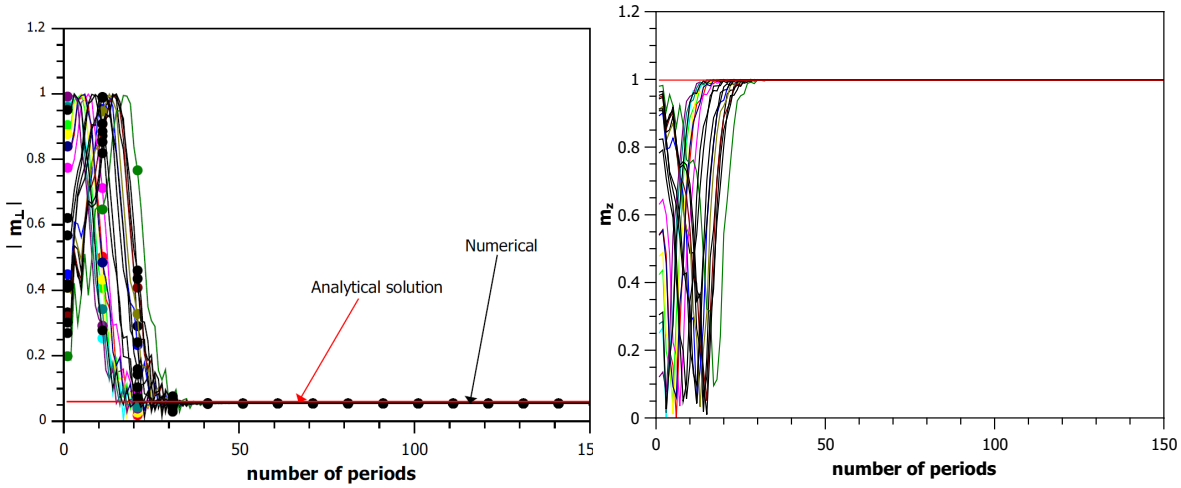

Figure 5.5: Numerical solutions for hard phase, on the left shows the variation of $\mathbf{m}_\perp$, and on the right is the variation of m_z for several initial conditions going towards stable solution. Time evolution starting from t=0; values of parameter: $M_s = 8 \times 10^5\ A/m$, $\alpha = 0.01$, $H_{az} = 1.1Ms$, $H_{a\perp} = 1 \times 10^{-4}Ms$, $\omega = 0.103\gamma M_s = 1.82 \times 10^{10}Hz$. The red horizontal line represents the P-mode obtained from analytical solution.

$$A_0 = \frac{1}{1+\alpha^2}\begin{pmatrix} 1 & -\alpha \\ \alpha & 1 \end{pmatrix}\begin{pmatrix} -\alpha\omega\cos\theta_0 & \nu_0 \\ \nu_0 - k_{eff}\sin^2\theta_0 & \nu_0 + \alpha^2\omega^2\cos^2\theta_0 \end{pmatrix} \tag{5.27}$$

the (θ_0, ν_0) represents a particular **P**-mode. The stability is controlled by the eigen value of the matrix A_0, expressed in terms of determinant and trace.

$$det\ \ A_0 = \frac{1}{1+\alpha^2}\left(\nu_0^2 - k_{eff}\sin^2\theta_0\nu_0 + \alpha^2\omega^2\cos^2\theta_0\right) \tag{5.28}$$

$$tr\ \ A_0 = -\frac{2\alpha}{1+\alpha^2}\left(\nu_0 - \frac{k_{eff}\sin^2\theta_0}{2} + \omega\cos\theta_0\right) \tag{5.29}$$

And the characteristics frequency ω_0^2 =det A_0 -$(tr\ A_0)^2/4$ is :

$$\omega_0^2 = \frac{1}{(1+\alpha^2)^2}\left[\left(\nu_0 - \frac{k_{eff}\sin^2\theta_0}{2} + \alpha^2\omega\cos\theta_0\right)^2 - (1+\alpha^2)\frac{k_{eff}^2\sin^4\theta_0}{4}\right] \tag{5.30}$$

Thus the **P**-mode stability can be given as :

- det $A_0 < 0$, saddle type fixed point
- det $A_0 > 0$ and $\omega^2 < 0$, Node-type fixed point
  tr $A_0 < 0$, stable node
  tr $A_0 > 0$, unstable node

- det $A_0 > 0$ and $\omega^2 > 0$, Focus-type fixed point
  tr $A_0 < 0$, stable focus
  tr $A_0 > 0$, unstable focus.

A **P**-mode solution exist only when det $A_0 > 0$ and tr $A_0 < 0$. The details using phase diagrams are given in the following section.

Now we try to understand the phenomena of reversal in the single magnetic phase system by using phase diagrams. The phase diagram in our system is plotted between in-plane component of the applied field $h_{a\perp}$ and the DC field h_{az}. To study the reversal phenomena we take two examples, a hard magnetic system subjected to microwave field of frequency 6 GHz and the other subjected to a frequency of 10 GHz.

5.1.2 Phase diagrams for magnetic reversal

We studied the reversal dynamics in presence of microwave field for single phase magnetic system. Using our Fortran code we perform the numerical simulation for the hard magnetic phase.

As already mentioned, the system is infinite thick system which means that in such systems the propagation field leads the magnetization reversal and coincides with the coercive field. This field is called as switching field because at this field the complete reversal of the system takes place. For numerical simulations, the infinite thickness means that the thickness of the system should be few tens of its domain wall length ($l_w = \sqrt{\frac{A}{K}}$) of the system.

The numerical simulations are performed for the initial magnetization state $\mathbf{m} = (0, 0, -1)$, and the in-plane applied field $\mathbf{h}_{a\perp}$ is kept constant. The DC field, h_{az}, is varied from $-M_s$ to M_s.
We obtain a m_z versus h_{az} magnetization loop in absence of the applied in-plane circularly polarized magnetized field, $h_{a\perp}$, as shown in fig.5.6. The hard magnetic system is represented by $k_{eff} > 0$. We find that the switching field in absence of the microwave field is found to be $h_{sw} = 0.8$.

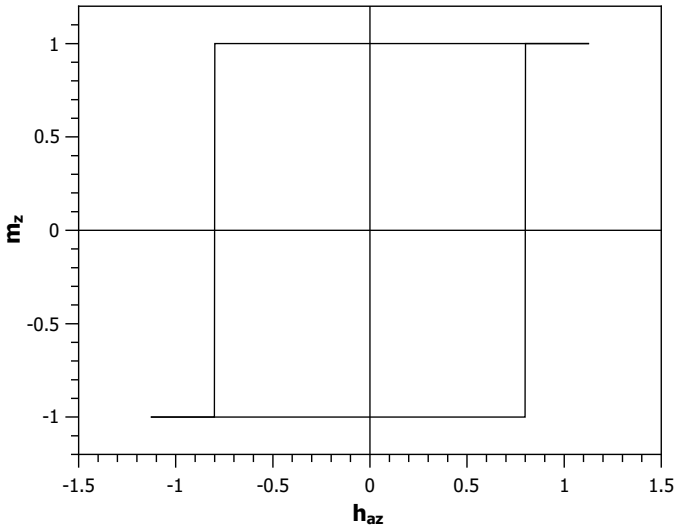

Figure 5.6: Representation of m_z in absence of $h_{a\perp}$.

On subjecting the system to the rotating magnetic field and keeping the other parameters, the same (as used for previous calculation), the magnetization behavior is plotted in fig.fig. 5.7. The parameters used for the simulation are defined below:

- total thickness is $z = 200nm$
- α(damping constant)$= 0.01$
- $k_{eff}(hard) = 0.4921$
- $k_{eff}(soft) = -1$
- $h_{a\perp} = 0.1$
- $\omega = -0.2142$, $f = 6GHz$, the negative sign is used since the frequency is applied in the anti-clockwise direction with respect to the frame.
- h_{az} varies from -1.125 to 1.125

Solving the dynamic equation numerically, for uniform hard phase $K = 6 \times 10^5 Jm^{-3}$) and soft phase, the resulting magnetization curve is represented in fig.5.7.

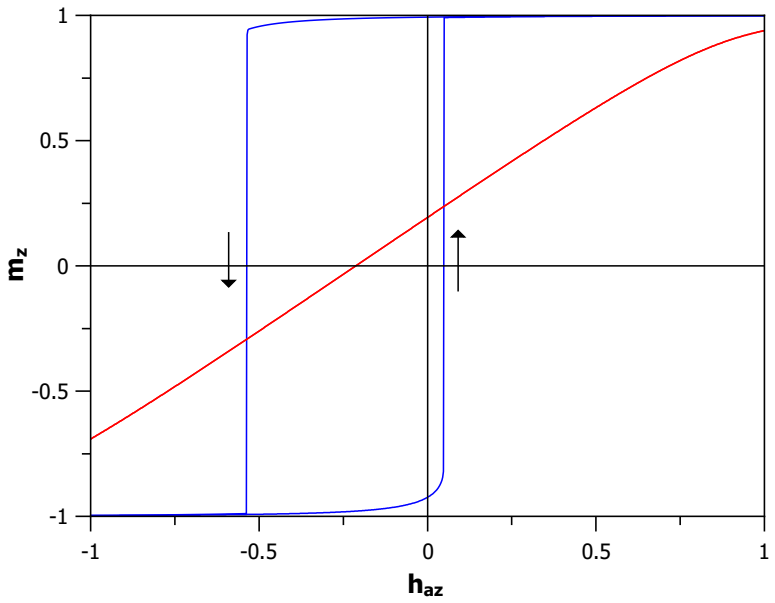

Figure 5.7: Spatial average of m_z vs h_{az} is shown, for hard (in blue)and soft (in red) phases for the microwave field frequency of 6 GHz.

We can see in the figure that the hard phase (shown in blue) and the soft phase (in red), shows an asymmetric behavior on the horizontal axis. This is due to the presence of in-plane rotating field which is responsible for breaking the symmetry of the system. The switching field for hard magnetic system is reduced to $h_{sw} = 0.05$, i.e. 42.6 kAm^{-1}.

We can explain the details of the switching using a phase diagram i.e. diagram is plotted in the control plane $(h_{az}, h_{a\perp})$, assuming that the microwave frequency ω is given and fixed. The diagram is invariant with respect to changes in k_{eff} when it is represented in terms of h_{az}/k_{eff}, $h_{a\perp}/k_{eff}$, and ω/k_{eff}.

The hard phase response is analyzed when the field h_{az} is slowly varied between opposite large values. The phase diagram for hard magnetic system subjected to microwave field of 6 GHz is shown in fig.5.8. The condition of constant $h_{a\perp}$ and slowly varying h_{az} is represented by the horizontal line in the $(h_{az}, h_{a\perp})$- plane Fig.5.8. The points A and B,

where the line crosses the bifurcation lines, are the possible switching points where the system may jump from one **P**-mode to another or from **P**-type to **Q**-type response or vice-versa. The **P**-mode in the system are characterized by different values of magnetization component $m_z = \cos\theta$, as a function of h_{az}. The field history determines which m_z state is realized under given h_{az}. The first switching occurs at point B, where the system becomes unstable due to saddle-node bifurcation. Switching results in the sudden m_z jump from negative to positive value as shown.

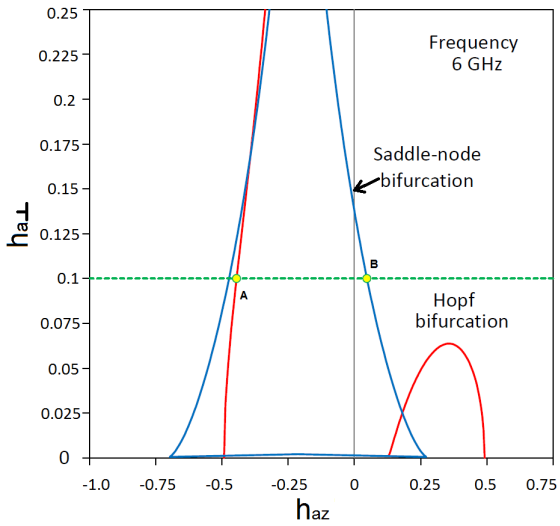

Figure 5.8: Phase diagram for hard phase at 6GHz.

This saddle node bifurcation is expressed for our system by the equation det $A_0 = 0$. The blue line in the fig. 5.8 representing saddle node are traced making eq. (5.28) equal to zero.

The second switching in this system occurs at point A, because of Hopf-bifurcation. The systems jumps back from positive to negative value, i.e. when a nonsaddle fixed point is changed from stable to unstable or vice versa. In our system, the bifurcation condition is given by tr $A_0 = 0$ and det $A_0 > 0$. The red line in fig. 5.8 representing the Hopf bifurcation is traced by equation eq. (5.29) to zero for the condition that eq. (5.28) is > 0.

The theoretical limit of the coercivity field according to magnetic consideration by Brown [85] and Aharoni [86], is given by $H_c = 2K/M_s - NM_s$. For the hard phase, using our parameters, the coercivity is calculated to be $H_c = 394\ \ kA/m$; $h_c = 0.49$. This coercivity value is also called *Stoner-Wohlfarth field*. It is the value obtained when the system is exposed to an applied field anti-parallel to magnetization $\mathbf{M}_s$.

Taking another case, we apply a higher microwave frequency to hard phase system. The response of magnetization is discussed as follows. The in-plane field frequency is 10 GHz and all the other parameters are kept the same as in the previous case. The initial magnetization state is assumed to be negatively saturated to $-M_s$. The DC field h_{az} is slowly varied (at the rate of 9 A/ms).

The magnetization curve for the Hard phase is shown in fig.5.9. The switching field $H_{sw} = 383.91\ \ kA/m$ and for the negative branch is $H_{sw} = -430.19\ \ kA/m$. The disturbances when h_{az} varies from negative to positive value, can be explained with the help of phase diagram shown in fig.5.10. The points A and B indicated in fig.5.10 are the switching points. These are the points where the horizontal line (i.e. the line of constant field

$h_{a\perp}$) crosses various bifurcation lines. At these the system may jump from one **P**-mode to another or from **P** to **Q**-type modes. Irreversible jumps can occur when the stability of the system is destroyed by the action of the field. The P-modes are characterized by different values of magnetization components as a function of h_{az}, can be obtained from the equation (5.24) and (5.23). The state of the system depends on the field history of h_{az}.

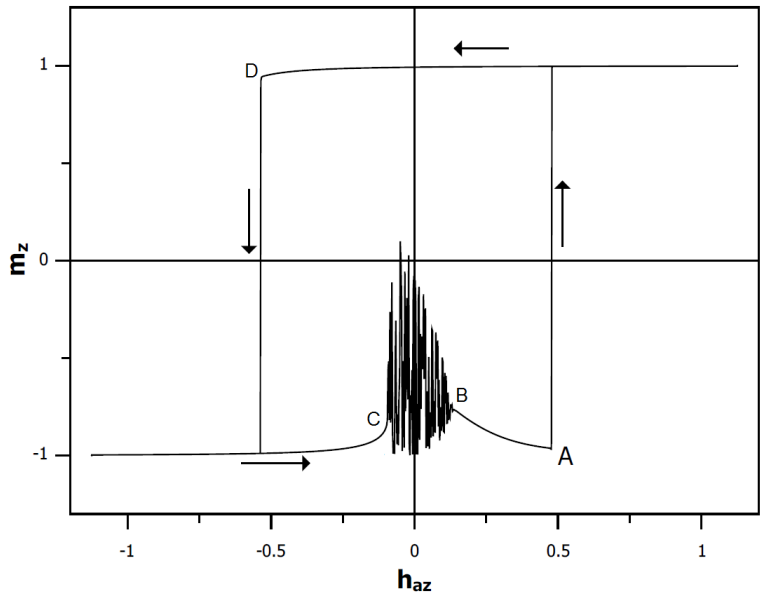

Figure 5.9: Average magnetization in z-direction for the single hard phase, with in plane circularly polarized field, $h_{a\perp}$ with a constant magnitude of $8 \times 10^4 A$ and frequency $f = 10GHz$. The arrows indicate the direction of dc field, h_{az} positive to negative and vice-versa.

When the field is increased from negative value, the situation in the system is quite complex. For increasing h_{az}, bifurcation encountered at point E and D involve the states different from the states occupied by the system. This means that the system is in a stationary state which does not encounter the situations or states denoted by points E and D while h_{az} is increased. Therefore the switching does not occur until the point C is reached. AT this point the stable state of the system is destroyed by the *saddle-node bifurcation* which is given by the condition det $A = 0$ (eq.(5.28)).

The system jumps from **P**-type to **Q**-type response, there are magnetization oscillations occurring at frequency much lower than ω between point C and B. At point B, the **Q**-mode changes **P**-mode by *Hopf-bifurcation*, control the creation or destruction of limit cycles. A limit cycle is a periodic solution, so it will represent a quasi-periodic magnetization mode, deriving from the combination of the rotating field and the limit cycle periods. The field is increased further from B to A, the quasi-periodic motion survives till point B where it is destroyed by the saddle-connection bifurcation.

Final switching occurs at point A due to second *Hopf-bifurcation* where m_z jumps from negative to positive values. The branch till point D is fully reversible, where the switching occurs and the system becomes unstable due to Hopf-bifurcation. The point E in the Fig.5.10 plays no role in this case. The lower and upper branches are not symmetric as the symmetry is broken by the rotation of the Rf field with respect to the dc field H_{az}.

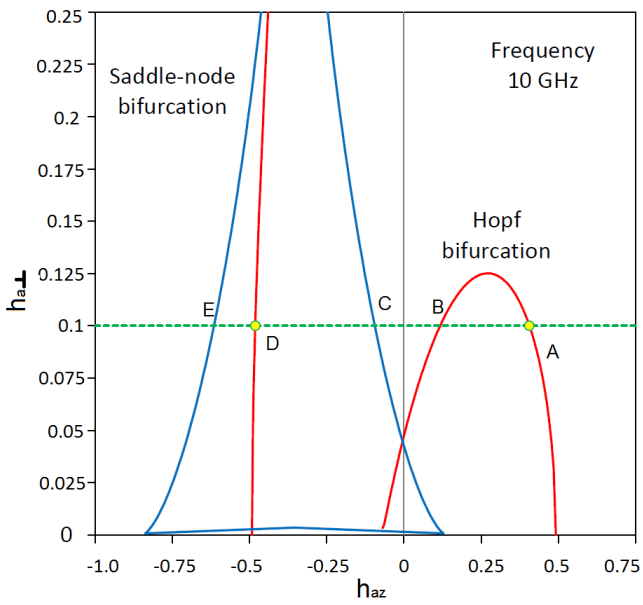

Figure 5.10: Phase diagram in (h_z, h_{xy})-plane; Hopf-bifurcation is indicated by red continuous lines, saddle-node by continuous blue lines.

The phase diagram provides an estimate for the threshold microwave field amplitude $h_{threshold}$ above which the reduction in switching field may be obtained by imposing the condition that $h_{a\perp}$ must be beyond the maximum of the Hopf-bifurcation line present in the $h_{az} < 0$ part of the phase diagram (fig. 5.10). This limit can found by considering $\cos\theta \simeq 1$ as the Hopf bifurcation is in the neighborhood of $m_z = 1 - \sin^2\theta/2$. Using this in the condition tr $A_0 = 0$ from eq. (5.29) and by inserting the resulting expression for $\sin^2\theta$ into eq. (5.24) one obtains the threshold equation,

$$h_{a\perp}^2 \simeq \frac{2}{k_{eff}+\omega}(\nu_0+\omega)(\nu_0^2+\alpha^2\alpha^2) \tag{5.31}$$

$$\frac{h_{threshold}}{k_{eff}} = \frac{h_{a\perp}}{k_{eff}} \simeq \frac{1}{\sqrt{1+\omega/k_{eff}}}\left(\frac{2\omega}{3k_{eff}}\right)^{3/2}$$

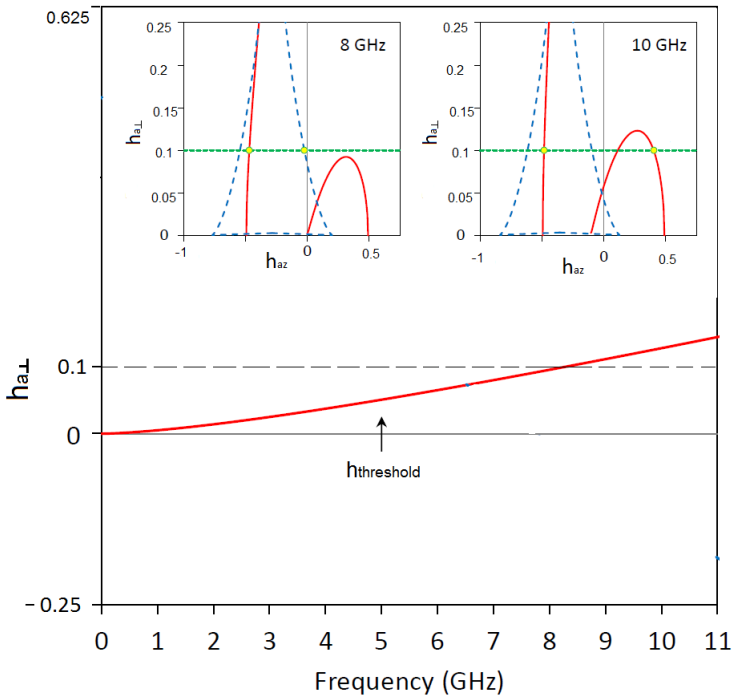

Figure 5.11: Analytical calculations for the hard phase system. Main frame: $h_{threshold}$ (red continuous line), corresponds with the maximum of the Hopf-bifurcation line (red continuous line in the insets) shown in the two insets for frequencies 8 and 10 GHz. In the two insets the saddle-node bifurcation line is represented by the dashed blue line.

The threshold line given by eq.(5.1.2) is traced for the system of hard magnetic phase as a function of frequency. It is obtained by neglecting $\alpha^2\omega^2$ term. fig. 5.11 represents the threshold in plane field above which further reduction in switching should be obtained by increasing the in-plane field above the Hopf- bifurcation line (given in inset by red curved lines). For our current system with $k_{eff} > 0$, we see that the Hopf bifurcation curve (given in inset by red lines), in the region $h_{az} > 0$ is lower up to 8 GHz frequency and then on increasing the frequency, the Hopf bifurcation curve crosses the applied in plane field line (dotted green line in the inset). In the main picture we can also see that for the frequency > 8 GHz, the threshold field also crosses the $h_{a\perp}$ line(shown in black dotted line).

Now we examine the switching behavior in hard magnetic systems as a function of microwave field frequency. Fig.5.12 shows the z-component of magnetization versus applied DC field, h_{az} as a response to microwave frequencies. From the figure, it is observed that with the increase in the microwave field frequency, the oscillations in the system increases.

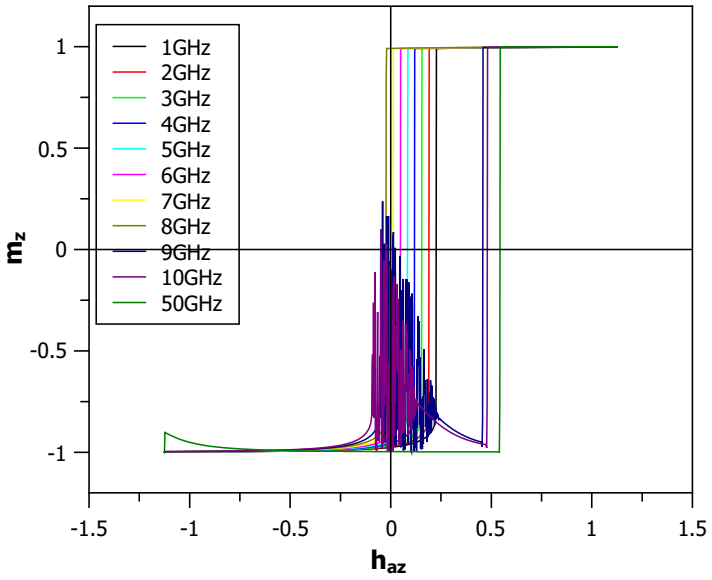

Figure 5.12: Representation of spatial average of m_z versus h_{az} under constant $h_{a\perp}$ at different frequencies. Only the branch where h_{az} is changing from negative to positive value is shown here.

As we observe in the fig.5.13, the switching field first decreases with the frequency upto $8GHz$. At frequencies greater than 8 GHz, the oscillations becomes more pronounced. For $f \geq 8GHz$, as we have already seen from phase diagram, the system jumps from **P**-type to **Q**-type response, with the appearance of oscillations. These oscillation persist until the **Q**-mode is changed to **P**-mode by Hopf-bifurcation. For the frequencies higher that 8 GHz, the switching field shows a sudden jump and is more closer to the value calculated from stoner-wohlfarth model.

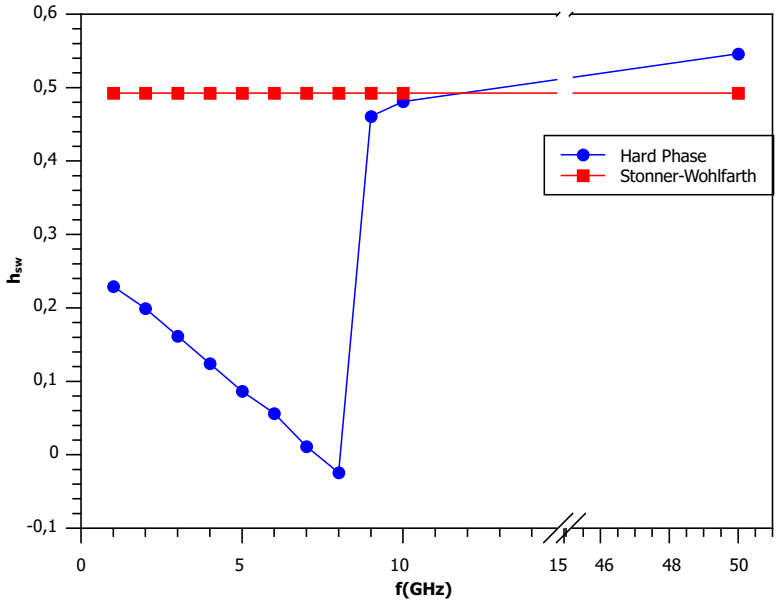

Figure 5.13: Variation of switching field as a function of frequency and its comparison to Stoner-Wohlfarth model.

Average behavior of Hard-Soft Phase Before discussing the bilayer exchange coupled system let us examine the magnetization behavior in the case when the two magnetic phases are not coupled to each other. We consider two magnetic systems i.e. hard and soft connected together at the interface but without any exchange between them. This situation is equivalent to calculating the average of the magnetization of the two systems. The magnetization response is studied under the slowly varying DC field, h_{az} and constant in-plane circular field at $f = 10\ GHz$.

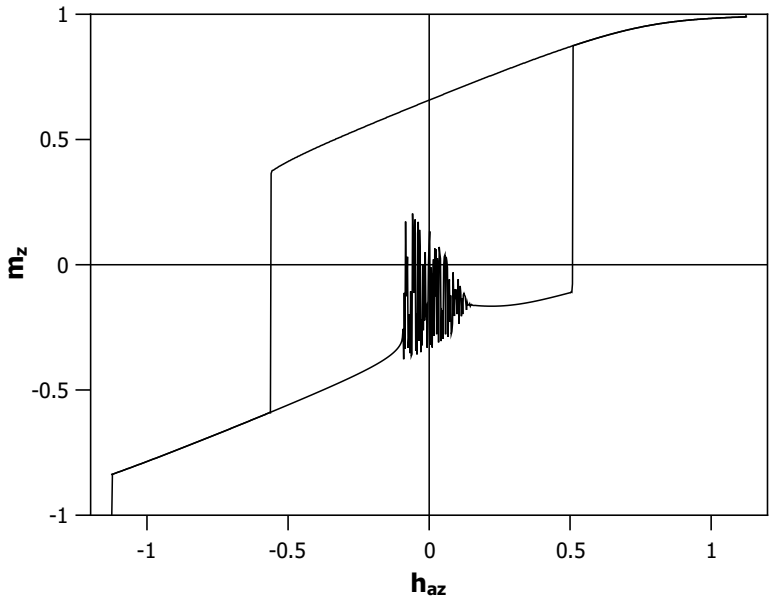

Figure 5.14: Represents the average of the z component of magentization versus H_{az} for $f = 10GHz$.

Fig.5.14 represents m_z vs h_{az}, with average of the two phases of equal thickness, under the parameters given in 5.1.2 except for frequency. We observe that the curve is not symmetric due to the presence of the microwave field and the oscillations still persists.

5.2 Exchange coupled bilayer system

Our main aim is to understand the magnetization dynamics of an exchange-spring bilayer system. There has been a lot of attention given to the research in exchange spring system in order to find the optimal condition for reduction of the switching field but finding an analytical solution has been a challenge. In order to understand the reversal process in the bilayer systems we study the LLG equation numerically in the limit of infinite thickness of the layers subjected to the microwave field.

We consider a system composed of two layers lying on the xy plane, one magnetically hard and the other soft. Both layers exhibit perpendicular uniaxial anisotropy directed along z-axis. The system is infinite in the xy plane and due to this geometry the magnetization is uniform along the plane. Therefore the magnetization vector is distributed along z-axis, given as $\mathbf{M} = \mathbf{M}(z)$ which is the local magnetization vector. Our main aim is to work out this magnetization distribution for the bilayer system. A representation of the bilayer system is shown in fig. 5.15. We define the coordinate z_0 to be the interface between the soft and the hard layer. The saturation magnetization is defined as $|\mathbf{M}(z)| = M_s(z)$.

The in-plane component of the magnetization is given by $M_\perp = \sqrt{M_x^2 + M_y^2}$. The magnetocrystalline anisotropy is $K(z) = K1$ for $z < z_0$, and $K(z) = K_2$ for $z > z_0$. The shape and magnetocrystalline anisotropies can be merged in a single effective anisotropy constant, $K_{eff}(z) = K(z) - \mu_0 M_s^2(z)/2$. Due to this geometry of the system, surface and interface anisotropies are neglected. The two media (hard and soft phases) are exchange-coupled on a nanometric scale.

The normalized parameters are defined in a similar manner as defined for the single phase system. Magnetization unit vector $\mathbf{m} = \mathbf{M}/M_s$ and $k_{eff} = K_{eff}/2\mu_0 M_s^2$.

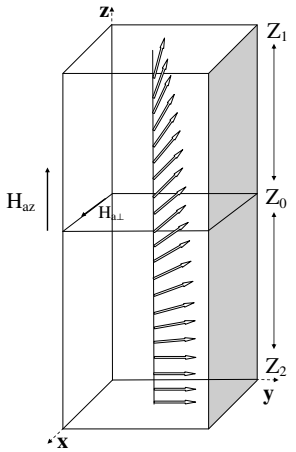

Figure 5.15: Basic model for of hard/soft bilayer with perpendicular (z-axis) anisotropy axis.

The magnetization reversal phenomena have been studied by Asti et al. using a 1D micromagnetic model for the bilayer system under static case. They studied and found analytical expression for the propagation field given by eq.(5.32) for the perpendicular exchange spring media. They showed that the coercivity field and the propagation field coincide in the limit of infinite thickness of the layers. In the limit of infinite thick systems, the demagnetization process starts from the soft phase, which undergoes a uniform reversible rotation until the irreversible switching of the hard phase occurs, in a way similar to a sudden penetration of a pinned domain wall.

$$h_P = \frac{2k_{eff(soft)}}{\mu_0 M_s^2}\left[1 - \sqrt{1 - \frac{k_{eff(hard)}}{K_{eff(soft)}}}\right] \tag{5.32}$$

Eq.(5.32) calculates the propagation field for the bilayer system in the limit of infinite thickness of the layers but does not consider the influence of the additional in-plane applied circularly polarized field. Here onwards we shall use subscript 1 to describe the parameters of the soft phase and 2 for the hard phase.

The magnetization dynamics are given by LLG equation eq. (5.6), and the applied field is given by eq. (5.7). The energy of the system is given by $\mathbf{g}_L$ defined as follows,

$$\mathbf{g}_L(\mathbf{m}, \mathbf{h}_a) = \frac{G_L(\mathbf{M}, \mathbf{H}_a)}{\mu_0 M_s^2 V} \tag{5.33}$$
$$= -\frac{1}{V}\int_V \left[\frac{l_{ex}^2}{2}(|\nabla \mathbf{m}|)^2 - \mathbf{h}_a \cdot \mathbf{m} - \frac{1}{2}k_{eff} m_z^2\right] dV$$

where $l_{ex} = \sqrt{\frac{2A}{\mu_0 M_s^2}}$ is the exchange length of the system. It is also useful to express the length in terms of normalized units for which we now denote the normalized position as $\mathbf{r}/l_{ex}$.

$$\mathbf{g}_L(\mathbf{m}; \mathbf{h}_a) = -\frac{1}{V}\int_V \left[\frac{1}{2}|\nabla \mathbf{m}|^2 - \mathbf{h}_a \cdot \mathbf{m} - \frac{1}{2}k_{eff} m_z^2\right] dV \tag{5.34}$$

where ∇ represents the gradient with respect to normalized position $\mathbf{r}/l_{ex}$. The effective field of the system $h_{eff} = -\partial \mathbf{g}_L/\partial \mathbf{m}$ is given by:

$$\mathbf{h}_{eff} = \nabla^2 \mathbf{m} + k_{eff} m_z \mathbf{e}_z + \mathbf{h}_a \tag{5.35}$$

The analytical solution of the LLG equation now become very complicated due to the exchange energy term. Using spherical coordinates, where magnetization is defined by eq. (5.10), for the system of bilayer system, the exchange term is defined by,

$$\nabla \mathbf{m} = \left(\frac{\partial^2 \theta}{\partial z^2} - \sin\theta\cos\theta\left(\frac{\partial \phi}{\partial z}\right)^2\right)\mathbf{e}_\theta + \left(\sin\theta\frac{\partial^2 \phi}{\partial z^2} + 2\cos\frac{\partial \theta}{\partial z}\frac{\partial \phi}{\partial z}\right)\mathbf{e}_\phi \tag{5.36}$$

Using eq. (5.36) and substituting in $\mathbf{h}_{eff}$ term given by eq. (5.35) and projecting the LLG equation along ϕ and θ and putting $d\theta/dt = d\phi/dt = 0$, we get,

$$\sin\theta\frac{\partial^2 \phi}{\partial z^2} + 2\cos\frac{\partial \phi}{\partial z}\frac{\partial \theta}{\partial z} = h_{a\perp}\sin\theta + \alpha\omega\sin\theta \tag{5.37}$$

$$\frac{\partial^2 \theta}{\partial z^2} - \sin\theta\cos\theta\left(\frac{\partial \phi}{\partial z}\right)^2 = (k_{eff}\cos\theta + h_{az})\sin\theta - h_{a\perp}\cos\theta\sin\phi - \omega\sin\theta \tag{5.38}$$

An analytical solution for these equation has not been found yet. Thus we study the bilayer system using the numerical solutions of LLG equation. For numerical solutions we use our Fortran code based on the finite difference method.

We solve the equation of motion for the bilayer system using the micromagnetic parameters of a widely used exchange spring system, FePt/Fe system. The following parameters are used for the simulation: exchange constant the exchange stiffness constant is taken to be $A = 10^{-11} Jm^{-1}$. Here we focus our attention on an infinite thick system where the propagation field leads the reversal process. The infinite thickness limit is easily reached when the total width of the system is few tens of its domain wall length, l_w. For our calculation we assume the total thickness to be 200 nm, each phase being 100 nm thick. Other parameters are as given below:

- α(damping constant)= 0.01
- $K(hard) = 2\ MJ/m$
- $K(soft) = 0.048\ MJ/m$

- $M_s = 1.55\ MA/m$ (this overestimates M_s for hard layer but allows a simpler analytical formulation in terms of reduced units)
- $H_{a\perp} = 0.08\ MA/m$
- $z = 200$, thickness of the system.
- $f = 6\ GHz$

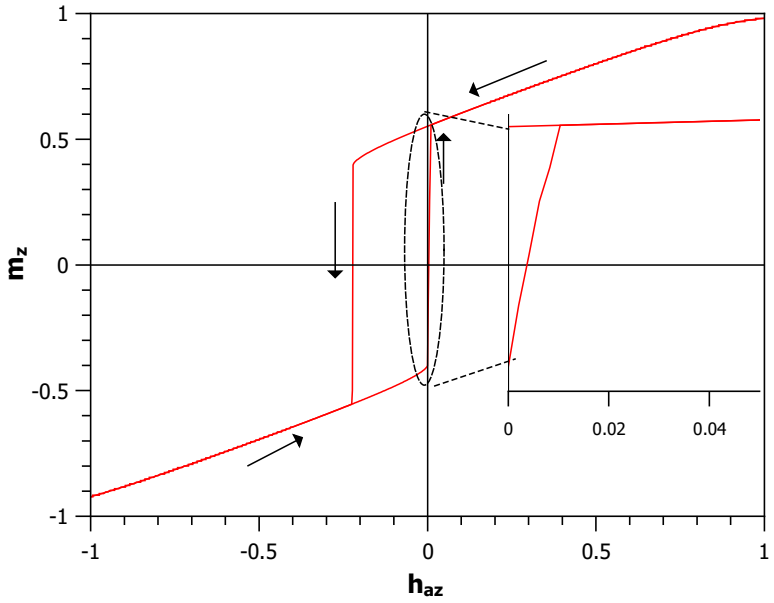

Figure 5.16: Average magnetization of the z component for non-uniform bilayer system for 6 GHz frequency of the in-plane applied field.

In the fig.5.16, the average of magnetization is shown for the bilayer system subjected to microwave field of frequency 6 GHz. The average of the magnetization is taken along z, $< m_z >$ behaves like a P-mode. Due to non-uniform magnetization in the bilayer system, the stable solution is given by the average magnetization $< m_z >$, which is constant in time forming an angle θ with respect to z axis whereas $< m_{\perp >}$ is rotating with angular frequency ω and with a phase lag ϕ with respect to the rotating component of the applied field $h_{a\perp}$. We call this stationary state a global P-mode.

A plot of the $m_\perp$ and h_{az} gives very similar results. The switching occurs at $h_{az} = 0.01$ ($H_{az} = 15kA/m$). From the figure, we see that the magnetization of the soft phase changes rapidly and more as compared to the magnetization of the hard phase. The hard phase is still closer to the initial magnetization state.

The arrows in the figure represent the direction of the variation of the applied field. Initially the system is assumed to be in the negative saturated state, with $\mathbf{m} = (0, 0, -1)$. The arrows showing the forward branch of the loop, i.e. when h_{az} is varied from -1.03 to $+1.03$ and similarly the reverse branch is when h_{az} varies from $+1.03$ to -1.03, are also indicated. We notice that the switching field has reduced and the plot is asymmetric due to the presence of the microwave field. Another very interesting point worth noting is that the curve is switching at a very small positive DC field. This result opens a possibility to investigate the zero directional field microwave assisted switching.
We perform simulation to investigate the possibility of zero field switching. For the numerical simulation we start with the global state of the system just before switching and

the DC field is not applied. However we still apply the constant microwave field. We let the system exposed to this condition and the we observe that indeed the system switches in absence of the DC field. This phenomena is shown in fig.5.17. The system goes to the fully switched state represented by $m_z \approx 0.6$. The x-axis of the curve represents an arbitrary time period.

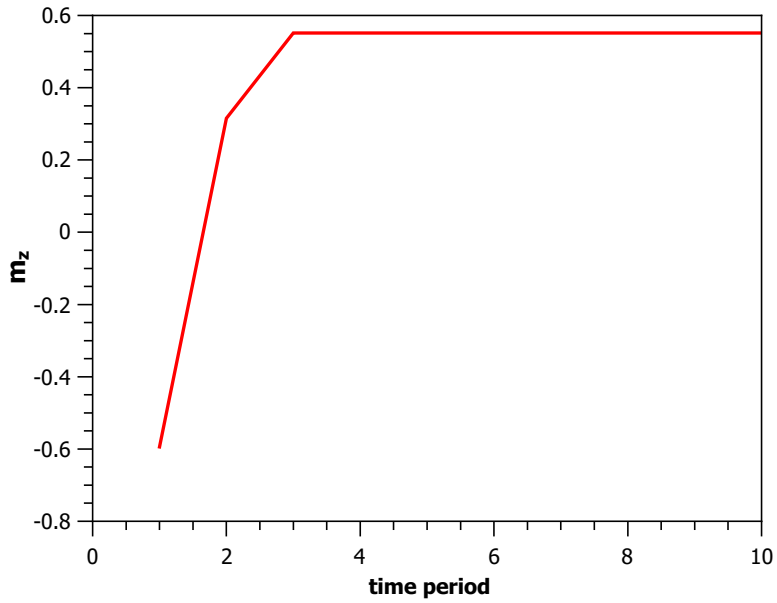

Figure 5.17: The system showing zero field switching. The system is initially in the condition just before the switching and the DC field is switched off but the microwave field is still applied.

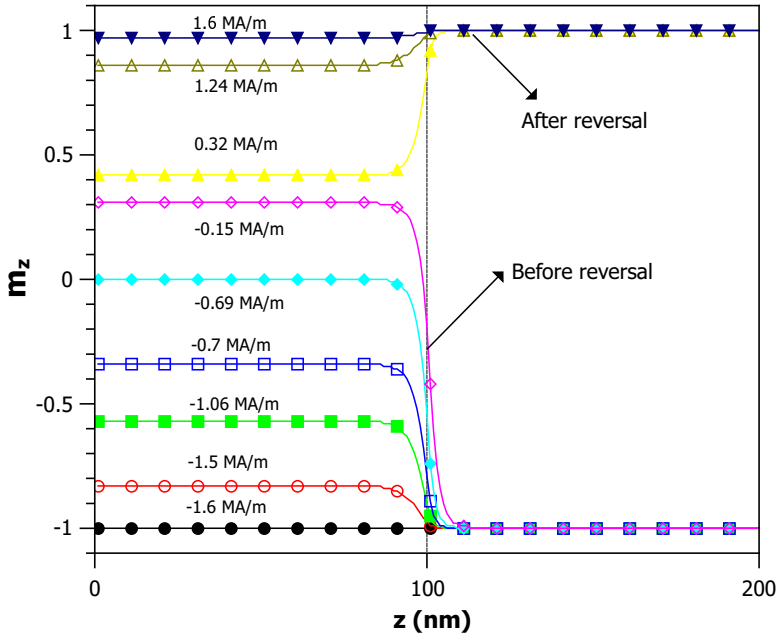

Figure 5.18: Spatial profile of m_z before the switching of the system at different values of h_{az}. From $z = 1 - 100$ represents the *soft phase* and $z = 101 - 200$ is the *hard phase*.

A deeper analysis of the simulation results gives us the opportunity to go beyond the

global P-mode concept. We also investigated the variation of magnetization over the space. Fig.5.18 shows the magnetization component m_z and h_{az} as a function of z for different values of h_{az}. The figure shows two uniform regions separated by a thin transition region. The thickness of the transition region remains constant (30 nm) all along the magnetization curve and its contribution to the average magnetization can be assumed to be negligible.

In the figure, for the profile after switching of the system we find that the hard phase, $100 < z \leq 200$ has switched its state from negative saturation to positive while the soft phase approaches to positive saturation value slowly. The uniform region for $z \leq 100$, as observed from the figure is not completely saturated. This is because the shape anisotropy of the system makes the soft phase magnetization to align in the plane of the system. Similar spatial profile is obtained for $m_\perp$ vs h_{az} plot. Thus we can say that the global P-mode is nothing but the average of two individual P-modes, corresponding respectively to the soft and the hard layer.

On the basis of this observation, we can divide the bilayer system into 3 regions based on their magnetic behavior; the hard phase region, the transition region and the soft phase region. The bilayer system away from the transition region, i.e. in the hard phase and the soft phase regions, can be seen as two uniformly magnetized region with magnetization rotating in-plane with the period of the AC field (i.e. like two **P**-modes).

We also studied the spatial magnetization distributions for different frequencies and found that the same pattern is followed. For instance if we look at the width of the region where the transition between the hard and soft happens in the system, we find that the width remains almost constant, as shown in table.5.1.

Frequency f (GHz)	Width of transition region (nm)
6	30
8	30
15	30

Table 5.1: Width of the transition region at different frequencies of the in-plane applied field.

For the current bilayer system, since we observe the two **P**-modes in the hard and soft regions, we can analytically check if these **P**-modes correspond to the analytical solutions of single hard and soft phase systems. We calculated the theoretical values of the applied field for the single phase system, form the eq.(5.24) and eq.(5.23) needed to obtain the same values of the magnetization state in the bilayer system. But the **P**-modes of the bilayer system are found to be different from those of the single phase systems studied in the section 5.1.

Treating the bilayer system as two **P**-mode solutions, we can simplify the analytical approach using the numerical solutions. We find that these 2 P-modes can not be generated by the fields given by eq. (5.24) and eq. (5.23) in the case of single phase system. Hence we develop a hypothesis that the observed **P**-modes, in the bilayer system are generated by the field denoted by $\mathbf{h}_i$ (i=1,2; for soft and hard phase respectively). This field is the sum of the applied field (calculated from the analytical expressions) and an additional interaction field, $\mathbf{h}_{exc,j}$ $(j = 1, 2 \neq i)$ which represents the exchange coupling with the other magnetic phase.

The field, $\mathbf{h}_i$ is described as

$$\mathbf{h}_i = \begin{pmatrix} h_{a\perp} \\ 0 \\ h_{az} \end{pmatrix} + C \begin{pmatrix} sin\theta_j \ cos\phi_j \\ sin\theta_j \ sin\phi_j \\ cos\theta_j \end{pmatrix} \tag{5.39}$$

where C is a constant which needs to be determined. We used the standard *ansatz* for the exchange field $h_{exc,j} = C\mathbf{m}_j$. The exchange energy corresponding to this field is given by $-\mu_0 C\mathbf{m}_1 \cdot \mathbf{m}_2$.

This field is subtracted from the field actually applied for the bilayer system, $\mathbf{h}_a$. This difference in the field is calculated as follows,

$$\begin{pmatrix} h_{a\perp(bilayer)} \\ 0 \\ h_{az(bilayer)} \end{pmatrix} = \begin{pmatrix} h_{a\perp} + Cm_{xj} \\ Cm_{yj} \\ h_{az} + Cm_{zj} \end{pmatrix} \tag{5.40}$$

$$\begin{pmatrix} h_{a\perp(bilayer)} - h_{a\perp} \\ 0 \\ h_{az(bilayer)} - h_{az} \end{pmatrix} = C \begin{pmatrix} m_{xj} \\ m_{yj} \\ m_{zj} \end{pmatrix} \tag{5.41}$$

The equation has 4 unknowns, specifically 3 components of $\mathbf{h}_i$ and C. They are determined by using eq.(5.23) and eq.(5.24) and by using the constraint $|\mathbf{m}| = 1$, we can write eq.(5.41) as:

$$\sqrt{(h_{a\perp(bilayer)} - h_{a\perp})^2 + (h_{az(bilayer)} - h_{az})^2} = C|\mathbf{m}| = C \tag{5.42}$$

Using the numerical data, we found the value of C to be 0.1. The calculated magnitude of the difference of applied fields , i.e. $\Delta H = \sqrt{(h_{a\perp(bilayer)} - h_{a\perp})^2 + (h_{az(bilayer)} - h_{az})^2}$ with respect to the applied DC field is demonstrated in fig. 5.19. We can see that the behavior of ΔH is linear and symmetric with respect to the applied DC field, h_{az}.

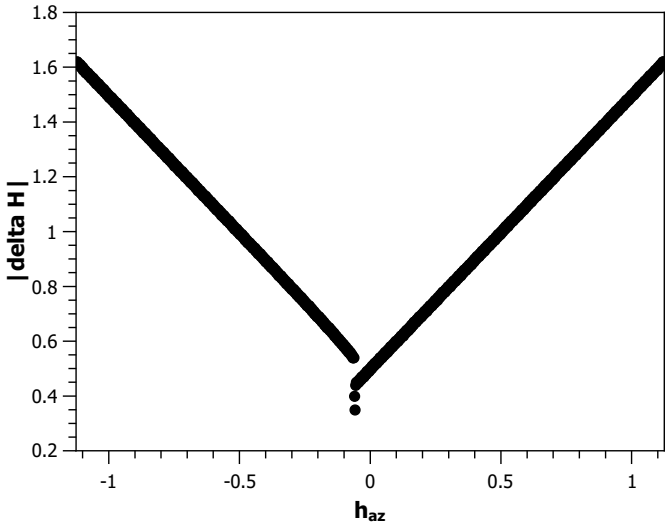

Figure 5.19: The delta H variation with respect to the applied DC field.

Using the numerical data, we have also calculated the exchange energy of the bilayer system fig.5.20. The exchange energy term is calculated by integrating $(\nabla\mathbf{m})^2$ along the sample thickness. This integration includes the transition region which will give the main contribution to the total exchange energy of the system. Numerical values of (m_x, m_y, m_z)

are used to calculate, ∇m_x, ∇m_y and ∇m_z. The figure plots the exchange energy versus the angle between the magnetization of the two system at the extremities of the bilayer system, i.e. soft and hard phase respectively. Finally the exchange energy integral over dz, (not the volume integral as we not consider x, and y variation in the model.) is calculated using trapezoidal rule as follows:

The exchange energy of the system:

$$\int \frac{1}{2}(\nabla \mathbf{m})^2 dz = \int \frac{1}{2}((\nabla m_x)^2 + (\nabla m_y)^2 + (\nabla m_z)^2) dz$$

where,

$$\nabla m_i = \frac{dm_i}{dz} = \frac{m_i(z+\triangle z) - m_i(z)}{\triangle z} \tag{5.43}$$

The integration is carried out using trapezoidal rule as follows:
For N equally spaced points, or for points from $(1, 2, \ldots, N+1)$ with the spacing $h = (b-a)/N$, then

$$\int_a^b f(x)dx \approx \frac{h}{2}\sum_{k=1}^{N}(f(x_{k+1} + f(x_k))) = \frac{b-a}{2N}(f(x_1 + 2(f(x_2 + \ldots + f(x_N)) + f(x_{N+1})))) \tag{5.44}$$

Thus for our case, $a = 1$,$b = 200$, and $N = 199$, thus, $h = 1$,

$$\int_1^{200} (\nabla \mathbf{m})^2 dz = \frac{1}{2}\left((\nabla \mathbf{m})^2(1) + 2\left((\nabla \mathbf{m})^2(2) + \ldots + (\nabla \mathbf{m})^2(199)\right) + (\nabla \mathbf{m})^2(200)\right) \tag{5.45}$$

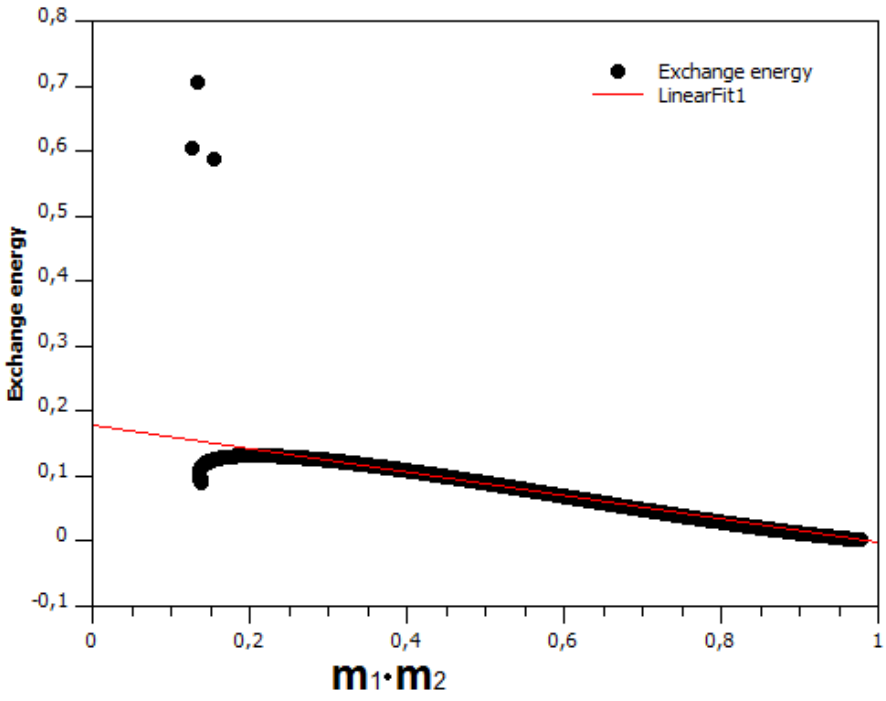

Figure 5.20: The exchange energy vs the cosine of the angle between the magnetization of the extremities of two layers, i.e. the hard and soft phase magnetization.

From the slope of the curve one can obtain an estimate of the coupling constant, C. *By linearly fitting the data, the coupling constant is found to be* $C = 0.1$. It is found to be the same value as our earlier estimated value. The points in the figure that do not fit the linear behavior are the points correspond to those values of h_{az} around the field where switching occurs.

5.2.1 Macrospin theory

Our conclusion from the numerical results for the bilayer system also offers us to have another point of view towards such kind of systems. This approach is equivalent to describe the system as two exchange coupled macrospins with different uniaxial anisotropy. The two spins can be assumed to have two different anisotropy constant, one representing the hard phase and the other, the soft phase. The interaction of the two spins is assumed to be due to the coupling energy of the type: $J(1 - \mathbf{m}_1 \cdot \mathbf{m}_2)$. J is the exchange constant and m_1 and m_2 are two spins.

The macrospin model is numerically solved under the same parametric conditions used for the bilayer system with the exchange constant derived from the solutions of bilayer system. We consider two spins having same saturation magnetization but different anisotropy constants, k_1 and k_2, where the contants are defined similar to the bilayer systems. We assume that both the spins are subjected to a DC field, h_{az} which is varied slowly from $-M_s \leq h_{az} \geq +M_s$. A constant in-plane microwave field $\mathbf{h}_{a\perp}$ is applied at a frequency of 6 GHz. The following parameters are used:

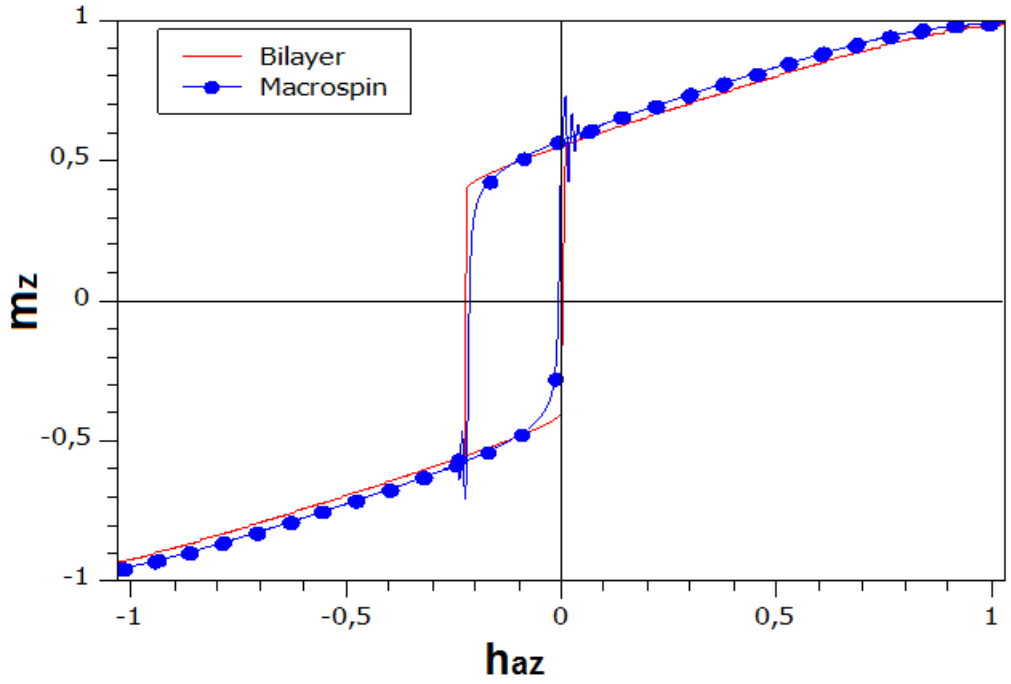

Figure 5.21: Average magnetization vs DC field. The loop in black is the magnetization behavior for bilayer system obtained from the numerical simulations and the loop in blue is the magnetization behavior from the magnetization model.

The saturation magnetization, $M_s = 1.55\ MA/m$, the microwave field $|H_{a\perp}| = 0.08\ MA/m$. Damping constant $\alpha = 0.1$ and the anisotropy constant $K_1 = 2\ MJ/m$ and

$K_2 = 0.048\ MJ/m$. Using these exact system parameters and the exchange constant calculated from the numerical calculations for the bilayer system to show the similar coupling observed in the bilayers we solve the macrospin system numerically.

The exchange energy constant was found to be 0.1, using which we numerically solved the macrospin system. From the results it is found that the magnetization loop obtained for the macrospin model and the bilayer system agree with each other as shown in fig.5.21.

Hence we can conclude that the bilayer system in the limit case of infinite thickness can be considered equivalent to 2 coupled macrospins.

5.2.2 Variation of the microwave field frequency

Until now we only discussed the bilayer system subjected to the in-plain field frequency of 6 GHz, which we used as an example to propose the idea and explain the magnetization dynamic in such systems. Here, we also see the average magnetization behavior of bilayer system as a function of frequency of the rotation of in-plane magnetic field. We first start the magnetization loop subjected to a frequency greater than 6 GHz, where the oscillations are more pronounced.

Here for the sake of clarity in the figures we present only the forward branch of the magnetization loop, i.e. the variation of DC field from negative maximum to positive maximum. In the fig.5.22, the forward branch curve is plotted for the frequencies ranging from 1 GHz to 25 GHz. It can be seen that the switching field is shifting towards more negative values with the increasing frequency, but the reduction is accompanied by the increasing (period) oscillations. There are also more pronounced oscillations when the field reaches the positive maximum value (i.e. saturation). The oscillations can be possibly explained due to the system passing from **P**-type to **Q**-type responses as explained in the single phase systems using phase portraits due to different bifurcations in the system. Taking a closer look at the spatial profiles for these systems, we found that the oscillations are more prominent in the hard phase of the bilayer system.

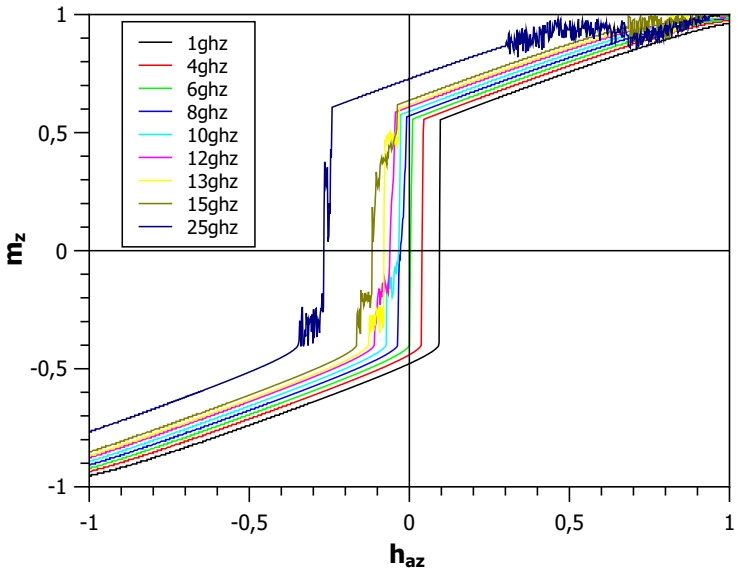

Figure 5.22: Representation of average m_z component of magnetization of bilayer system on variation of h_{az} from negative to positive value as a function of high microwave frequencies.

The oscillation near the saturation persists during the reverse branch of the curve as well. The reverse branch refers to the simulations performed when the DC field h_{az} is varied from positive maximum to negative maximum value. During the reverse branch the system is initially positively saturated and becomes unstable while decreasing the DC field. Similar to the case of the single phase systems, the oscillations during the switching are not present at lower frequencies but start to appear after a certain critical value of the frequency is reached.

We extracted the value of the switching field for different frequencies obtained form the numerical simulation. The variation in the switching field with frequency is plotted in the fig.5.23. We compared the reduction of the switching field in bilayer system with the single phase hard magnetic system. The curve in black represents the bilayer system and curve in red shows switching field for the bilayer system in the absence of the microwave field. It is observed that for the bilayer system, the switching field reduces upto $f = 27$ GHz (not shown in the figure) and then suddenly increases as applied microwave field frequency is increased.

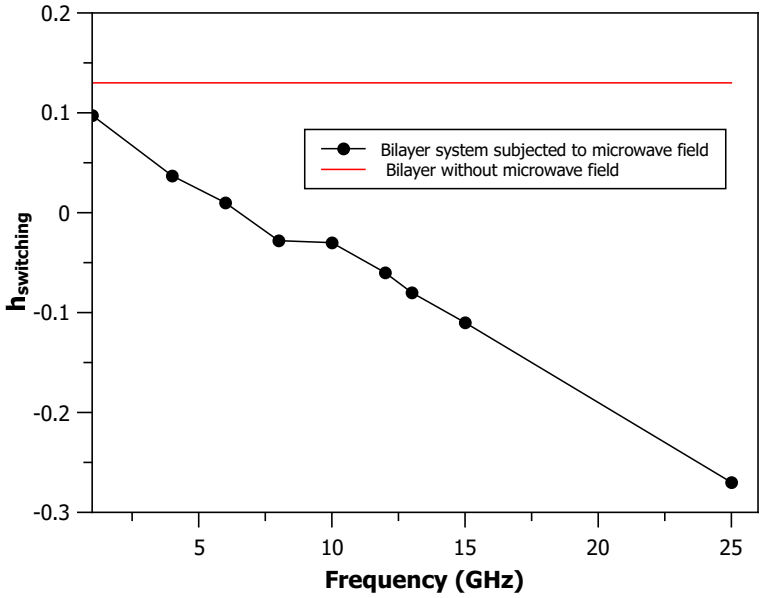

Figure 5.23: Variation of switching field of bilayer system subjected to microwave field as a function of frequency. The red line on the top indicates the bilayer switching field in absence of microwave field.

The switching field for the bilayer system is found to be much lower than the single phase system which is a good result as it proves that the ESM media can be a solution for the challenges in the magnetic recording technology. As we have seen in the case of the single hard magnetic phase in section 5.1.2, the switching is explained using the analytical expressions but for the bilayer spring system the situation is rather different. From our numerical simulation for bilayer we find that the bilayer system presents stationary **P**-mode states under saturating DC fields. From this result we assume that exploring the phase diagram of the bilayer system for different frequencies should give results similar to the ones discussed for the single layer. This assumption is verified for the switching field reduction. The reduction in the bilayer case resembles to the saddle-node bifurcation as in the single phase system. On the contrary to the single phase system, we are able to achieve further reductions of the switching field till frequencies of the order of 10 GHz. The presence of the soft-layer coupled with the hard one seem to drastically improve the frequency at which the threshold field is attained.

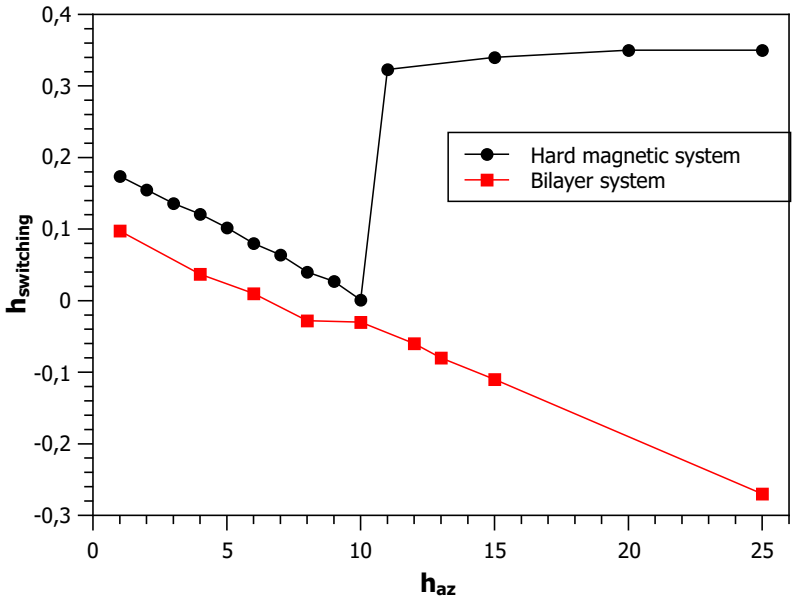

Figure 5.24: Comparison between the switching field of bilayer and hard system and its variation with the microwave frequency.

We also note that the oscillations are only distributed near the region of switching for the frequencies near the 10 GHz range. But for the $f \geq 13$ GHz, the oscillations are more prominent near the switching field and also near the saturation region.

We can conclude from the above that the soft layer aided by the strong coupling at the interface assists the switching behavior and keeps the system stable at higher microwave frequency than the single phase system.

5.3 Summary

In this chapter we studied magnetization reversal in perpendicular single magnetic phase system subjected to microwave magnetic field. This formed a basis for studying the perpendicular bilayer exchange coupled system under similar conditions. Our main motivation to study the systems was to overcome the problem of "recording trilemma" and understand the dynamics of the bilayer system. We used the analytical solution of LLG equation, under the given conditions for single phase media by Bertotti et al. We showed that for bilayer system, LLG equation becomes very complex in nature and we do not have uniform solution. The analytical solutions are very difficult to be worked out. Therefore we used numerical method to solve the LLG equation.

5.4 Conclusion

We studied the result for the perfectly coupled hard and soft magnetic material. Under the assumption of infinite thickness of the system (i.e. thickness $\gg$ domain wall width), coercivity coincides with the propagation field, or better referred to as Switching field (H_{sw}). By observing the numerical results of the bilayer system, it was found that the average magnetization taken along the z-axis behaves like a P-mode. Since the magnetization was non-uniform, therefore the stable solution of the system is given by average magnetization

$< m_z >$, we called this stationary state *global P-mode*. The average magnetization was studied as a function of microwave frequency and it was found that the switching field reduces with increasing frequency. Another feature that was interesting was that the existence of the oscillation beyond the 10 GHz. These oscillations are found to be similar to a quasi-periodic mode or a Q-mode.

The spatial profile of the bilayer system showed very interesting property. The plot between m_z as a function of z at different applied dc field, shows two uniform separated regions by a thin transition region. Similar plot was obtained between $m_\perp$ and z, which shows similar behavior. It was found that the width of the transition region stays constant at different microwave frequencies. Therefore we can conclude that the global P-mode is an average of the two individual P-modes corresponding to the soft magnetic phase and a hard magnetic phase respectively.

Using the analytical solution of the single phase systems, we found that the applied field $\mathbf{h}_a$ could not produce the observed P-modes when this field is applied to the uncoupled systems. Thus using our *ansatz* that the observed P-modes in the bilayer can be generated by the field $\mathbf{h}_i$ which is the sum of the applied field $\mathbf{h}_a$ and the interaction field $\mathbf{h}_{exc,j}$, showing the exchange coupling with the other layer. The exchange field was assumed to be proportional to the magnetization from the other layer. This posed a problem of determining the three components of $\mathbf{h}_i$ and exchange constant C. These 4 unknowns were fully determined using the analytical solution of the single phase media and the constraint $|h_{exc,j}| = C$. Using our numerical results we estimated C=0.1. Also by determining the exchange energy versus the angle between the magnetization of the two layers of the bilayer system, the slope of the curve gives the value of C which was in agreement with our estimate. Thus using the ansatz, we could fully describe the P-modes of the bilayer system.

It was also found that this approach for the bilayer system was equivalent to treating the bilayer system as two exchange coupled macrospins with different uniaxial anisotropies. The numerical solutions of the macrospin were in agreement with the bilayer system.

CHAPTER 6
CONCLUSION AND FUTURE PROSPECTS

Chapter 6

Conclusion and Future Prospects

Contents

6.1	Conclusion	**128**
6.2	Future Prospects	**130**

6.1 Conclusion

This work has been divided into two parts. In the first part, we studied the experimental work related to the synthesis of "*Exchange-Spring*" magnet (ESM) and in the second part, we discuss the dynamics of bilayer "Exchange-spring" system.

- Experimental part:

  The synthesis of ESM was experimentally studied by (i) Mechanical milling and (ii) Ultrasonic mixing. It is very important to have small crystallite size of the precursors in order to obtain desired properties of ESM. We synthesized the nano sized barium hexaferrite by sol-gel method with the crystallite size of $\sim 140\ nm$. The bulk nanocomposites were synthesized from spark plasma sintering (SPS) of the mixtures. The magnets obtained from mechanical mixing showed that the hexaferrite phase disintegrated into magnetite and barium monoferrite phase. This is because of the possible reaction which was initiated during the milling but completes after sintering at $800°C$. Therefore the intermediate phases are not seen in the XRD pattern after mixing but only after sintering. The disintegration is due to access of iron content and it is calculated that minimum 5% is the iron is required to disintegrate barium hexaferrite. This kind of disintegration has also been reported in the literature by several authors. Thus these composites do not retain the hard magnetic behavior but become soft magnetic due to presence of large amount of magnetite phase.

  Since in the previous samples the higher temperature of the synthesis was responsible for disintegration of the hexaferrite phase therefore ultrasonic mixed powders were sintered at lower temperature. The reduction in the hexaferrite phase was found lesser than the previous samples. The hexaferrite disintegrates into maghemite phase. The magnetization of the various samples were compared with the theoretical average of the two precursor phases. If the appropriate volume fraction of the intermediate phases is also considered then the magnetization is found to be lower

than the average theoretical magnetization. In the we found that due to the disintegration of the hexaferrite phase the desired ESM was not obtained. However there is a possibility if the reaction is controlled and if the crystallite size of hexaferrite phase could be reduced even more, the ESM may be obtained.

- Theoretical part:

  It has been shown that ESM is a possible candidate to overcome the "recording trilemma" in order to achieve better recording and storage media. This is the motivation to study the magnetization dynamics in ESM subjecting it to the DC magnetic field and an additional microwave field. Magnetization reversal is studied using microwave assisted magnetic recording (MAMR) as a solution to help the magnetic switching in the ESM which we incorporated in the theoretical analysis. The magnetization dynamics of the bilayer exchange coupled systems are studied theoretically using concepts of micromagnetics. We tried to find the analytical solution of the Landau lifshitz Gilbert (LLG) equation but we found that due to non-uniform magnetization distribution it was difficult to find the stable solution. The following observations are found from the numerical results of the bilayer exchange coupled system:

  - The average magnetization of the bilayer system showed a P-mode like behavior, which we call global **P**-mode.
  - The switching field H_{sw} was found to significantly reduce as a function of increasing frequency of the microwave field.
  - From the spatial profile of the magnetization,it is observed that there are two uniform regions separated by the thin transition region.
  - The width of the transition region remains constant (~ 30) nm. The contribution from the transition region are negligible.
  - It was found that the uncoupled **P**-modes are different from the P-modes of the bilayer system. We developed an *ansatz* that the field generating the P-modes is a combination of an applied field and an additional exchange field which is proportional to the magnetization from the other layer.
  - In order to find out the unknown of this ansatz, specifically the 3 field vectors and the constant of proportionality, or the exchange constant, we used a combination of analytical and numerical data and the constraint $|\mathbf{m}| = 1$. Thus we find 3 unknowns of the vector equation and the constant of proportionality was calculate to be **0.1**. This was further confirmed by calculating the exchange energy of the system from the numerical data, the slope of the exchange energy gives us the constant value.
  - This concept was also compared to the system of two macrospins subjected to similar conditions and under the influence of the exchange field proportional to the magnetization of the other spin. The solution of the macrospin system were found to be in very good agreement with the magnetization loops of the bilayer system.
  - From this we concluded that the we are able to successfully study the dynamics of the bilayer exchange system using semi analytical approach. The system is also found to be equivalent to the two coupled macrospin system.

6.2 Future Prospects

The field of magnetism offer very interesting opportunities. Since the fundamental concepts and origin of magnetism is still a very blooming subject, this works offers many future prospects for further investigation and realization.

The work done in this thesis in the experimental part in the realization of exchange spring magnets was performed under certain limited conditions, which provides more scope for the realization of ESM. Further reduction in the particle size of Barium Hexaferrite: by mechanical milling in vacuum, pre-ultrasonic mixing could help in the better architecture of ferrite based composites. Control of the reduction reaction or the use of Fe less metallic alloys could also help achieve the desired ESM.

On the theoretical aspect, the model used in this thesis is an infinite thick system, which can be modified to study thin systems as used in the many recording and storage devices. During the magnetization reversal phenomena the work was focused on the reversal lead by propagation field system and it remains to study the nucleation phenomenon in the bilayer system. Also our simulations showed us the possibility of zero field switching which offers an interesting and efficient solution for the recording media. Further investigation in this respect needs to be studied both theoretically and experimentally.

APPENDIX

Appendix A

Program Structure

The finite difference program has been implemented in FORTRAN. The main part of the program are described in the following flowchart.

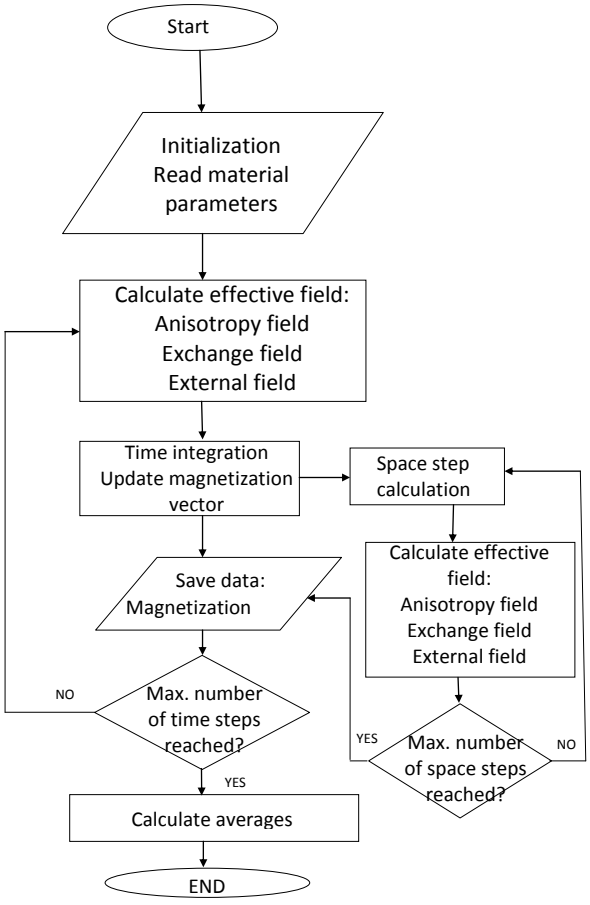

Figure 6.1: Flow chart of finite difference program

For time integration of the LLG equation we use mid-point rule.

Finite difference method

LLG or LL equation are very non-linear in nature, hence we can not always derive the analytical solutions. Therefore we solve the equation using numerical method. For this we have to convert it into a form which can be translated into the algorithm. We use the finite difference method to solve the differential equation, Landau Lifshitz equation describing the magnetization dynamics. First we need to do the time stepping to compute the step by step stationary solutions. We device a code in Fortran based on finite difference method to numerically solve this equation.

Finite-difference methods (FDM) are numerical methods for approximating the solutions to differential equations using finite difference equations to approximate derivatives.
The time interval is assumed to be $0 = t^0 < t^1 < t^2 < ... < t^n = T$. We consider a short time interval (t^i, t^{i+1}), where $t^{i+1} = t^i + \Delta t$. For simplification we assume Δt to be constant.
For the differential equation of the type

$$\frac{dy}{dt} = f(y(t), t) \tag{6.1}$$

$$\frac{dy}{dt}\Big|_{i+1} = y_i + hf(t_i, y_i), \tag{6.2}$$

The latter equation can be written at the time instant $i + \Delta t/2$ (we assume Δt to be constant):

$$\frac{dy}{dt}\Big|_{i+\Delta t/2} = f(y(i + \Delta t/2), i + \Delta t/2) \tag{6.3}$$

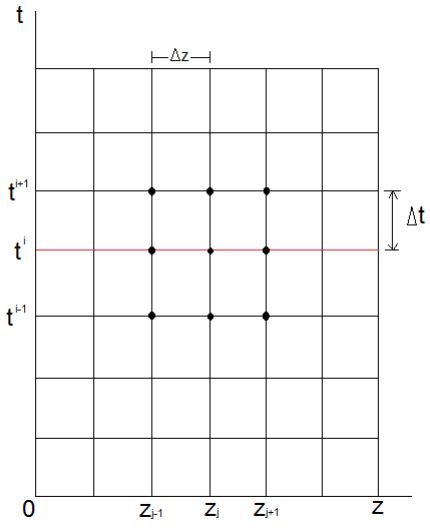

Figure 6.2: Time discretization and spatial point mesh.

The time stepping uses two steps for calculation as seen in the fig.6.2.

$$y(i + \Delta t/2) = \frac{y(i + \Delta t) + y(t)}{2} + Err \tag{6.4}$$

The difference scheme associated with our dynamics is shown step by step as follows. We first write down the LLG equation,

$$\frac{d\mathbf{m}}{dt} = -\mathbf{m} \times \mathcal{H}(\mathbf{m}, t) \tag{6.5}$$

where $\mathcal{H}$ is the given as $\mathcal{H} = (\mathbf{h}_{eff} + \alpha \mathbf{m} \times \mathbf{h}_{eff})$. We consider time instants $i = 1, 2, 3....$ for t_ith time component. We use the following mid-point rule formulae:

$$\left(\frac{d\mathbf{m}}{dt}\right)^{i+1/2} = \frac{\mathbf{m}^{i+1} - \mathbf{m}^{i}}{\Delta t} + err \tag{6.6}$$

$$\mathbf{m}^{i+1/2} = \frac{\mathbf{m}^{i+1} + \mathbf{m}^{i}}{\Delta t} + err \tag{6.7}$$

where Δt is constant.

$$\mathbf{h}_{eff}^{i+1/2} = \frac{3}{2}\mathbf{h}_{eff}^{i} - \frac{1}{2}\mathbf{h}_{eff}^{i-1} \tag{6.8}$$

Using these formulae, we can implement the finite difference method. From this scheme, the complete LLG equation for the $j - th$ cell can be written as,

$$\frac{\mathbf{m}_j^{t+1} - \mathbf{m}_j^{t}}{\Delta t} = -\left(\frac{\mathbf{m}_j^{t+1} + \mathbf{m}_j^{t}}{\Delta t}\right) \times \left[\mathbf{h}_{eff,j}\left(\frac{\mathbf{m}_j^{t+1} + \mathbf{m}_j^{t}}{\Delta t}, t + \frac{\Delta t}{2}\right) - \alpha \frac{\mathbf{m}_j^{t+1} - \mathbf{m}_j^{t}}{\Delta t}\right] \tag{6.9}$$

where j denotes the space point, for simplicity all the space point are equidistant from each other.
The problem of calculating the spatial dependence of magnetization is taken into account as follows , the first partial derivative

$$(\nabla \mathbf{m})^2 = \left(\frac{\partial m_x}{\partial z}\right)^2 + \left(\frac{\partial m_y}{\partial z}\right)^2 + \left(\frac{\partial m_z}{\partial z}\right)^2 \tag{6.10}$$

For calculating the effective field, the exchange term is formulated as $\nabla^2 \mathbf{m}$ which is approximated by the finite difference method

$$\left(\frac{\partial^2 m_x}{\triangle z^2}\right) + \left(\frac{\partial^2 m_y}{\triangle z^2}\right) + \left(\frac{\partial^2 m_z}{\triangle z^2}\right) \tag{6.11}$$

where $\triangle z$ denotes the spacing of the system. Let us now consider the vector $\mathbf{m}_j$ at point j and $\mathbf{m}_{j+1}$ is the neighboring point in z direction. Then we can rewrite the term as

$$\frac{\partial^2 \mathbf{m}}{\partial z^2} = \frac{\mathbf{m}^{i+1} - 2\mathbf{m}^{i} + \mathbf{m}^{i-1}}{(\triangle z)^2} \tag{6.12}$$

Appendix B

One of the ways to represent a dynamical system is by using phase space. A phase space is space whose coordinates are the variables of the system. The equations evolve with respect to time in terms of simple functions which forms the trajectory or orbit of the system to determine its position. The trajectories (shown by arrows)can be represented geometrically in a phase plane which is known as the phase portrait. The steady state of the system (shown by dots) can be stable and unstable which can be represented by node, saddle or focus.
For the dynamical system represented by coupled equations:

$$\frac{dX}{dt} = f(X, Y) \tag{6.13}$$

$$\frac{dY}{dt} = g(X, Y) \tag{6.14}$$

Some phase plots are as shown in figure below.

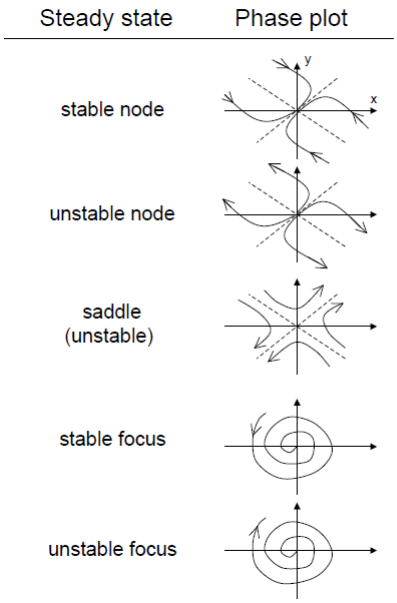

When the system has several steady states, depending on the initial condition the system will evolve towards one of the steady state. The system can also exhibit certain oscillations, which in phase space are represented by closed curve called a limit cycle.

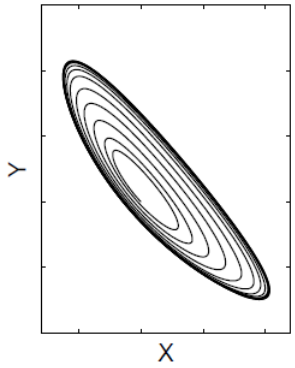

This stability analysis allow us to determine the regions in the phase space where the steady state is stable or unstable. These domains can be represented graphically in bifurcation diagrams. The bifurcation diagrams show a steady state and the behavior of the system changes as a control parameter varies.
There are different type of bifurcations but we shall concentrate on some important cases:

- Saddle-node (fold) bifurcation
- Hopf bifurcation
- Homoclinic bifurcation in which a limit cycle collides with a saddle point.
- Heteroclinic bifurcation in which a limit cycle collides with two or more saddle points.

Saddle-node bifurcation

A saddle-node bifurcation is a collision and disappearance of two equilibria in dynamical systems. In systems generated by autonomous ordinary differential equations (ODEs), this occurs when the critical equilibrium has one zero eigenvalue. This phenomenon is also called fold or limit point bifurcation. Fig.6.3 represents a saddle-node bifurcation for a set of ODEs given by

$$\begin{aligned} \frac{dy}{dt} &= \beta + y^2 \\ \frac{dz}{dt} &= z \end{aligned} \tag{6.15}$$

When the system passes from one state to another, at a certain value of parameter β, two equilibria collide, form a critical saddle-node equilibrium (case $\beta = 0$ in Fig.6.3), and disappear [87].

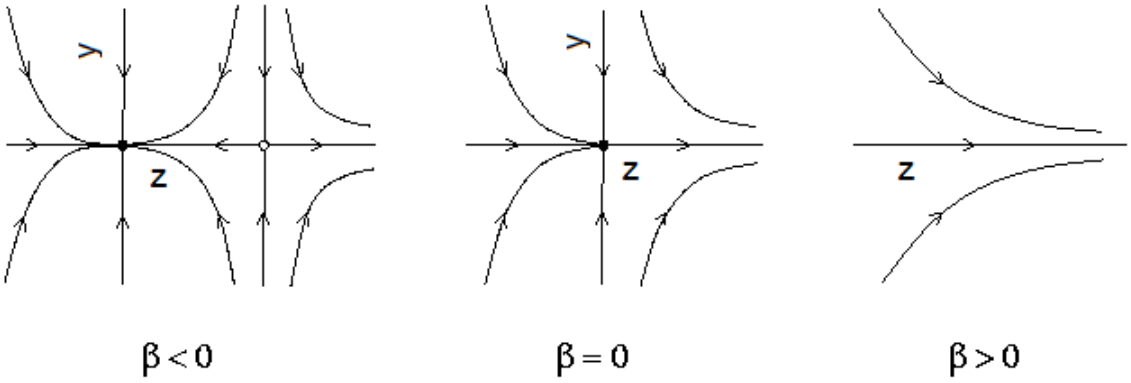

Figure 6.3: Saddle-node bifurcation on the plane in the system $\dot{y} = \beta + y^2$ and $\dot{z} = z$.

Hopf-bifurcation

Andronov-Hopf bifurcation is the birth of a limit cycle from an equilibrium in dynamical systems generated by ODEs (section 6.2), when the equilibrium changes stability via a pair of purely imaginary eigenvalues. The bifurcation can be supercritical or subcritical, resulting in stable or unstable (within an invariant two-dimensional manifold) limit cycle, respectively. When the system changes is stability, a unique limit cycle bifurcates from it [87]. For general systems of the form,

$$\dot{y}_1 = y_2 + \beta y_1 + \sigma(y_1 y_2), \tag{6.16}$$
$$\dot{y}_2 = y_1 + \beta y_2 + \sigma(y_1 y_2) \tag{6.17}$$

The system has equilibrium at the origin for $\sigma = -1$, at $\beta \leq= 0$ and is unstable for $\beta > 0$. Moreover, there is a unique and stable circular limit cycle that exists for $\beta > 0$, this is a supercritical Andronov-Hopf bifurcation, fig.6.4. If $\sigma = +1$, the system is stable for $\beta < 0$ and unstable for $\beta \geq 0$ (weakly at $\beta = 0$), while a unique and unstable limit cycle exists for $\beta < 0$. This is a subcritical Andronov-Hopf bifurcation fig.6.5.

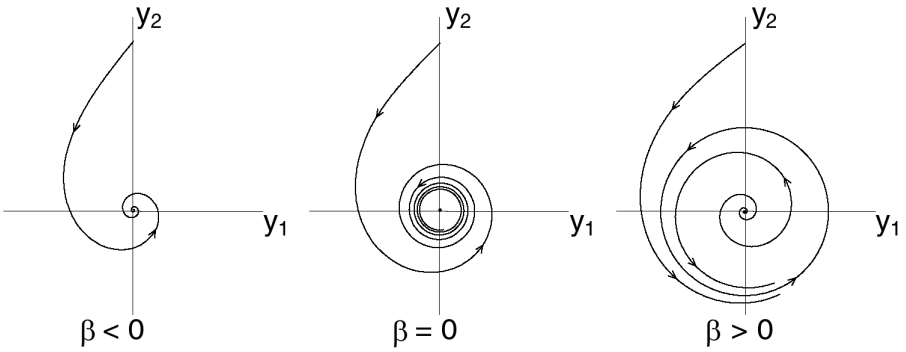

Figure 6.4: Graphical representation of the super-critical hopf-bifurcation.

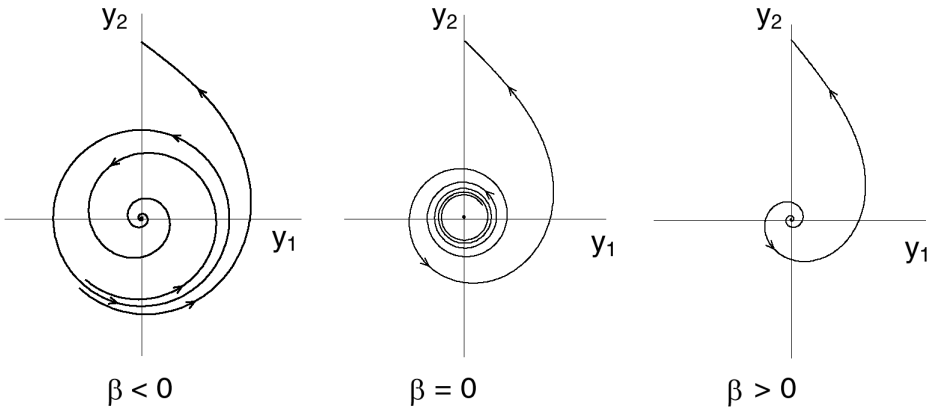

Figure 6.5: Graphical representation of the sub-critical hopf-bifurcation.

Bifurcation diagrams

Using all the stable and unstable points and its dependence on the paramters which in our case are the externally controlled parameters like the in-plane field and the DC field, we plot the phase diagram. The steady states are called P-modes and the stability properties of these states for large and low values of the magnetic fields are studied. The system parameters are h_{az} and $h_{a\perp}$ for which the phase diagram is traced. For large values of h_{az}, only 2 P-modes can be present as det $A > 0$ and when applied field is greater than h_{eff}, it dominates the effective field and at this time no limit cycle is present. So phase portrait is always stable/unstable type.

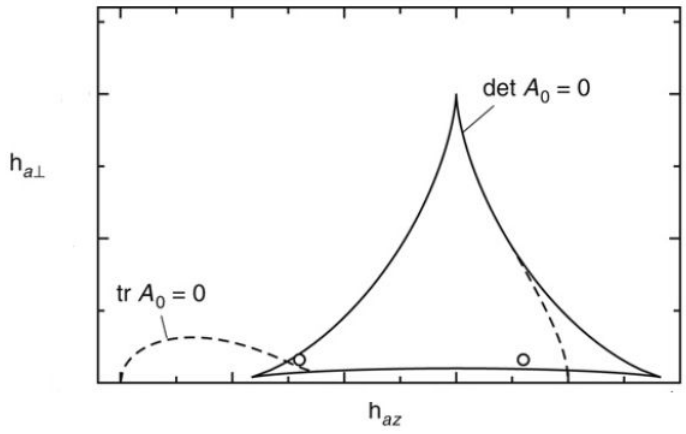

Figure 6.6: Representation of $(h_{az}, h_{a\perp})$ plane.

Fig.6.6 represents $(h_{az}, h_{a\perp})$ control-plane indicating the lines corresponding to det $A = 0$ and trace$A = 0$ when det $A > 0$. Looking at the phase diagram of the system, for the case at constant h_{az}, when the $h_{a\perp}$ is also zero, the situation is static and there exists two fixed points which are both unstable. There is one more solution, $\cos\theta = -h_{eff}/k_{eff}$, this solution represents a limit cycle. Limit cycle is the set of continuous stable equilibrium states characterized by same value of θ. All these states are minimum energy states with respect to θ. When $h_{a\perp}$ is increased, the value of $\cos\theta$ associated with 2 unstable fixed points is reduced: the limit cycle, initially centered about the symmetry axis, become increasingly distorted. When $h_{a\perp}$ becomes large enough, for a critical value the limit

cycle is destroyed by homo-clinic saddle-connection bifurcation. The system jumps form the Q-mode to a stable P-mode. Under decreasing field there is a jump from the P-mode to Q-mode through a saddle-node bifurcation which occurs at lower value of $h_{a\perp}$.

BIBLIOGRAPHY

Bibliography

[1] John Michael David Coey. *Magnetism and magnetic materials*. Cambridge University Press, 2010.

[2] Mary Bellis. Timeline of electromagnetism innovations using magnetic fields.

[3] J.M.D. Coey. Magnetic materials. *Journal of Alloys and Compounds*, 326(12):2 – 6, 2001. Proceedings of the International Conference on Magnetic Materials (ICMM).

[4] Oliver Gutfleisch, Matthew A. Willard, Ekkes Brck, Christina H. Chen, S. G. Sankar, and J. Ping Liu. Magnetic materials and devices for the 21st century: Stronger, lighter, and more energy efficient. *Advanced Materials*, 23(7):821–842, 2011.

[5] Bernard Dennis Cullity and Chad D Graham. *Introduction to magnetic materials*. Wiley. com, 2011.

[6] D.C. Jiles. Recent advances and future directions in magnetic materials. *Acta Materialia*, 51(19):5907–5939, 2003.

[7] Richard Becker and Werner Doring. *Ferromagnetismus*, volume 1. J. Springer, 1939.

[8] Martin Kersten. *Grundlagen einer Theorie der ferromagnetischen Hysterese und der Koerzitivkraft*. JW Edwards, 1943.

[9] J. M D Coey. Hard magnetic materials: A perspective. *Magnetics, IEEE Transactions on*, 47(12):4671–4681, 2011.

[10] Ralph Skomski and J. M. D. Coey. Giant energy product in nanostructured two-phase magnets. *Phys. Rev. B*, 48:15812–15816, Dec 1993.

[11] Nicola Jones. Materials science: The pull of stronger magnets. News Feature, April 2011.

[12] E.F. Kneller and R. Hawig. The exchange-spring magnet: a new material principle for permanent magnets. *Magnetics, IEEE Transactions on*, 27(4):3588–3560, 1991.

[13] Hao Zeng, Jing Li, J. P. Liu, Zhong L. Wang, and Shouheng Sun. Exchange-coupled nanocomposite magnets by nanoparticle self-assembly. *Nature*, 420(6914), 2002.

[14] R. Skomski. Aligned two-phase magnets: Permanent magnetism of the future? (invited). *Journal of Applied Physics*, 76(10):7059–7064, 1994.

[15] Eric E. Fullerton, J. S. Jiang, M. Grimsditch, C. H. Sowers, and S. D. Bader. Exchange-spring behavior in epitaxial hard/soft magnetic bilayers. *Phys. Rev. B*, 58:12193–12200, Nov 1998.

[16] I. A. Al-Omari and D. J. Sellmyer. Magnetic properties of nanostructured cosm/feco films. *Phys. Rev. B*, 52:3441–3447, Aug 1995.

[17] R. J. Astalos and R. E. Camley. Magnetic permeability for exchange-spring magnets:application to fe/sm-co. *Phys. Rev. B*, 58:8646–8653, Oct 1998.

[18] Eric E. Fullerton, J.S Jiang, and S.D Bader. Hard/soft magnetic heterostructures: model exchange-spring magnets. *Journal of Magnetism and Magnetic Materials*, 200:392–404, 1999.

[19] J.M.D. Coey. Permanent magnetism. *Solid State Communications*, 102(23):101 – 105, 1997. Highlights in Condensed Matter Physics and Materials Science.

[20] J. Y. Gu, Jefery Kusnadi, and Chun-Yeol You. Proximity effect in a superconductor/exchange-spring-magnet hybrid system. *Phys. Rev. B*, 81:214435, Jun 2010.

[21] Shi-shen Yan, W. J. Liu, J. L. Weston, G. Zangari, and J. A. Barnard. Magnetization-reversal mechanism of hard/soft exchange-coupled trilayers. *Phys. Rev. B*, 63:174415, Apr 2001.

[22] Shi-shen Yan, J. A. Barnard, Feng-ting Xu, J. L. Weston, and G. Zangari. Critical dimension of the transition from single switching to an exchange spring process in hard/soft exchange-coupled bilayers. *Phys. Rev. B*, 64:184403, Oct 2001.

[23] Z. J. Guo, J. S. Jiang, C. Y. You, V. K. Vlasko-Vlasov, U. Welp, J. P. Liu, and S. D. Bader. Exchange coupling in epitaxial smco(1100)/ndco exchange-spring bilayers. *Journal of Applied Physics*, 93(10):8122–8124, 2003.

[24] Z. J. Guo, J. S. Jiang, J. E. Pearson, S. D. Bader, and J. P. Liu. Exchange-coupled smco/ndco nanomagnets: correlation between soft phase anisotropy and exchange field. *Applied Physics Letters*, 81(11):2029–2031, 2002.

[25] A. J. Zambano, H. Oguchi, I. Takeuchi, Y. Choi, J. S. Jiang, J. P. Liu, S. E. Lofland, D. Josell, and L. A. Bendersky. Dependence of exchange coupling interaction on micromagnetic constants in hard/soft magnetic bilayer systems. *Phys. Rev. B*, 75:144429, Apr 2007.

[26] G.S. Abo, Yang-Ki Hong, Jihoon Park, Jaejin Lee, Woncheol Lee, and Byoung-Chul Choi. Definition of magnetic exchange length. *Magnetics, IEEE Transactions on*, 49(8):4937–4939, 2013.

[27] Ralph Skomski. *Simple models of magnetism*. Oxford University Press Oxford, 2008.

[28] J S Jiang and S D Bader. Rational design of the exchange-spring permanent magnet. *Journal of Physics: Condensed Matter*, 26(6):064214, 2014.

[29] G. Herzer. Grain structure and magnetism of nanocrystalline ferromagnets. *Magnetics, IEEE Transactions on*, 25(5):3327–3329, 1989.

[30] Vamsi M. Chakka, Z. S. Shan, and J. P. Liu. Effect of coupling strength on magnetic properties of exchange spring magnets. *Journal of Applied Physics*, 94(10):6673–6677, 2003.

[31] S. H. Florez, Y. Ikeda, T. Hennen, F. Q. Zhu, K. Takano, and B. D. Terris. Demonstration of the thermal stability advantage of advanced exchange coupled composite media. *Journal of Applied Physics*, 115(17):–, 2014.

[32] F. Garcia-Sanchez, O. Chubykalo-Fesenko, O. Mryasov, R. W. Chantrell, and K. Yu. Guslienko. Exchange spring structures and coercivity reduction in fept/ferh bilayers: A comparison of multiscale and micromagnetic calculations. *Applied Physics Letters*, 87(12):122501, 2005.

[33] S. N. Piramanayagam. Perpendicular recording media for hard disk drives. *Journal of Applied Physics*, 102(1):011301–011301–22, 2007.

[34] W. H. Meiklejohn and C. P. Bean. New magnetic anisotropy. *Phys. Rev.*, 102:1413–1414, Jun 1956.

[35] H J Richter. The transition from longitudinal to perpendicular recording. *Journal of Physics D: Applied Physics*, 40(9):R149, 2007.

[36] M.H. Kryder, E.C. Gage, T.W. McDaniel, W.A. Challener, R.E. Rottmayer, Ganping Ju, Yiao-Tee Hsia, and M.F. Erden. Heat assisted magnetic recording. *Proceedings of the IEEE*, 96(11):1810–1835, 2008.

[37] E. Schreck, D. Li, S.V. Canchi, L. Huang, G.P. Singh, B. Marchon, H.J. Richter, B. Stipe, and M. Staffaroni. Thermal aspects and static/dynamic protrusion behaviors in heat-assisted magnetic recording. *Magnetics, IEEE Transactions on*, 50(3):126–131, March 2014.

[38] Jian-Gang Zhu, Xiaochun Zhu, and Yuhui Tang. Microwave assisted magnetic recording. *Magnetics, IEEE Transactions on*, 44(1):125–131, 2008.

[39] Christophe Thirion, Wolfgang Wernsdorfer, and Dominique Mailly. Switching of magentization by nonlinear resonance studied in single nanoparticles. *Nature materials*, 2(8):524–527, 2003.

[40] D. Suess, T. Schrefl, R. Dittrich, M. Kirschner, F. Dorfbauer, G. Hrkac, and J. Fidler. Exchange spring recording media for areal densities up to 10tbit/in2. *Journal of Magnetism and Magnetic Materials*, 290-291, Part 1(0):551 – 554, 2005. Proceedings of the Joint European Magnetic Symposia (JEMS' 04).

[41] D. Suess, T. Schrefl, S. Fahler, M. Kirschner, G. Hrkac, F. Dorfbauer, and J. Fidler. Exchange spring media for perpendicular recording. *Applied Physics Letters*, 87(1):012504–012504–3, 2005.

[42] Giselher Herzer. Magnetization process in nanocrystalline ferromagnets. *Materials Science and Engineering: A*, 133(0):1 – 5, 1991. Proceedings of the Seventh International Conference on Rapidly Quenched Materials.

[43] J. Moulin, Yannick Champion, L.K. Varga, Jean-Marc Greneche, and F. Mazaleyrat. Magnetic properties of nanocomposites containing fe-ni or fe dispersed in a mn-zn ferrite matrix. *Magnetics, IEEE Transactions on*, 38(5):3015–3017, 2002.

[44] G. W. Elmen. Magnetic alloys of iron nickel, and cobalt. *American Institute of Electrical Engineers, Transactions of the*, 54(12):1292–1299, 1935.

[45] M Sorescu and A Grabias. Structural and magnetic properties of fe50co50 system. *Intermetallics*, 10(4):317 – 321, 2002.

[46] J Smit and HPJ Wijn. Ferrites: physical properties of ferri-magnetic oxides in relation to their technical ap. 1959.

[47] H. Kojima. Chapter 5 fundamental properties of hexagonal ferrites with magnetoplumbite structure. volume 3 of *Handbook of Ferromagnetic Materials*, pages 305 – 391. Elsevier, 1982.

[48] DB Nicholson. Hexagonal ferrites for millimeter-wave applications. *Hewlett-Packard Journal*, 41(5):59–61, 1990.

[49] T. Fujiwara. Barium ferrite media for perpendicular recording. *Magnetics, IEEE Transactions on*, 21(5):1480–1485, 1985.

[50] Yue Liu, Michael G.B. Drew, and Ying Liu. Preparation and magnetic properties of barium ferrites substituted with manganese, cobalt, and tin. *Journal of Magnetism and Magnetic Materials*, 323(7):945 – 953, 2011.

[51] WD Townes, JH Fang, and AJ Perrotta. The crystal structure and refinement of ferrimagnetic barium ferrite, bafe12o19*. *Zeitschrift für Kristallographie*, 125(125):437–449, 1967.

[52] Alexander Pasko, Frédéric Mazaleyrat, Martino Lobue, Vincent Loyau, Vittorio Basso, Michaela Küpferling, CP Sasso, and Lotfi Bessais. Magnetic and structural characterization of nanosized bacoxzn2- xfe16o27 hexaferrite in the vicinity of spin reorientation transition. In *Journal of Physics: Conference Series*, volume 303, page 012045. IOP Publishing, 2011.

[53] F. Mazaleyrat, A. Pasko, A. Bartok, and M. LoBue. Giant coercivity of dense nanostructured spark plasma sintered barium hexaferrite. *Journal of Applied Physics*, 109(7):07A708, 2011.

[54] B. T. Shirk and W.R. Buessem. Temperature dependence of ms and k1 of bafe12o19 and srfe12o19 single crystals. *Journal of Applied Physics*, 40(3):1294–1296, 1969.

[55] G. W. Elmen. Magnetic alloys of iron nickel, and cobalt. *American Institute of Electrical Engineers, Transactions of the*, 54(12):1292–1299, 1935.

[56] R.M. Bozorth. *Ferromagnetism*. An IEEE Press CLassic Reissue. Wiley, 1993.

[57] F Mazaleyrat and L.K Varga. Ferromagnetic nanocomposites. *Journal of Magnetism and Magnetic Materials*, 215216(0):253 – 259, 2000.

[58] Mehdi Ammar. *Study of magnetism of metal-oxide composite and metal-dielctric nanostructures integrated passive components*. PhD thesis, Ecole Normale Superieure de Cachan, 2007.

[59] Johan Moulin. *Elaboration and characttization of metal-ferrite nanostructured ccomposite for applications at high and low frequencies.* PhD thesis, Ecole Normale Superieure de Cachan, 2001.

[60] X.G. Li, A. Chiba, and S. Takahashi. Preparation and magnetic properties of ultrafine particles of feni alloys. *Journal of Magnetism and Magnetic Materials*, 170(3):339 – 345, 1997.

[61] Dajie Zhang, K. J. Klabunde, C. M. Sorensen, and G. C. Hadjipanayis. Magnetization temperature dependence in iron nanoparticles. *Phys. Rev. B*, 58:14167–14170, Dec 1998.

[62] M Saurez, A Fernandez, JL Menendez, R Torrecillas, HU Kessel, J Hennicke, R Kirchner, and T Kessel. Challenges and opportunities for spark plasma sintering: A key technology for a new generation of materials. 2013.

[63] H. M. Rietveld. Line profiles of neutron powder-diffraction peaks for structure refinement. *Acta Crystallographica*, 22(1):151–152, Jan 1967.

[64] H. M. Rietveld. A profile refinement method for nuclear and magnetic structures. *Journal of Applied Crystallography*, 2(2):65–71, Jun 1969.

[65] R.A. Candeia, M.A.F. Souza, M.I.B. Bernardi, S.C. Maestrelli, I.M.G. Santos, A.G. Souza, and E. Longo. Monoferrite bafe2o4 applied as ceramic pigment. *Ceramics International*, 33(4):521 – 525, 2007.

[66] A. Garcia, M. Lusar, S. Sorli, and J. Calbo. Effect of the surfactant and the precipitant on the synthesis of pink coral by a microemulsion method. *Journal of European ceramic society*, 11(23):1829–1839, 2003.

[67] P.G Bercoff and H.R Bertorello. High-energy ball milling of ba-hexaferrite/fe magnetic composite. *Journal of Magnetism and Magnetic Materials*, 187(2):169 – 176, 1998.

[68] Simona Ovtar, Sophie Le Gallet, Ludivine Minier, Nadine Millot, and Darja Lisjak. Control of barium ferrite decomposition during spark plasma sintering: Towards nanostructured samples with anisotropic magnetic properties. *Journal of the European Ceramic Society*, 34(2):337 – 346, 2014.

[69] M Pal, S Bid, S.K Pradhan, B.K Nath, D Das, and D Chakravorty. Synthesis of nanocomposites comprising iron and barium hexaferrites. *Journal of Magnetism and Magnetic Materials*, 269(1):42 – 47, 2004.

[70] C.J. Goss. Saturation magnetisation, coercivity and lattice parameter changes in the system fe3o4-fe2o3, and their relationship to structure. *Physics and Chemistry of Minerals*, 16(2):164–171, 1988.

[71] H El Ghandoor, HM Zidan, Mostafa MH Khalil, and MIM Ismail. Synthesis and some physical properties of magnetite (fe3o4) nanoparticles. *Int. J. Electrochem. Sci*, 7:5734–5745, 2012.

[72] William Fuller Brown. Some magnetostatic and micromagnetic properties of the infinite rectangular bar. *Journal of Applied Physics*, 35(7):2102–2106, 1964.

[73] Helmut Kronmüller and Stuart Parkin. *Handbook of Magnetism and Advanced Magnetic Materials*. Wiley Online Library, 2007.

[74] Thomas Schrefl. Finite elements in numerical micromagnetics: Part i: granular hard magnets. *Journal of Magnetism and Magnetic Materials*, 207(13):45 – 65, 1999.

[75] Thomas Schrefl. Finite elements in numerical micromagnetics: Part ii: patterned magnetic elements. *Journal of Magnetism and Magnetic Materials*, 207(13):66 – 77, 1999.

[76] Giorgio Bertotti. *Hysteresis in magnetism: for physicists, materials scientists, and engineers*. Access Online via Elsevier, 1998.

[77] Massimiliano dAquino. *Nonlinear magnetization dynamics in thin-films and nanoparticles*. PhD thesis, Ph. D. thesis," Universita degli studi di Napoli Federico II"," Universita degli studi di Napoli"Federico II, 2004.

[78] Isaak D Mayergoyz, Giorgio Bertotti, and Claudio Serpico. *Nonlinear magnetization dynamics in nanosystems*. Elsevier, 2009.

[79] G. Bertotti, I.D. Mayergoyz, and C. Serpico. Analytical solutions of landau lifshitz equation for precessional dynamics. *Physica B: Condensed Matter*, 343(14):325 – 330, 2004. Proceedings of the Fourth Intional Conference on Hysteresis and Micromagnetic Modeling.

[80] G. Asti, M. Ghidini, R. Pellicelli, C. Pernechele, M. Solzi, F. Albertini, F. Casoli, S. Fabbrici, and L. Pareti. Magnetic phase diagram and demagnetization processes in perpendicular exchange-spring multilayers. *Phys. Rev. B*, 73:094406, Mar 2006.

[81] G. P. Zhao and X. L. Wang. Nucleation, pinning, and coercivity in magnetic nanosystems: An analytical micromagnetic approach. *Phys. Rev. B*, 74:012409, Jul 2006.

[82] G. Bertotti, C. Serpico, I.D. Mayergoyz, and A. Magni. Nonlinear aspects of landau lifshitz gilbert dynamics under circularly polarized field. *Journal of Magnetism and Magnetic Materials*, 226-230, Part 1(0):495 – 497, 2001. Proceedings of the International Conference on Magnetism (ICM 2000).

[83] Lawrence Perko. *Differential equations and dynamical systems*, volume 7 of *0939-2475*. Springer-Verlag, New York, 1996.

[84] I. D. Mayergoyz, G. Bertotti, and C. Serpico. Rotationally symmetric solutions of the landau–lifshitz and diffusion equations. *Journal of Applied Physics*, 87(9):5511–5513, 2000.

[85] William F. Brown. Virtues and weaknesses of the domain concept. *Rev. Mod. Phys.*, 17:15–19, Jan 1945.

[86] Amikam Aharoni. Theoretical search for domain nucleation. *Rev. Mod. Phys.*, 34:227–238, Apr 1962.

[87] Yuri A. Kuznetsov. *Element of Applied Bifurcation Theory*, volume 112 of *0066-5452*. Springer New York, 2004.